Diese Dissertation haben begutachtet

TU WIEN

Dr. Marie-Alexandra NÉOUZE

Prof. Dr. Herwig PETERLIK

DISSERTATION

Materials from Functionalised Metal Oxide Surfaces: Ionic Nanoparticle Networks and Cellulose Aerogels

ausgeführt zum Zwecke der Erlangung des akademischen Grades eines

Doktors der technischen Wissenschaften unter der Leitung von

Privatdoz. Dr. Marie-Alexandra Néouze

165

Institut für Materialchemie

eingereicht an der Technischen Universität Wien

Technische Chemie

von

DIPL.-ING. MARCO LITSCHAUER

Mat. Nr. 0125499

Leopoldstraße 48, 3400 Klosterneuburg

Wien, am 16. Dezember 2011

II

Ahhh...nice! Dr. H. Liu

Acknowledgements

These two pages are dedicated to the people who not only helped me during the last 3 to 4 years for this work to come into existence, but also for my personal development as a person, scientist, coffee-maker,...

First of all I want to thank Dr. Marie-Alexandra Néouze for giving me the opportunity to work on this project and her supervision of this work. The constant availability, beside the room to develop my own ideas, made it enjoyable to work in this group. In addition I thank Prof. Schubert for his scientific guidance in the beginning of this project.

Further, this work would not have been possible without the scientific expertise and help (making innumerous measurements) of many people: Dr. B. Basnar (AFM, ellipsometry, XPS), Dr. T. Konegger and E. Eitenberger (EDX, SEM), Dr. B. Stöger, C. Maurer and C. Artner (XRD), M. Czakler and Dr. K. Föttinger (Photoluminszenz), Dr. M. Puchberger (NMR), Prof. H. Peterlik and S. Pabisch (SAXS), the people at USTEM, in particular Dr. J. Bernardi and Dr. M. Stöger-Pollach (TEM), Dr. F. Liebner and N. Aigner (cellulose materials), and E. Haimer (sCO_2 drying).

Moreover I thank my present and past colleagues for scientific and non-scientific support, in- and outside university, during and around coffee breaks, barbeque-evenings and birthday-parties; Angelika for her availability for Dominion rounds, Aparna, Bernhard for just being Bernhard, Christian Mar., Christian Mau. my working-class hero, Christine next time more rum please, Christoph L. my favourite version, Christoph R., Claudia, Denisa, Elisabeth, Fatmir, Giedrius, Jakob for his bike related talks, Jasmin the "Würstel-princess", Jingxia, Johannes the destroyer of obstacles, Dr. L. for his memorable impact on the group, Majka, Marina, Martin for bringing the german culture into the office, Matthias for supplying the whole group with chocolate(-)bananas, Michael, Mirka, Mohsin for his conversations about everything and anything, Phillip, Ralf, Robert L. for showing me "Leberkäseland", Robert P., Rupali, Sarah for her calm character, Sorin, Stefan B., Stephan K., Sven, Van An, I will miss your leftovers.

Work at university would be not possible without the help of the people in the "background"; Anita and Melitta for helping me with the administrative hurdles which appeared from time to time, Harald for sharing his IT-knowledge, Stephan R. for providing the chemicals and laboratory stuff and Rupert for repairing everything from bike- to oilpumps.

IV

Kurzfassung

In dieser Arbeit wurde die Synthese neuer anorganisch-organischer Hybridmaterialien, basierend auf Metalloxid Nanopartikel und ionischer Bindeglieder untersucht. Hierfür wurden SiO_2 Nanopartikel, mit Durchmessern von ca. 15 nm, mit Hilfe von Trialkoxysilanen, welche entweder Imidazol oder Chlorid Funktionalitäten besitzen, oberflächenfunktionalisiert. Der entscheidende Schritt, eine nukleophile Substitutionsreaktion, resultiert in einem Netzwerk aus SiO_2 Nanopartikeln basierend auf Imidazolium als verbrückende Einheit. Mittels diverser spektroskopischer Methoden, wie etwa NMR und SAXS, konnte gezeigt werden, dass das erhaltene System eine Nahordnung besitzt, obwohl nicht alle Imidazol Funktionalitäten eine Verbindung eingehen.

Weiters wurde der Einfluss der verschiedenen Komponenten, die Partikel, die Verbindungseinheiten und die Anionen, auf die Eigenschaften des Materials untersucht. Verschiedene Übergangsmetalloxid, in einem anderen Teil der Arbeit auch metallisches Silber, Nanopartikel wurden synthetisiert und funktionalisiert mit Phosphonsäurederivaten. Durch FTIR und TGA Methoden konnte ein Beweis über die Funktionalisierungen erbracht werden. Beispielhaft wurden TiO_2 Nanopartikel Netzwerke synthetisiert, welche hohe spezifische Oberflächen mit interpartikulärer Porösität aufweisen. Netzwerke mit zwei Imidazoliumeinheiten wurden mittels Dichlormolekülen hergestellt. Dabei führen flexible Alkylketten zu schwächer geordneten Systemen, als gegenüber starren. Weiters wurden Austauschreaktionen, mit verschiedensten Anionen durchgeführt. Durch Elementaranalyse konnte gezeigt werden, dass die Chloridanionen nur teilweise ausgetauscht werden konnten. SAXS Untersuchungen wiesen auf eine Anordnung der Imidazoliumeinheiten hin.

In einem weiteren Teil der Arbeit wurde die Herstellung von Mono- und Multischichten von TiO_2 Nanopartikel auf Siliziumwafern gezeigt. Dabei zeigen die erhaltenen Schichten Widerstände gegenüber Scherkräften, im Bereich von kovalenten Bindungen.

Weiters wurde der Sol-Gel Process, welcher verwendet wurde um die SiO_2 Nanopartikel zu funtionalisieren, zur Oberflächenmodifizierung von Zelluloseaerogelen, mittels verschiedenen Verhältnissen von CPTMS und TEOS, benutzt. Mit Hilfe von N_2-sorptionsmessungen bei 77 K wurde gezeigt, dass durch bestimmte Kombinationen das poröse System der Aerogele erhalten werden konnte.

Abstract

In this work the synthesis of new inorganic-organic hybrid materials based on metal oxide nanoparticles and ionic connectors was investigated. Therefore, SiO_2 nanoparticles, with sizes around 15 nm diameter, were surface functionalised using trialkoxysilanes bearing either imidazole or chloride end groups. The final step, a nucelophilic substitution reaction between these two functionalities, results in a SiO_2 nanoparticle network based on imidazolium as briding units. Through various spectroscopic methods, such as NMR and SAXS, it could be shown, that the system exhibits a short-range ordering, even though not every imidazole undergoes a reaction.

Further, the influences of the different components, the nanoparticles, the ionic bridging unit and the anionic counterpart, on the properties of the system were investigated. First, different transition metal oxide, and in another part also metallic silver, nanoparticles were synthesised, and functionalised with phosphonic acid, bearing chloro or imidazole end groups. FTIR and TGA measurements provided proof of the modifications. Exemplary, TiO_2 nanoparticle systems were synthesised, showing high surface areas, together with interparticle porosity. For the second alteration, different dichloro compounds were used to bridge SiO_2 nanoparticles. Thereby, flexible alkyl chains resulted in weaker ordered networks, than by using more rigid ones. Furthermore anion metathesis reactions with different anions were carried out on the networks. Through elemental analyses it could be seen, that the chloride anions where only partially exchanged. SAXS investigations showed the evaluation of arrangement of the imidazolium units.

In another part of the work the fabrication of these covalently connected nanoparticle networks was highlighted. Mono- and multilayers of TiO_2 nanoparticles were deposited on silicon substrates. Thereby, the connections showed resistances against shearing forces, typical for covalent bonds.

In the last part the sol-gel process, used for the functionalisation of SiO_2 nanoparticles, was also used in order to surface functionalised cellulose aerogels, using different ratios of CPTMS or TEOS. It was shown through nitrogen sorption measurements at 77 K, that different combinations of these led to the preservation of the porous systems.

Parts of this work have been published

"Nanoparticles connected through an ionic liquid-like network"; M. Litschauer, M.-A. Néouze: Journal of Materials Chemistry, **2008**, *18*; 640 - 646.

"Nanoparticles / ionic linker of different length: short-range order evidenced by Small Angle X-Ray Scattering"; M. Litschauer, H. Peterlik, M.-A. Néouze: Journal of Physical Chemistry C, **2009**, *113*, 16; 6547 - 6552.

"Porous Titania Ionic Nanoparticle Networks"; M.-A. Néouze, M. Litschauer, M. Puchberger, H. Peterlik: Langmuir, **2011**, *27*, 7; 4110 - 4116.

"Anion Metathesis in Ionic Silica Nanoparticle Networks"; M. Litschauer, M. Puchberger, H. Peterlik, M.-A. Néouze: Journal of Materials Chemistry, **2010**, *20*; 1269 - 1276.

"Photoluminescence as complementary evidence for short-range order in Ionic Silica Nanoparticle Networks"; M. Czakler, M. Litschauer, K. Föttinger, H. Peterlik, M.-A. Néouze: Journal of Physical Chemistry C, **2010**, *149*, 49; 21343 - 21347.

"Layer-by-layer assembly of titania nanoparticles based ionic networks"; B. Basnar, M. Litschauer, S. Abermann, E. Bertagnolli, G. Strasser, M.-A. Néouze: Chemical Communications, **2011**, *47*; 361 - 363.

"Silica modified cellulosic aerogels"; M. Litschauer, M.-A. Néouze, E. Haimer, U. Henniges, A Potthast, T. Rosenau, F. Liebner: Cellulose, **2011**, *18*, 1; 143 - 149.

Abbreviations

Instrumentations

AFM	Atomic force microscopy
ATR	Attenuated total reflectance
BET	Brunauer, Emmett and Teller
BJH	Barrett, Joyner and Halenda
CP	Cross-polarisation
DLS	Dynamic light Scattering
EDX	Energy dispersive X-ray spectroscopy
FT-IR	Fourier transform infrared spectroscopy
GPC	Gel permeation chromatography
HBMC	Heteronuclear multiple-bond correlation spectroscopy
HR	High resolution
LFM	Lateral force microscopy
MAS	Magic angle spinning
NMR	Nuclear magnetic resonance
SAXS	Small-angle X-ray scattering
sc	Supercritical
SEM	Scanning electron microscopy
TEM	Transmission electron microscopy
TGA	Thermogravimetric analysis
t-plot	Thickness-plot
UVA	Ultraviolet absorber
UV-Vis	Ultraviolet-visible
XPS	X-ray photoelectron spectroscopy
XRD	X-ray diffraction

Chemicals

BF_4	Tetrafluoroborate
BMIm	1-Butyl-3-methylimidazolium
$CDCl_3$	Deuterated chloroform
CL	Cotton linter
CPTMS	3-Chloropropyltrimethoxysilane
DMF	Dimethylformamide
DMSO	Dimethylsulfoxide
Et	Ethyl
Im	Imidazole
Me	Methyl
NMMO	N-methylmorpholine-N-oxide
PF_6	Hexafluorophosphate
Pr	Propyl
PTFE	Polytetrafluoroethylene
Sol	Hardwood pre-hydrolysis kraft pulp
$T_{f2}N$	Bis(trifluoromethylsulfonyl)imide
THF	Tetrahydrofuran
TEOS	Tetraethoxysilane
TMOS	Tetramethoxysilane
TMSBr	Trimethylsilyl bromide

Spectroscopy

°	Degree
2θ	Diffraction angle
λ	Wavelength
A	Absorption
a.u.	Arbitrary units
d	Doublet
kD	Kilodalton
m	Multiplet
MW	Molecular weight
P/P_0	Relative Pressure
ppm	Parts per million

X

q	Scattering vector
rpm	Round per minute
s	Singlet
t	Triplet
w%	Weightpercent

Contents

Chapter 1

Introduction

1.1 Hybrid Materials

The constant demand of materials with improved mechanical or chemical properties, has led scientific research to the development of hybrid materials. Thereby, the term hybrid material, refers to a system of at least two components, mostly one inorganic and one organic, on a molecular scale. As in many other field of chemistry, nature has been a step ahead in the production of hybrid materials. For instance bones, mollusc shells or diatoms, where organic eukaryotic microorganisms are covered by a silica shell, present nice examples for inorganic-organic hybrid materials.[1] The aim of the synthesis of nature, as well as man-made derived hybrid materials stays the same; the combination of the properties of the two parts, within one material, e.g. the hardness of nanoparticles, with the elasticity of a polymer.

To draw a classification, two classes of hybrid materials can be distinguished, depending on the kind of interaction between the inorganic and the organic part. In *class I* materials, only weak bonds are present, e.g. hydrogen, van der Waals or ionic, whereas in *class II* hybrid materials the two phases are connected together through strong chemical bonds, for example covalently.[2] In this work hybrid materials presenting the second class, based on nanoparticles and ionic connectors, were investigated

1.2 Metal and Metal Oxide Nanoparticles

In the last decades nanoparticles evolved into one of the most diverse compounds in materials chemistry. This is, on the one hand, due to their great variety, both chemically and structurally, and, on the other, to their unique characteristics, most of the time different from the corresponding bulk material. Nanoparticles are usually in a

size range of between 1 and 100 nm,[3] a dimension, where quantum chemistry cannot be applied and solid state physics are not valid anymore.[4] This derives from an increased surface-to-volume ratio and a gradually conversion of the common electron bands for the bulk material to molecular orbitals, with decreasing size, the so-called "quantum size effect" (Figure 1.1)
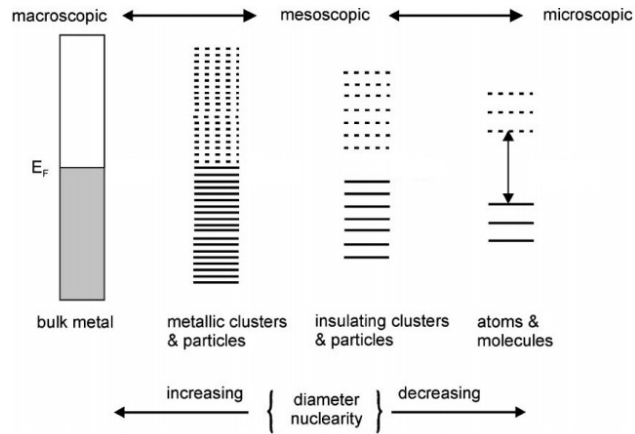
Figure 1.1: Evolution of the band gap with decreasing size of the investigated objects.[5]

Thereby, a wide range of properties is influenced, optical, electronic or magnetic. This makes nanoparticles interesting for many applications, e.g. industry, electronics or even every day life product, such as coatings[6] or paints.[7][8] Another reason for the increasing interest in nanoparticles is their wide range of life science applications, e.g. drug delivering agents or contrast markers.[9,10] This stems from the fact, that, besides noble metals as gold,[11] also some of the common metal oxides, e.g. TiO_2, SiO_2, WO_3 or Fe_3O_4 are not eliminated by macrocyts and therefore, posses low cytotoxicity values.[12]

For the preparation of nanoparticles, two different kinds of pathways can be followed: a *top down* and a *bottom up* approach.[3] In the first process, *top down*, the particles are generated from macroscopic objects. Thereby, physical methods are applied, such as electron beam photolitography,[13,14] or grinding and high energy ball milling.[15,16] As for the first technique, the electron beam photolitography, mainly used by the microelectronics industry, diameters around 10 nm can be generated. Limitations are reached upon down-scaling, since costs for equipments and operating facilities increase. In the second technique, grinding or high energy ball milling, mechanical forces are applied on metal or metal oxide powders, e.g. Ti or ZnO.[15,16] With this technique nanoparticles with sizes of about 2 nm are reached. A drawback

is the usually broad size distribution, accompanied with defect rich surfaces.

On the contrary, through the *bottom up* approach nanostructures are formed from molecular building blocks.[1] Thereby, this pathway makes use of all kind of covalent, and non-covalent interactions, e.g. hydrogen, van der Waals or electrostatic interactions. The assembly is driven by the tendency to form energetically favourable states. Through this approach, not only nanoparticles but larger nanostructured arrays can be formed, for example bilayers in biological membranes.[4] Since only *bottom up* approaches were used throughout this work, pathways using this route will be discussed in detail in the following chapters.

1.2.1   Synthesis of Metal Oxide Nanoparticles

Various *bottom up* approaches have been developed for the synthesis of metal oxide nanoparticles. The chosen method depends on the investigated systems and desired compounds. For crystalline nanoparticles the hydrothermal synthesis is often used. It is achieved through the thermal decomposition of the precursors under elevated temperatures and pressures, in the presence of water. The controlled nucleation and growth of the particles is driven by the dissolution of the precursor and precipitation of the stable compound. Through this approach, crystalline ZrO_2 nanoparticles with sizes around $10\,nm$ can be prepared.[17]

Another technique, which yields nanoparticles with narrow size distributions is the precipitation method. The precipitation of the nanoparticles, often carried out in water, is induced by the addition of a salt, acid or base. Thereby, all nuclei must form at the same time, before subsequent growth. For example, mixed oxide system, such as Fe_3O_4, can be formed from a solution containing Fe^{2+} and Fe^{3+} ions.[18]

Nevertheless, one of the most used methods to prepare nanosized objects, is the sol-gel process, which will be described in detail.

Sol-Gel Process

The sol-gel process can be described as a process, where a precursor solution is turned into an inorganic solid via inorganic polymerization reactions induced by water.[19] Through the use of the sol-gel process the production of ceramic and ceramic-organic nanostructures is enabled at low reaction temperatures and through the usage of non-toxic solvents.[4,20] Thereby, the process can be divided into four individual steps: the synthesis of the sol, the gelation process, ageing and finally drying, with additional shaping, of the final product.

The first step consists of the synthesis of a *sol*, a colloidal suspension where the colloids, either amorphous or, in special cases, crystalline, can be in the range of about 1 to 1000 nm. During the preparation of these *sols* two types of reactions are mainly present, hydrolysis and condensation reactions (Figure 1.2).

The rate at which these two kind of reactions are proceeding, depend on several factors: choice of solvent, catalyst, pH, amount of water, temperature, and, maybe the most important one, the choice of the precursor.

It is important to note, that the use of a catalyst is of importance in the particular case of silicon. Silicon exhibits rather low reactivity towards condensation and hydrolysis reactions due to the fact of a low electrophilicity and fully saturated coordination sites. On the contrary, transition metals (Ti, Zr, Mn, Cr, Al,...) possess a more electropositive character and a large number of coordination sites, making them highly reactive towards hydrolysis and condensation reactions.

For the synthesis of silicon dioxide, tetraalkoxysilanes, $Si(OR)_4$, can be used with R being short alkyl chains. The reaction rate for the hydrolysis decreases in the order $OMe > OEt > O^nPr > O^iPr$.[4] Tetraethlorthosilicate (TEOS) and tetramethylorthosilicate (TMOS) are the most investigated ones. Furthermore, it is also possible to introduce organic functionalities by starting from tri- or dialkoxysilanes,[20,21] as described in detail in the following chapter.

As said before, the range of pH in which the synthesis is performed, is of great importance. It influences which kind of reaction, hydrolysis or condensation, is dominant. At lower pH values, below the point of zero charge, which is between 1.5 and 4.5 for silica systems, depending on the degree of condensation, the electron density on the central silicon atom decreases. Therefore, less branched networks are obtained since the attack on terminal silicon atoms is favoured. Above the point of zero charge, the opposite is achieved. The electron density is increased on the attacked central silicon atom, therefore leading to more branched systems.

Either way, the second step of the sol-gel process, *gels* are obtained.

As mentioned before, transition metals differ from silicon, regarding the hydrolysis and condensation reactions in respect to their different chemical nature.[21,22] Due to their high reactivity, larger alkoxy moieties are used, e.g. O^iPr, to prevent the formation of bulk materials.

Hydrolysis

$$\equiv\!\!Si\!\!-\!\!OR \quad + \quad H_2O \quad \longrightarrow \quad \equiv\!\!Si\!\!-\!\!OH \quad + \quad R\!\!-\!\!OH$$

Condensation

$$\equiv\!\!Si\!\!-\!\!OH \quad + \quad HO\!\!-\!\!Si\!\!\equiv \quad \longrightarrow \quad \equiv\!\!Si\!\!-\!\!O\!\!-\!\!Si\!\!\equiv \quad + \quad H_2O$$

$$\equiv\!\!Si\!\!-\!\!OR \quad + \quad HO\!\!-\!\!Si\!\!\equiv \quad \longrightarrow \quad \equiv\!\!Si\!\!-\!\!O\!\!-\!\!Si\!\!\equiv \quad + \quad R\!\!-\!\!OH$$
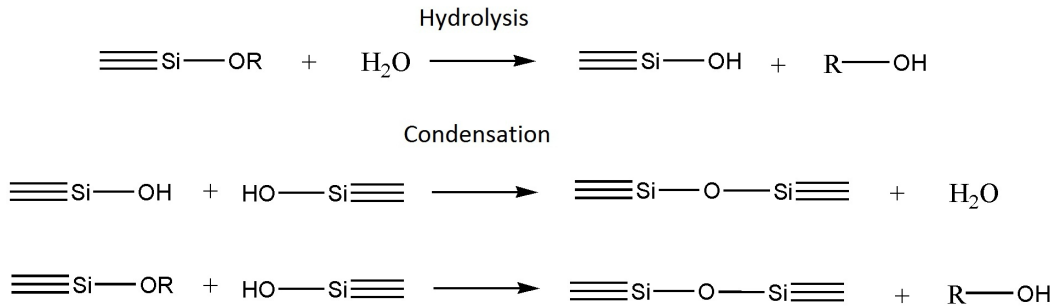
Figure 1.2: Schematic depiction of the different stages of a sol-gel reaction. [4]

The hydrolysis product is dependent not only on the pH of the solution, but on the charge, coordination number and electronegativity of the used metal center. [22] The subsequent condensation process can be divided into two steps: olation and oxolation (Figure 1.3). In the *olation* process a labile hydroxy bridge is formed, accompanied by β-elimination of water. Several different types can be present, depending on the size and charge of the used metal ion. In the second condensation reaction, the *oxolation*, an oxygen bridges two metal centres, occurs by fast nucleophilic substitution addition.
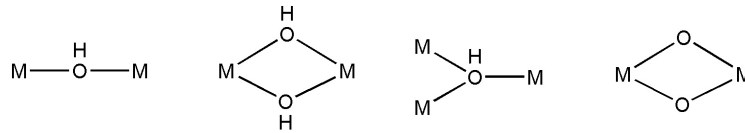
Figure 1.3: Different types of olation and oxolation products.

The third and fourth step, ageing and drying, are equal for both kind of metal oxide materials, deriving from silicon and transition metals. During the ageing step, polycondensation reactions continue, beyond the point of gelation. This point describes the moment, a continuous network is formed, which can be macroscopically seen by an increase of the viscosity of the mixture till no flowing of the liquids is possible anymore. Furthermore, the structure of the network is strengthened through condensation reactions of neighbouring M-OH or M-OR groups. [4] At this stage also ripening can occur, leading to a disappearance of small particles and filling up of small pores.

The last step, drying, is a critical step, since it determines the shape of the final material. By evaporation of the residual solvent in the pores of the gel through elevation of temperature, the tension in the pores increases to a point, where the porewalls collapse and structural features are lost. This process results in *Xerogels*.

Through supercritical drying, most often CO_2 is used, macroporous structures can be preserved, *Aerogels* are obtained.

Furthermore, there has been increasing investigations on non-aqueous sol-gel techniques, for the production of mixed metal oxide nanoparticles.[23,24] Thereby, the oxygen for the nanoparticle formation is provided by the solvent, being ethers, alcohols, ketones or aldehydes. Subsequently condensation reactions occur under cleavage of alkyl halides, ethers, esters or amides.[19,25]

1.2.2   Synthesis of Metal Nanoparticles

As for metal oxide systems, several synthetic *bottom-up* approaches exist for the formation of metal nanoparticles. Many groups focussed on the formation of noble metal oxide particles, in particular gold and silver. Generally, the existing *bottom up* pathways deal with the reduction of noble metal salts, such as $HAuCl_4$,[26] $AgNO_3$,[27,28] or H_2PtCl_6.[29]

The first synthesis of gold nanoparticles reported in scientific literature, dates back to 1857, when british scientist Michael Faraday prepared gold nanoparticle suspensions with various diameters, through the reduction of auric acid using phosphorous in carbon disulfide. This resulted in differently coloured systems.[30] What Faraday did not know, is that the size of metal nanoparticles is crucially dependant on the amount and chemical structure of the used stabilisers. Nanoparticles, in particular metal nanoparticles, tend to agglomerate through van der Waals forces, because of their high surface energies. Therefore, stabilisers are used to induce repulsive forces, e.g. solvation, electrostatic or steric. These agents can have various structures, e.g. thiols, carboxylic acids or amines.[31,32]

A facile approach for the production of gold nanoparticles was developed by Turkevich *et al.*,[33,34] later refined by Frens.[35] In this method sodium citrate is applied as both reduction and stabilising agent. Gold nanoparticles ranging from 16 to 140 nm are obtained, depending on the sodium citrate concentration. Beside the stabilisation with rather small molecules, the introduction of a hydrophobic shell could be achieved by Brust *et al.*.[36] In their report, the production of 1 to 2 nm sized gold nanoparticles functionalised with long chain alkylthiol, was described. Thereby, a phase catalyst was used, tetraoctylammonium bromide (TOAB), to transfer the gold ions into an organic solvent, in which the thiol capping agent is dissolved. Reduction to metallic gold is then triggered through addition of a strong base, sodium borohydride.

Very recently Martin *et al.* investigated a method, where the noble metal

nanoparticles are stabilised electrostatically, through addition of simple base or acidic molecules, e.g. hydrochloric acid.[37]

1.2.3   Surface Modification of Metal and Metal Oxide Nanoparticles

As shown in the previous chapter, nanosized materials possess unique physical and chemical properties, compared to the bulk material. As a consequence, modification of the surface of such materials is necessary to suit the needs for specific application, e.g. to prevent agglomeration of the particles,[38–40] or tailor the surface properties in order to obtain improved mechanical properties, when used as filler for polymeric materials.[41–43] Another field for the usage of modification agents, is the possibility to enable and tune the self-assembly characteristic,[44,45] which will be described later in detail. For these listed purposes, functionalising agents bearing simple organic groups may be sufficient, but through the introduction of functional groups, interactions with molecules, other nanoparticles, surfaces, or solids is enabled.

Two criteria have to be considered for the choice of the appropriate functionalising agent: first, it is important to know the chemical nature, and therefore the reactivity of the reactive groups on the surface of the solid interface and second, to adjust the functional end group to fit the targeted field of application. One can choose from a plethora of different anchoring units, depending on the strength of interaction to the surface of the inorganic compound. These range from organosilanes, for maingroup metal oxides, e.g. SiO_2,[46–48] SnO_2,[49] or Al_2O_3,[50] phosphorous based coupling agents, used for transition metals, e.g. TiO_2,[51–53] Fe_3O_4,[54–56] Y_2O_3,[57] Ta_2O_5,[58] or mixed oxides, such as $BaTiO_3$,[59] carboxylic acids, used to modify AgO and Al_2O_3,[60] sulfonic acids for amorphous Fe_2O_3,[61] amines, used to modify Pd nanoparticles,[62] and thiols, mainly used as modifying agent for noble metals, such as Au,[36,63] Ag,[64] or Pd nanoparticles.[65]

To achieve such a modification of the surface of the nanoparticles, two synthesis routes are possible: post synthetic and *in situ* functionalisation.[4] In the first approach, particles are formed, e.g. via sol-gel or precipitation methods, and modified in a second step. Thereby, the reactive O^- or OH groups, in the case of metal oxide systems, on the surface undergo hydrolysis reactions with the appropriate functionalising agents. For the *in situ* functionalisation, molecular building blocks, in many cases organosilanes, can be synthesised, bearing for example β-diketones, prior to hydrolysis and condensation reactions. These β-diketones can selectively bind to many metal centers, e.g. titanium, yielding mixed metal oxide systems.[66]

Silane Coupling Agents

As discussed above, silanes are used in a broad variety for post and *in situ* functionalisation processes for the past decades, for metal oxide nanoparticle systems.[67] Thereby, organochlorosilanes and organoalkoxysilanes are most commonly used (Figure 1.4).[68]
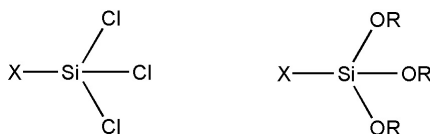

Figure 1.4: Chemical structure of organochloro- and organoalkoxysilanes.

Organochlorosilanes are obtained through the Müller-Rochow process, a process to prepare such compounds on an industrial scale, developed in the 1940s.[69] The hydrolysis—alkoxysilanes are synthesised this way—proceeds through the generation of hydrochloric acid as a by-product (Figure 1.5).
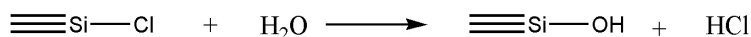
Figure 1.5: Hydrolysis reaction of organochlorosilanes.

Alkoxysilanes on the other hand, with the molecular formula X_n-$Si(OR)_{4-n}$, are most commonly used as mono- or trialkoxysilanes. Here, the alkoxides are, as for the synthesis of silica nanoparticles, usually ethoxy and methoxy groups.[4] Further, inductive effects of the substituents are of importance.[70] These can cause incomplete hydrolysis, and therefore mono-, bi- and tridendate binding states (Figure 1.6).[71] Through the usage of trifunctional silanes—assuming a sterical demand of about $25\,\text{Å}^2$, when bond to the nanoparticle surface—more dense layers on silicon surfaces are formed. Helmy *et al.*[72] showed, that the surface coverage decreases from about 4.5 ligand per nm^2 to about 1.5 ligands when monoalkoxysilanes are used instead of the trifunctional ones. The reason for this effect can be explained by the increase of the sterical demand of the non-hydroliseable groups on the silicon atom. As drawback, when trialkoxysilanes are used, the possible formation of multilayers and networks, next to the most commonly stabilisation through lateral cross condensation,[73] has to be considered (Figure 1.6). Tian *et al.* could prove the formation of multilayers through sophisticated IR techniques.[74] During the later cross-condensation two mechanisms are present, depending on the reaction conditions.[75] First, the *liquid condensed mechanism* assumes, that oligomeric silane chains are formed in solution,

prior to adsorption on the surface. The *liquid expanded mechanism*, on the other hand, is goverened by an island-like growth on the substrate, forming dense layers. It has to be considered, that the hydrolysis and condensation reaction of the organosilanes are reversible. It could be shown, that the Si-O-Si bond can be cleaved by alcohols and hydroxide groups.[76]

Despite the formation of multilayers and reversibility of the reaction, organochloro- and organoalkoxysilanes present a versatile group for the modification of silica surfaces. Many different silanes are commercially available or can easily be synthesised as shown later in this work.
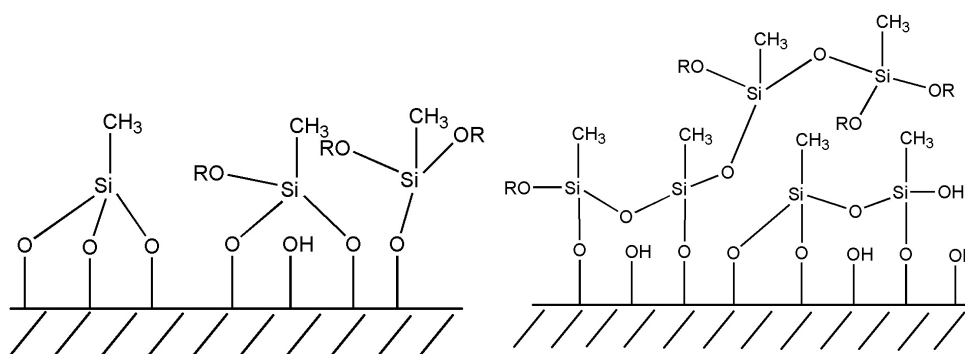
Figure 1.6: Mono-,di- and tridentate (left),[71] and mono- and multilayered (right) bonding of silanes to a surface containing hydroxy groups.[73,74]

Phosphorous Based Coupling Agents

Another functional group, suitable for the surface modification of metal oxide systems, are phosphonic acids. Beside the fact, that some Si-O-M bonds, especially in the case for titanium as metal, are unstable towards hydrolysis,[77] three advantages make phosphorous based coupling agents favourable compared to silanes for the modification of transition metal nanoparticles.[53,78] First, no homocondensation occurs under normal reaction sol-gel condition, resulting in more defined layers. Second, the modification can easily be performed in aqueous media since condensation of P-OH and P-O$^-$ moieties do not take place. The third and last advantage, as a consequence, is given by the fact, that phosphorous based coupling agents react solely with hydroxy groups of the surface and yield strong covalent bonds to the surface of transition metals.[79,80]

As for the organosilanes, phosphorous based coupling agents can bear one to three coordination sites. The most common compounds are thereby the phosphoric and phosphonic ester compounds (Figure 1.7).

Figure 1.7: Chemical Structure of phosphoric and phosphonic acid esters.

For di- and trifunctional phosphorous based coupling agents the hydroxy groups are gradually replaced through non reactive moeties.[53,81] The formation of the covalent bond between the respective coupling agent and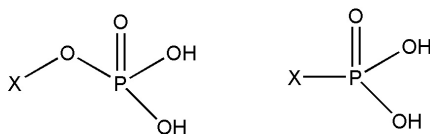 the substrate remains the same for all phosphorous species. Thereby, the M-O-P bonds are built up through the condensation of the hydroxy groups on the surface, M-OH, with the hydroxy groups attached to the phosphour, P-OH, under cleavage of water. Further, as for the attachment of phosphine oxide derivaties, OPR_3, bearing only a double bonded oxygen, this oxygen groups can interact with *Lewis* acidic metal centers.[78]
As shown by Daou *et al.*,[55] the pH value plays an important role during the condensation reaction. Since the condensation reaction is favoured by electrostatic interactions the pH has to be adjusted regarding the pKa value of the respective coupling agent, determining the degree of deprotonation. The described condensation reaction usually proceed very fast. Reaction times of only some seconds can lead to significant changes of the surface coverage of transition metals[41,82] After the formation of complete monolayers, several minutes are required, surface coverages of about 4.5 ligands per nm^2, compareable to organosilanes, are achieved.[72]

Keeping all these different aspects in mind, several binding states are possible (Figure 1.8).[83,84] The found binding states range from mono- to bi- and tridendate modes, either involving the double bonded oxygen atom or not. Several characterisation methods have been undertaken to resolve all possibilities, for example ^{17}O and ^{31}P solid state NMR measurements.[53,80]
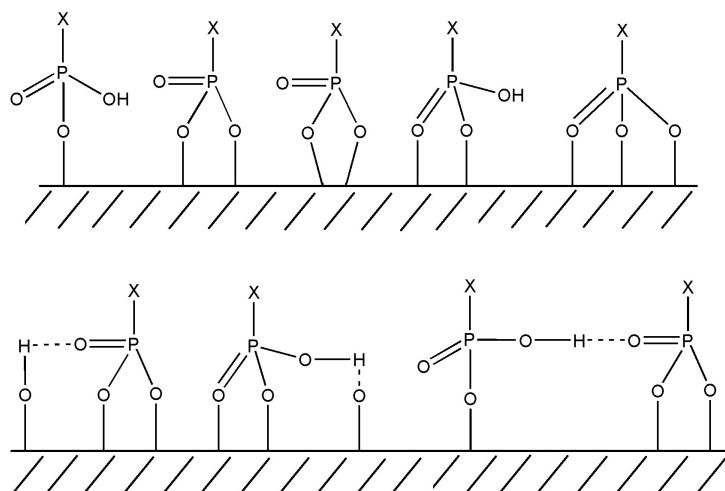
Figure 1.8: Different binding states of phosphorous based coupling agents on a transition metal surface.

Beside these bridging modes, also chelating (Figure 1.8, middle upper schematic description) states are also possible to emerge. Furthermore, the mentioned investigations suggest the formation of hydrogen bonds, either between two neighbouring phosphorous based coupling agents, or between unreacted surface hydoxide groups.

Thiol Coupling Agents

Thiol groups show remarkable affinities and strong interactions with surfaces of metal nanoparticles. Thereby, the chemisorption energies, between sulfur and gold surfaces for example, are in the order of about $28 \, \text{kcal·mol}^{-1}$.[85,86] Two different kinds of interaction can be present. First adsorption of the still protonated X-SH molecules on the surface,[87] and second the chemisorption of the thiol, with the accompanied deprotonation of the thiol moiety, on the metal surface.[88] Extensive studies, spectroscopical and theoretical,[89] lead to the assumption of thiolate radicals bound to the surface with no metal-molecule charge transfer. Leff *et al.* calculated that for the described interactions there must be approximately two gold atoms on the surface per thiol.[86]

Two synthetic approaches are generally possible to obtain thiol capped metal nanoparticles. As already described before, Brust *et al.* synthesised gold nanoparticles capped with alkanethiols in a one step process. Fleming *et al.*, on the other hand, used a two step approach. Here, pre-synthesised gold nanoparticles were afterwards treated with the appropriate thiol capping agent. This way, the citrate,

used as a stabiliser for the nanoparticles, was exchanged through the thiol moieties. Furthermore, also thiol-thiol exchanges are possible,[90] but one has to keep in mind that only a certain ratio can be exchanged and the resulting layers will inevitably contain both molecules of thiols.

1.2.4   Assembly of Nanoparticles

Consequently, after the synthesis of nanoparticles, the controlled assembly and positioning of these is under intensive investigation and presents a key role for the formation of materials with advanced functions.[19] This stems from the fact, that in hybrid nanomaterials, consisting of both inorganic nanoparticles and organic counterparts, the desired properties are often lost due to poor dispersion of each component within the complementary material. The driving forces for the formation of assemblies, as for the synthesis of nanomaterials, can vary from covalent, van der Waals, ionic, hydrogen to colloidal interactions.[91] In general two synthetic pathways are offered for the formation: the synthesis of the particles and their assembly in one step, or two consecutive steps. For the first strategy many examples are given in nature, e.g. biominerals or mesocrystals. Mesocrystals are composed of individual nanoparticles, or to be more specific nanocrystals, and stabilised through organic molecules, which are ordered in a crystallogrphically oriented way. Their size can reach from some hundred nanometers to micrometers.[92] Since the properties of such arrays are rather difficult to predict, the second pathway is more often used to gain assemblies of nanoparticles.

In the second approach different research groups start with the surface functionalised metal of metal oxide nanoparticles.[93–98] Again, two approaches are possible. Wang *et al.* for example, functionalised gold nanoparticles with dithiols, or silver nanoparticles with dicarboxylates.[98] In this way an interparticle linkage was gained, leading to the formation of thin films. These films exhibit interesting electrical and optical properties dependent not only on the particle size, but also on the interparticle spacing parameters.

If no difunctional molecules are used, the linking unit has to be build up between two different funtionalities of already modified nanoparticles. Liu *et al.* established a connection between gold particles through a Diels-Alder reaction.[96] It was shown, that these assemblies feature enhanced photoluminescent properties. Further, such materials feature interesting characteristics, such as electron transfer-based applications,[99,100] optoelectronics,[101] or in the field of bio-medicine.[102]

1.3   Ionic Liquids

Beside nanoparticles, ionic liquids are a group of materials gaining more and more attention in the chemical community. Ionic liquids are per definition salts with low melting points, preferably below 100 °C, which is the case for room temperature ionic liquids.[103] Contrary to this rather vague definition most ionic liquids consists of the similar building blocks, an organic cation and an inorganic, often polyatomic, anion. The first reported room temperature ionic liquid dates back to the early 20th century, when german-baltican chemist Paul Waldon synthesised ethylammonium nitrate,[104] which exhibits a melting point of 13 °C.[105]

Until their rediscovery in the 1960s, through scientist at the U.S. Air Force aiming to synthesis new electrolytes, investigations on ionic liquids received no, or very low consideration.[103] In these researches ionic compounds with chloraluminates were studied. Later in the 1980s several groups studied the potential in preparative chemistry of these chloroaluminates, by stabilising various new transition metal complexes, such as molybdenum,,[106] tungsten,[107] or copper chlorides.[108] Further, Boon *et al.* studied their use for organic reactions, such as Friedl-Craft alkylation reactions.[109] However, the major drawback these ionic liquids suffer from is, that chloroaluminates are moisture and air-sensitive.

Through the introduction of different anion, such halides, nitrates or tetrafluoroborate,[110] stable ionic liquids could be achieved. This opened the door for many different applications, such as reaction medium for various organic reaction,[111] e.g. Beckmann rearrangements,[112] BaeyerVilliger reactions,[113] or Heck coupling reaction.[114] Thereby, a broad variety of cations and anions have been developed (Figure 1.9 and 1.10).
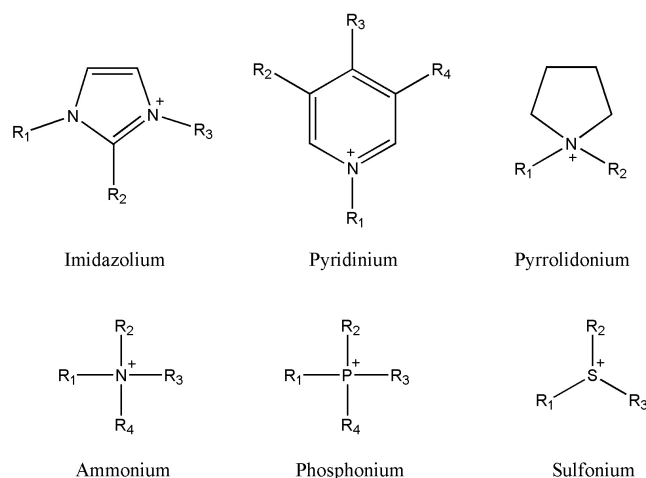

Figure 1.9: Chemical structure of various cations.

As for the organic reactions carried out in ionic liquids, it could be shown, by Earle *et al.*, that the anion of the ionic liquid influences the products of a chemical reaction.[115] For example, the usage of triflate and hydrogensulfate ionic liquids, together with nitric acid yield a nitrated product, whereas a halide anion with nitric acid outputs monohalogenated products. This is also enabled by the fact, that the anion tremendously influences the physical properties of the ionic liquid, including not only the melting point, but also the hydrophilicity, hydrophobicity.[103] In the case for imidazolium based ionic liquids, the alkyl chains as moieties have also to be taken into account, halides or tetrafluoroborate as anions lead to hydrophilic properties, whereas hexafluorophosphate and bis(trifluoromethylsulfonyl)imide induce water immiscibility.
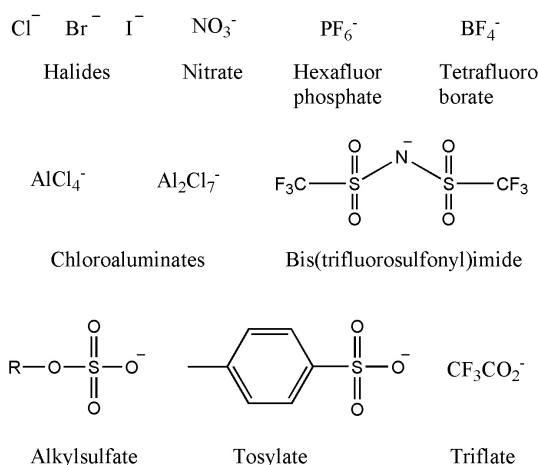
Figure 1.10: Chemical structure of various anions.

Next to the discussed physicochemical characteristics, many other properties, e.g. thermal stability, low vapour pressure, electric conductivity, or high heat capacity,[103] make ionic liquids interesting compounds for various chemical and also industrial applications. As an example for applications, Fredin *et al.* showed the possibility of ionic liquids for the use of electrolytes for dye-sensitised solar cells.[116] They recorded the influence of the anion on the power conversion efficiency of the solar cell.

As for the industrial applications the most renown process for ionic liquids is the BASIL^TM process, developed by BASF. In this process *N*-methylimdiazole acts as scavenger for hydrochloric acid. The resulting imidazolium based ionic liquids is liquid at the used conditions and therefore easy to separate, contrary to solid ammonium salts which have to be filtered off. Furthermore ionic liquids gained interest for liquid–liquid extraction processes, since conventional solvents are often toxic,

flammable, and volatile.[117]

1.3.1 Ionic Liquids in Hybrid Materials

Recently there have been many investigations about ionic liquids incorporated into, or bonded on, inorganic materials. Thereby, the motivation for these researches is often the synthesis of heterogeneous catalysts which contain the properties of ionic liquids and nanomaterials.

Many groups studied the immobilisation of ionic liquids either on silica particles,[118,119] or porous materials based on silica.[119–121] The immobilisation of the ionic liquids can be applied in two approaches. The first approach is a one step approach, were the silica matrix is reacted with the already synthesised ionic liquid. Through tri-alkoxysilane groups, as shown in the previous chapter, a covalent bonding is enabled.[121] The second pathway consist of incorporating the initial state of the cation first—in the case of the imidazolium this would be the imidazole—and afterwards the synthesis of the ionic liquid is induced through addition of the desired alkylhalide. This two step way was shown by Park *et al.* for the modification of multi-walled carbon nanotubes.[122]

Further, the incorporation of ionic liquids into inorganic materials, where no covalent bonding between the two components are present, unlike the examples mentioned above, presented an interesting task for some research groups.[123,124] Thereby, the inorganic matrix is a silica gel, prepared through the already described sol-gel process. The preparation of these hybrid materials was achieved either through a one step process through reaction of silica sources in the presence of various ionic liquids,[123] or previously synthesised silica gels were placed into various ionic liquids, resulting in filling of the pores.[124] The advantage of the resulting materials is, that these still offer typical characteristics for ionic liquids, e.g. ionic conductivity, or the influence of the anion on the stability of the resulting gels, while maintaining stable macroscopic solid systems.

Chapter 2

Goals of Work

The main focus of this project was to develop a facile strategy for the formation of new inorganic-organic hybrid materials based on silica nanoparticles and ionic linking units. Thereby, the work can be separated into four parts: synthesis and characterisation of a system based on silica nanoparticles, investigations of the influence of the different parts of this system, the deposition of the networks on a silicon substrate and finally the surface modification of cellulosic aerogels.

2.1 Synthesis of Silica Nanoparticle Networks

In the first part a straightforward synthetic route to construct silica nanoparticles, with diameters about 15 nm, connected trough ionic bridging units, containing one imidazolium moiety, had to be developed. Therefore, optimal syntheses were planned for the nanosized silica particles and the functional trialkoxysilanes, with which the surface modification was carried out. Furthermore, adequate measurement methods had to be found, in order to proof the successful networking of the silica nanoparticles.

2.2 Alteration of the Network

In the second part the influence of the different parts of the nanoparticles network, the kind of nanoparticles, linker and anion, on the properties of the hybrid material, had to be investigated. Different synthesis routes for the formation of transition metal oxide nanoparticles, and phosphonic acid coupling reagents, were chosen. Furthermore, various linking molecules and inorganic salts were selected to exchange and vary the bridging units and the counteranion, respectively.

2.3 Deposition of Layers of Nanoparticle Networks on Silicon Substrates

Another goal of this work, was the deposition of the obtained nanoparticle networks onto to silicon substrates. Therefore, a route for covalently linking modified titania nanoparticles onto silicon wafers was worked out. Especially the stabilities of the resulting mono- and multilayers were of crucial interest.

2.4 Surface Modification of Cellulosic Aerogels

The last point of interest was to investigate the surface functionalisation of cellulosic alcogels with tri- or tetraalkoxysilanes. Thereby, different combinations of two silica precursors, prior to supercritical drying, were chosen. One of the main subjects was to sustain certain properties, e.g. porosity and surface area, of the resulting cellulosic aerogels.

Chapter 3

Silica Nanoparticle Networks

In this chapter silica nanoparticles linked by one imidazolium unit will be investigated. Two main aspects are decisive for the choice of silica nanoparticles: first, as pointed out in Chapter 1.2.1, the synthesis of silica nanoparticles through the sol-gel process is well studied throughout scientific literature, based on the fact, that a broad field of applications for silica nanoparticles exist, such as catalysis or biomedical drug delivery,[125,126] and second, the precursors are rather inexpensive, compared to educts for transition metals. This system will serve as the "model system" for the alteration and fabrication possibilities shown in the following chapters.
To gain such networks, the silica nanoparticles were surface modified with functional trialkoxysilanes to undergo further nucelophilic substitution reactions. Through the nucelophilic substitution reactions, the imidazolium units form, bridging the silica nanoparticles and finally leading to silica nanoparticle network. To follow the synthesis of these networks, several different measurement techniques were used.

The three individual steps; the synthesis of the silica nanoparticles, their surface modification with functional trialkoxysilanes, and the final nucelophilic substitution reactions to form the imidazolium bridging units, will be discussed in the following chapters in detail.

3.1 Synthesis of Silica Nanoparticles

Following a literature known protocol, published by Stöber *et al.*,[127] tetraethylorthosilicate (Figure 3.1), as the silica source, is reacted in a polar solvent, in this case methanol, under the use of basic catalyst, NH_3. As shown in chapter 1.2.1, the usage of a base will lead to spherical nanoparticles. In this *bottom up* approach, as

in sol-gel processes in general, the ratio between the solvent, precursor and catalyst determines the size of the nanoparticles. Stöber *et al.* showed, that silica particles with sizes ranging from 50 nm to about 2000 nm can be prepared.
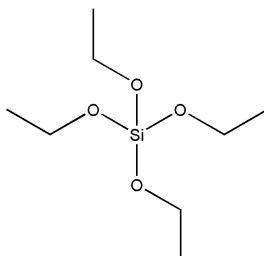

Figure 3.1: Chemical structure of tetraethylorthosilicate.

By reducing the volume of the catalyst—in the publication of Stöber *et al.* 2 ml ammonium hydroxide in 50 ml ethanol were used to synthesise silica nanoparticles with 50 nm diameter—to 60 μl of NH_3 in 100 ml solvent and 10.41 g of TEOS, particles below the reported sizes, below 20 nm, can be obtained. The size of the synthesised silica nanoparticles was determined through dynamic light scattering (DLS) measurements (Figure 3.2). Therefore, a sample was taken directly from the reaction solution and diluted. The measured sample shows a signal centred at 8 $\pm$ 2 nm radius. Thereby, the nanoparticle suspension is stable for several days up to weeks, due to the electrostatic repulsion of the negatively charged surfaces, deriving from the basic condition of the reaction medium. Further, a transmission electron microscopy (TEM) image (Figure 3.2) shows uniform nanoparticles, considering the size and shape, with diameters around 15 nm.
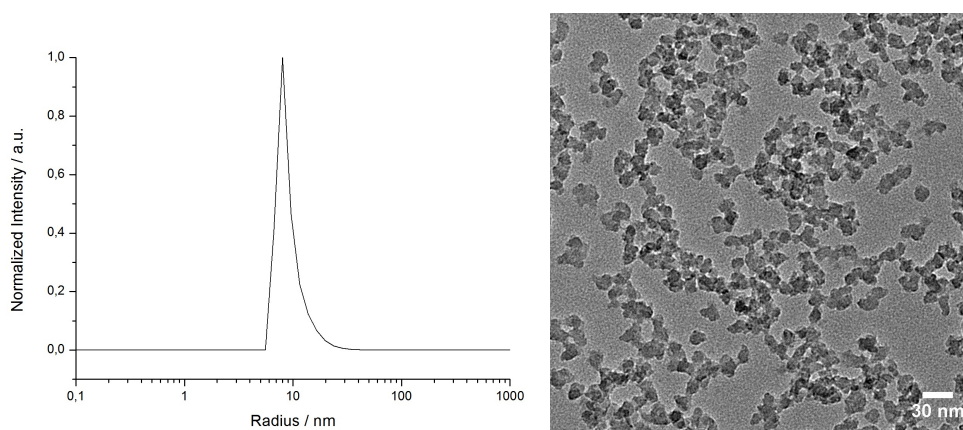

Figure 3.2: DLS (left) and TEM (right) measurements of silica nanoparticles.

An important aspect drawn from DLS and TEM measurements is, that no agglomeration of the particles is visible. This can also be seen with the naked eye, given, that agglomeration would lead to turbidity of the silica nanoparticles suspension, which was not the case.

3.2   Surface Functionalisation of Silica Nanoparticles

For the introduction of functional groups on the particles surface, trialkoxysilanes were chosen due to their controllable reactivity towards sol-gel reactions.[20,70] For the aimed purposes functional trialkoxysilanes containing either a halogen or imidazole end group are required. The halogen bearing compound 3-chloropropyltrimethoxysilane was chosen, since it is commercially available and still reactive enough to form ionic briding units.

For the synthesis of the imidazolesilane, a pathway described by Cazin *et al.* was followed (Figure 3.3).[128] Thereby, 3-chloropropyltrimethoxysilane was reacted, in a Finkelstein reaction, with sodium iodide in acetone. In this S_{N2} subsitution reaction the halogens are exchanged, the driving force for this reaction comes from the insolubility of sodiumchloride in acetone, whereas sodiumiodide is soluble in this solvent. 3-Iodopropyltrimethoxysilane is gained after filtration of sodium chloride. In parallel, sodium imidazolide, which is synthesized through the addition of a strong base to imidazole to form the deprotonated anionic imidazolide, was added to achieve *N*-(trimethoxysilylpropyl)imidazole.
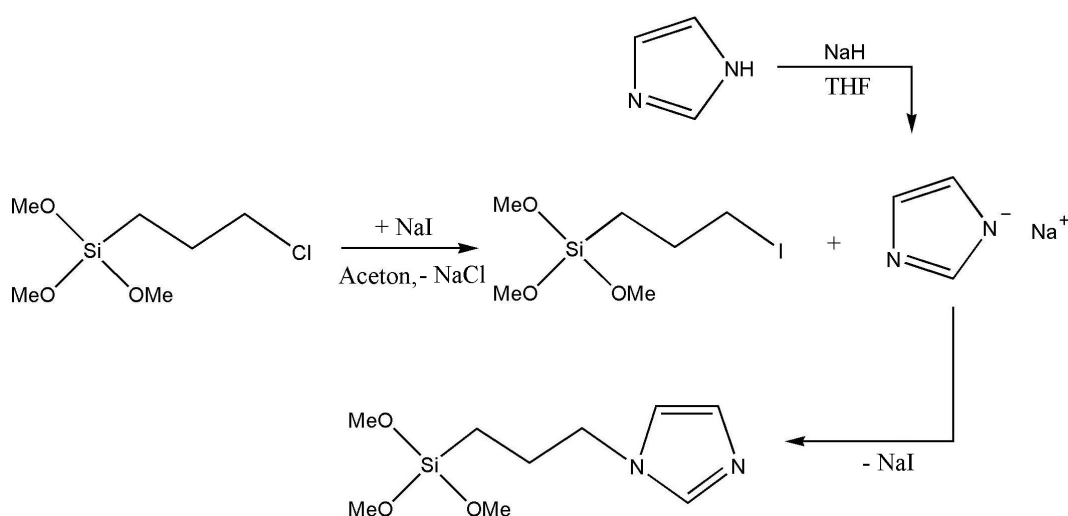

Figure 3.3: Synthesis of *N*-(trimethoxysilylpropyl)imidazole.

After the synthesis of the appropriate silane, the surface modification of the silica nanoparticles was carried out directly from the suspensions, obtained in the Stöber process. Two batches were prepared, one modified with 3-chloropropyltrimethoxysilane and one with N-(trimethoxysilylpropyl)imidazole. Afterwards, as for the plain silica nanoparticles, DLS measurements were carried out to investigate the evolution of the radii of the nanoparticles after modification (Figure 3.4). For both kind of surface modificiations a slight increase in the radius can be observed. It has to be noted, that using DLS the hydrodynamic radii of the nanoparticles are measured. This derives from the interaction of the surfaces of the nanoparticles with the solvent molecules, thus forming a solvation shell, which is measured by DLS. The DLS signal for imidazole modified nanoparticles is centered on 10 nm, whereas the measurement for chloro funtionalised particles exhibits a radius of about 11.5 nm. Another information, drawn from optical observations, is, that again no agglomerates of silica particles during the modification process occurs, since the samples exhibit no sign of turbidity.
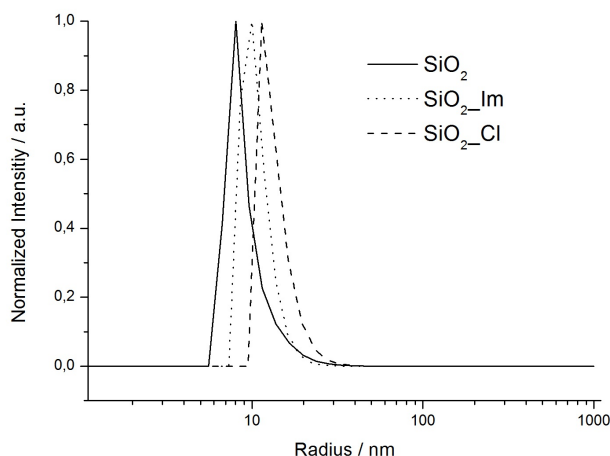
Figure 3.4: DLS measurements before and after modification with either imidazole or chloro bearing trialkoxysilanes.

3.3   Synthesis of Silica Nanoparticle Networks

The third and last step consists of the nucleophilic substitution reaction between the imidazole and chloro modified silica nanoparticle batches. This reaction results in the formation of the imidazolium entities and follows in principle the synthesis of ionic liquids. It is induced by mixing the two batches in a volume ratio of 1 to 1 and heating it to reflux for 24 hours. Afterwards the solvents were removed,

the crude product washed several times with ethanol, acetone and water. After drying the white powder in a desiccator over P_2O_5 various analyses could be carried out.

To confirm, the presence of the organic linking unit between the silica nanoparticles, which formed during the nucelophilic substitution reaction, a ^{13}C solid state cross-polarised magic angle spinning nuclear magnetic resonance (CP MAS NMR) spectrum was recorded (Figure 3.5). In the spectrum, the characteristic peaks of the 1,3-dipropylimidazolium link can be observed. The signals at lower field, 135 and 122 ppm derive from the three imidazolium ring carbon atoms, whereas the three remaining signals at higher field, at 48, 16 and 3 ppm, correspond to the carbon atoms of the alkyl chains between the nitrogen and the silicon atoms. However, in the solid state spectrum the formation of the imidazolium units can not be followed, as the shift of the peaks, between the imidazole and imidazolium, is too small, when compared to the peak resolution. These results are only an indication of the presence of the organic linking units inside the final material.
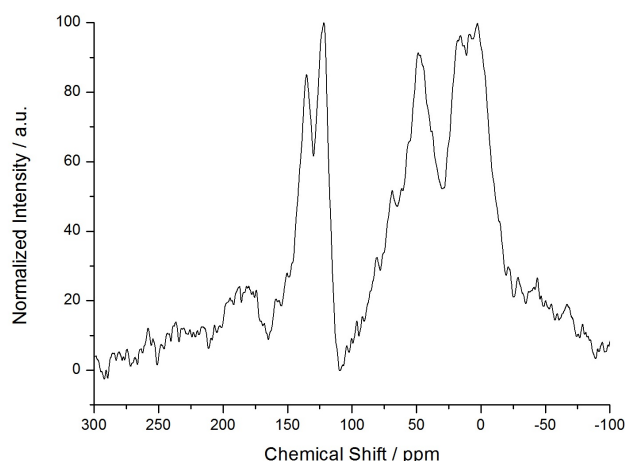
Figure 3.5: CP MAS ^{13}C NMR spectrum of silica nanoparticle networks.

Further, thermogravimetric analyses, for the final nanoparticle networks and the differently modified silica nanoparticles, were carried out (Figure 3.6). It can be seen, that the onset temperature of the degradation varies for the differently modified nanoparticles and the nanoparticle networks. The measurements for the chloro and imidazole surface modifications show onset temperatures at 170 and 250 °C, respectively. Thereby, the mass loss below a temperature of 170 °C can be attributed to the degradation of absorbed solvent molecules, in this case water and methanol and above, until 250 °C, to the degradation of unbound ligands. For the connected networks an increased onset degradation temperature, starting around

300 °C, is observed. This temperature is typical for ionic liquids containing chloride anions.[103,129,130] Between 170 and 300 °C a weight loss of about 6 % can be seen, which corresponds to about 13 % of unreacted ligands, keeping in mind a weight loss of 48 % between 170 and 650 °C. After a temperature of 650 °C the degradation of the organic moieties is finished and a white powder, SiO_2, is left. These investigations are an indication, that the nucleophilic substitution reaction was successful, although some unreacted ligands seem to be present within the system. Usually also the amount of ligands bound to the surface of the silica nanoparticles can be calculated from TGA measurements.[131] Since monolayers are required to calculate the ligands per nm^2, these calculations can not be applied in this case, since trialkoxysilanes can form multilayer (Chapter 1.2.3), and therefore lead to incorrect values.
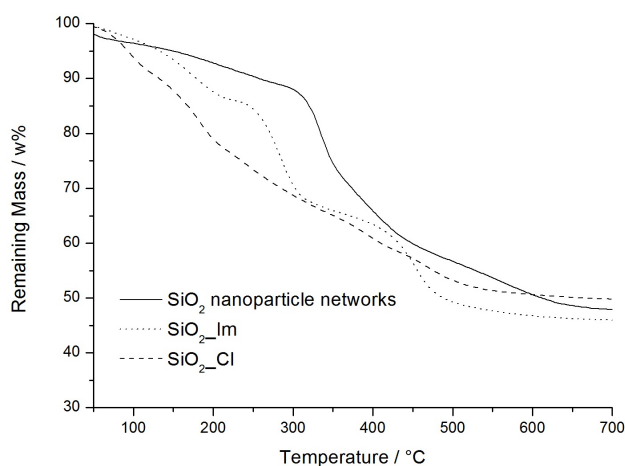
Figure 3.6: TGA measurements of differently modified silica nanoparticles and nanoparticle networks.

To gain direct information about the state of the imidazolium units, ^{15}N solid state NMR measurements were carried out. For reference, 2-D $^{1}H/^{15}N$ heteronuclear multiple-bond correlation spectroscopy (HMBC) experiments with nitrogen containing compounds were measured.

First, N-methylimidazole was measured to determine the signals for the nitrogen atoms (Figure 3.7). It can be observed, that the nitrogen atoms interact with the hydrogen of the methyl group, as seen by the signals at 3.5 ppm in the ^{1}H spectrum. Two main peaks are visible, one at 140 ppm and the other at 240 ppm. It is known from literature,[132] that the peak at higher fields can be attributed to the nitrogen right next to the methyl-group. To determine the effect of the conversion of the imidazole into imidazolium units, next to N-methylimidazole also 1-butyl-

3-methylimidazolium hexafluorophosphate ([BMIm][PF$_6$]) was measured. Through this nucleophilic substitution reaction, which also occurs during the formation of the nanoparticle networks, the chemical shifts can be tracked, since it yields to 100 % imidazolium units (Figure 3.7). As a result, a chemical down field shift of 9 ppm between the imidazole and the imidazolium units can be observed, also reported by several groups. [133–136]
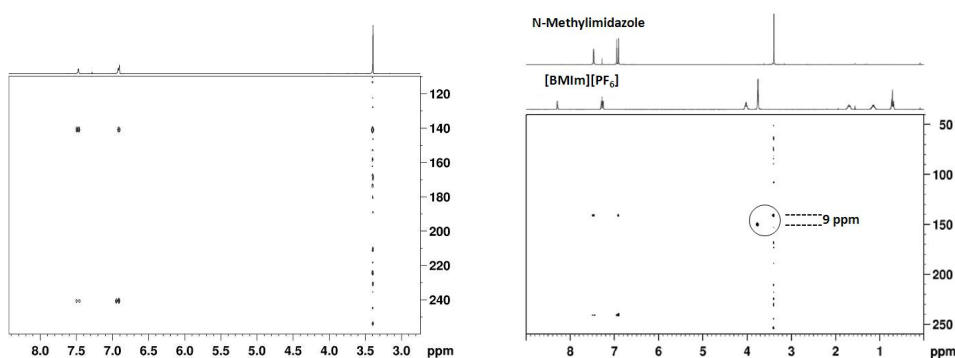
Figure 3.7: ^{1}H/^{15}N HMBC spectrum of *N*-methylimidazole (left) and *N*-methylimidazole and [BMIm][PF$_6$] (right).

This chemical shift can also be seen in the ^{15}N solid state NMR spectrum of the silica nanoparticle networks (Figure 3.8). In the spectra, a broad peak around 145 ppm can be observed, with a shoulder at 135 ppm (Figure 3.8).
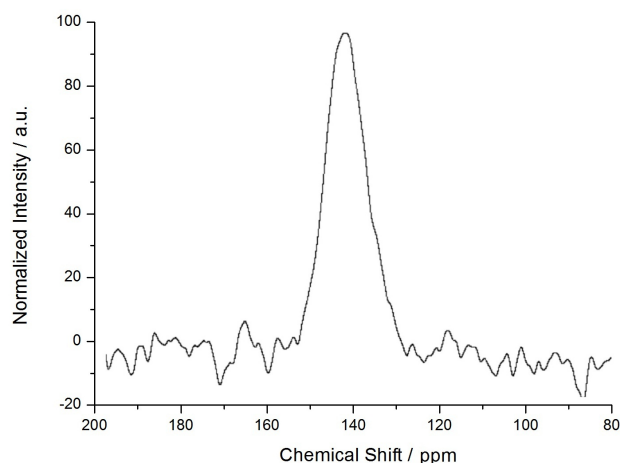
Figure 3.8: ^{15}N CPMAS spectra of the synthesised silica nanoparitlce networks.

From the reference experiments the shoulder at higher field in the ^{15}N solid state

spectrum of the networks can be attributed to non-reacted imidazole units, whereas the peak around 142 ppm corresponds to the imidazolium linking units. Considering the pattern obtained through HMBC experiments another peak around 240 ppm should be visible for the unreacted imidazole units, but given the low total amount of imidazole groups in the system, this peak disappears in the noise of the spectrum, already reported by other groups.[132,135] A quantification of the amount of reacted species can not be conducted, since the ^{15}N solid state MAS NMR spectrum was recorded under cross polarisation conditions, a technique, where the magnetisation of neighbouring hydrogen atoms is transferred to the probed nucleus, nitrogen, and thus the amount of hydrogen influences the peak intensities. Due to the very low natural abundance of the ^{15}N isotope, 0.366%, as well as the low amount of nitrogen atoms in the material, solid state MAS NMR spectroscopy, without cross-polarisation, would extend the measurement time dramatically. It has to be noted, that already with cross-polarisation approximately 400000 scans, requiring two to three days of measurement time, are needed to gain a ^{15}N spectrum.

To evaluate the organization of the silica nanoparticle networks, small-angle X-ray scattering (SAXS) was measured (Figure 3.9), which gives access to the size, distance, and arrangement of nanosized objects.[137] In the measured spectrum a trimodality can be observed. The broad peak at high q-values around $15\,nm^{-1}$ corresponds to amorphous silica, deriving from the arrangement of the silica tetrahedrons within the nanoparticles.[138] Additionally, two features are observed around $q = 0.4\,nm^{-1}$ and $5\,nm^{-1}$. These two peaks are due to the arrangement of the nanoparticles within the constructed network.
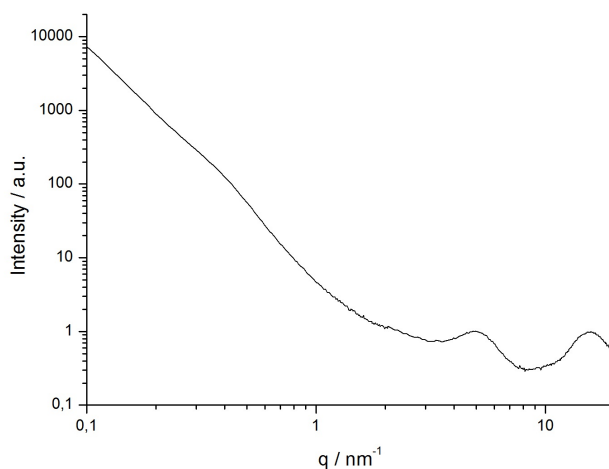

Figure 3.9: SAXS measurement of the silica nanoparticle networks.

To gain a numerical description of the silica nanoparticle networks, an approach by Beaucage is used. This approach was developed for system showing microstructural features on many length scales and more specifically for concentrated nanoparticle systems. Thereby, the approach is split into several terms of levels of structure, whereat each level corresponds to a Guinier regime combined with a structurally limited power-law regime.[137] The power-law regime describes the properties of the structure, while the Guinier regime the size.

In the present case, the scattering curve presents a two-level system, indexed by the subscripts for the following parameters. The calculations of these parameters were performed through iterative fitting by Mathematica®. In order to find appropriate starting values for the final approach, first, fitting was carried out only for high q-values, for one distribution, and afterwards at low q-values. The approximation of the scattering curve can be expressed through the following equation:

$$
\begin{aligned}
I(q) = \ &\Phi(q, k_1, d_1)(g_1 exp(-q^2 r_{g1}^2/3) + \\
&b_1 exp(-q^2 r_{g2}^2/3)((erf(qr_{g1}/\sqrt{6}))^3/q)^{p1}) + \\
&\Phi(q, k_2, d_2)(g_2 exp(-q^2 r_{g2}^2/3) + \\
&b_2 exp(-q^2 r_{g2}^2/3)((erf(qr_{g2}/\sqrt{6}))^3/q)^{p2}) + BGR
\end{aligned}
\tag{3.1}
$$

Here, g_i and b_i are prefactors, determined by the scattering contrast of the two phases, the number of scattering particles, and the intensity of the beam, used for the measurement. In the equation the expression "erf" described the error function and BGR a factor, deriving from a constant low background from parasitic scattering due to residual air. Furthermore, for weak ordering, which frequently occurs in concentrated systems, an interference function $\Phi(q, k, d)$ is introduced. This interference function describes the concentration effect due to a close packing of the nanoparticles:

$$
\begin{aligned}
\Phi(q, k_1, d_1) &= \frac{1}{1 + k\theta(q, d)} \\
\theta(q, d) &= 3\frac{sin(qd) - qdcos(qd)}{(qd)^3}
\end{aligned}
\tag{3.2}
$$

Next to described prefactors, g_i and b_i, the evaluation of the SAXS measurements through the approach by Beaucage, delivers a number of important parameters: r_g, the radius of gyration (generally derived by the Guinier's law at small q-values),[137] d_i, the distance of correlation of the building blocks, p_i, the fractal dimension, and k_i, the packing factor of the respective distribution.[137] Thereby, the radius of gyration is

linked to the diameter $\oslash$ of spherical nanobuilding blocks by the following equation:

$$\oslash = 2r = 2\sqrt{\frac{5}{3}}r_g \tag{3.3}$$

Through the mathematical approximation, the intensity decrease of the second distribution (at low q-values) is close to q^{-4}. Thus, p_2 was set to 4 to reduce the number of parameters, which is based on the assumption of a two-phase material with a sharp interface, between the silica nanoparticles and the organic moieties, at this size level. The resulting numerical data of the described parameters are summarized in Table 3.1.

Table 3.1: Parameters obtained from mathematical approximation of SAXS measurements.

r_{g1} / nm	$\oslash_1$ / nm	k_1	d_1 / nm	p_1	r_{g2} / nm	$\oslash_2$ / nm	k_2	d_2 / nm
4.8	12.5	2.2	13.5	3.6	0.7	1.8	7.5	1.1

Here, the numerical value of p_1 is also close to 4, which indicates a sharp interface of the large nanoparticles. This is reasonable, as the scattering contrast of the silica particles is considerably higher than that of the organic linkers. Further, the diameter of the nanoparticles, $\oslash_1$, is in the range of 12.5 nm. This corresponds to the values obtained through DLS measurements, without the solvent shell, and is in the area expected from the Stöber process, which was used to synthesise the silica nanoparticles. Additionally, a distance of correlation, d_1, of 13.5 nm was obtained. This distance can be related to two half-nanoparticle diameters plus the linker length, l (Figure 3.10). The value l is about 1 nm, which corresponds well to the expected size of a 1,3-dipropylimidazolium unit. This correlation distance is connected to the packing factor, k_1, of 2.2. This packing factor is similar to the probability to find another unit within the range of a sphere with a certain radius, the so-called hard sphere volume ratio in a hard sphere model.[139] Thereby, a factor of $k_2 = 3$ corresponds to a hard sphere volume ratio of 0.13, whereas a factor of 9 to a ratio of 0.21. Thus, and this important, d_1 and k_1 reveal a short-range order within the silica nanoparticles networks.

As said in the beginning, the Beaucage approximation is generally suitable for structures with multiple orders of hierarchy, through introduction of an additional factor for small structures, at high q-values in reciprocal space. This structural factor, d_2,

is attributed to the distance of the imidazolium units. The amount of short-range order of the imidazolium units is described by the second packing factor k_2. In the case of the silica nanoparticle networks high packing values of 7.5 are obtained, attributed to the $\pi - \pi$ stacking of the imidazolium rings. Such stacking phenomenons of imidazolium rings were already reported for constrained systems. [140–142] Through the molecular confinement of ionic liquids, e.g. in a silver matrix, [140] $\pi - \pi$ stacking can occur through an interaction with the surface of the matrix.
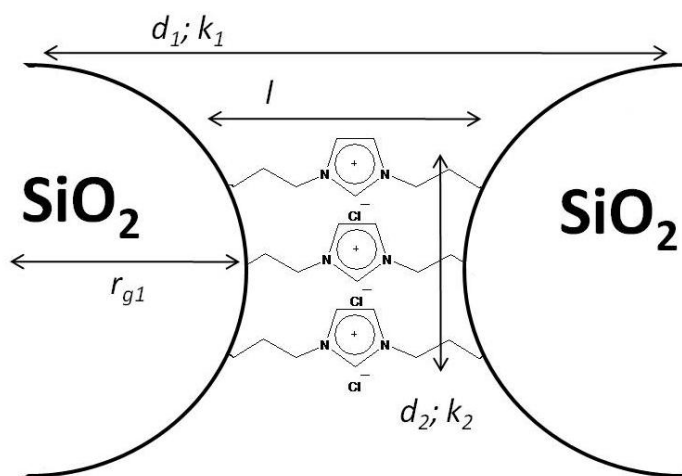
Figure 3.10: Assignment of the parameters introduced for the mathematical fitting of the SAXS measurements.

3.4   Conclusion

The synthesis of the "model system" based on silica nanoparticle was divided into three separate steps. The first step, the synthesis of silica nanoparticles, was achieved through a *bottom-up* approach to yield spherical nanoparticles with sizes around 15 nm. The second step, the functionalisation, was carried out by using functional trialkoxysilanes and confirmed through DLS and TGA measurements. The last and crucial step, the construction of the networks, was established through a nucleophilic substitution reaction of the differently modified nanoparticles. The efficiency of this method was proven through TGA, solid state NMR and SAXS measurements. Thereby, a short-range order of the silica nanoparticles in the networks could be observed.

Chapter 4

Alteration of the Networks

In order to investigate the influence of the different components of the synthesised hybrid materials based on silica nanoparticles and ionic linkers, three options are offered. First, the nanoparticles can be varied. Here, many different kinds of metal oxides can be synthesised, depending on the desired application (Chapter 1.2.1). Second, the linker between the nanoparticles can be altered, through introduction of alkyl or, more rigid, xylene ligands, and third, the anion of the system can be exchanged, through metathesis reactions.

4.1 Variation of the Metal Oxide Nanoparticles

In this chapter the variation of the metal oxide nanoparticles, will be investigated. Analogous to the already described silica nanoparticles (Chapter 3.1), metal oxide nanoparticles, titania, zirconia and iron oxide, were prepared through either sol-gel, hydrothermal decomposition or precipitation methods. After characterisation of the obtained nanoparticles, surface modifications, using phosphonic acids containing either chloro or imidazole functionalities, were carried out. A verification of the surface modifications were achieved through fourier transform infrared (FTIR) and TGA measurements. Afterwards, as shown for titania nanoparticles, the two differently modified nanoparticles batches were combined, to form the imidazolium bridging units. The received networks were characterised through SAXS, nitrogen sorption and solid state NMR measurements.

4.1.1   Synthesis of Metal Oxide Nanoparticles (Titania, Zirconia, Iron Oxide)

Titania Nanoparticles

Many different routes are known from literature to prepare titania nanoparticles, such as hydrothermal treatment, thermolysis or the sol-gel process.[143–145] Thereby, the chosen reaction conditions determine the crystalline structure of the nanoparticles. Anatase nanoparticles can be obtained at low reaction temperatures, whereas rutile only forms at higher temperatures.[146,147] The third modification structure of titanium dioxide, brookite, is obtained under acidic conditions through precipitation methods.[148] Nevertheless, when heating to about $800\,°C$ again rutile is the only stable phase. As titanium source alkoxides, e.g. titanium isopropoxide $(Ti(O^iPr)_4)$ or salts, e.g. $TiCl_4$, can be used.

As the anatase modification offers interesting properties, such as the high photocatalytic activity, which can be useful for photovoltaic systems,,[149] a facile sol-gel route, developed by Choi *et al.*,[150] and later refined and further investigated by Ivanocivi,[151] was chosen. Following this method, titanium isopropoxide was added drop-wise to an aqueous solution, which pH was previously adjusted with HNO_3 to a value of about 1.5. Spherical titania nanoparticles were obtained after three days of stirring at ambient temperature. Using dynamic light scattering (DLS) the diameter of the particles can be estimated (Figure 4.1). Thereby, it can be observed, that the anatase nanoparticles are very well redisperseable in water. It can be seen, that nanoparticles with a narrow size distribution, with an average hydrodynamic diameter of $5.6 \pm 2\,nm$, are obtained. Further, it is notable, that through the drying and redispersion process, no agglomerates did form.

To verify these results, the size and crystallinity of the nanoparticles was also investigated with conventional powder X-ray diffraction (XRD, Figure 4.1). The X-ray diffractogram represents the characteristic reflexions for the anatase modification.
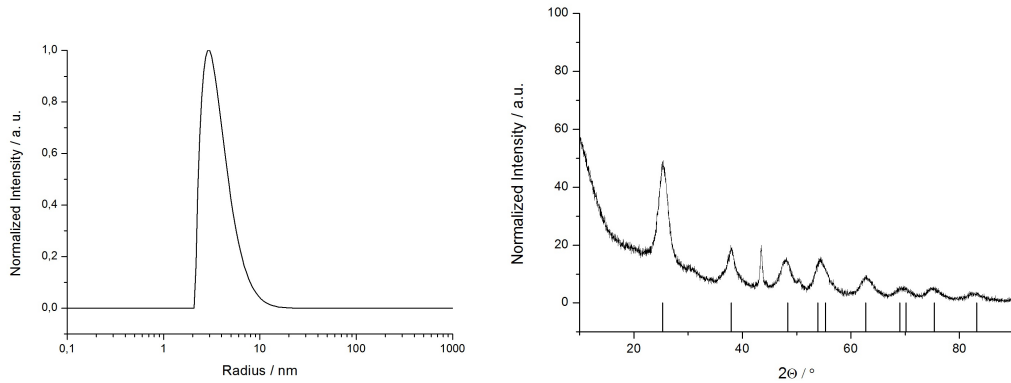
Figure 4.1: DLS of sol-gel synthesised anatase nanoparticles (left) and XRD pattern of sol-gel derived titania nanoparticles (right, bars: JCPDS # 01-0562 for anatase).

By applying the Scherrerr's equation (Equation 4.1) on the (101) reflexion at 25°, the size of the nanoparticles can be calculated:

$$D = \frac{K\lambda}{\beta \cos\theta} \tag{4.1}$$

Here, K is a form factor (0.9 for nearly spherical-shaped nanoparticles), λ the wavelength of the X-rays (1,5406 Å), β the line broadening at half the maximum intensity and θ the Bragg angle of the studied relfexion. This calculation affords an average diameter of anatase crystallites of 4.0 ± 0.7 nm. This result is slightly smaller than obtained through the DLS measurement. The reason for this can be found in the utilised methods. For XRD, dried nanoparticles were used, whereas in DLS the nanoparticles were measured in solution. As described in the previous chapter, due to the interaction of the particles with the solvent, the radii of the particles contain a solvent shell and appear bigger than in reality. TEM measurements were not applied in this case, since XRD and DLS measurements were in good agreement. For further calculations the diameter obtained through XRD calculations will be considered.

Zirconia Nanoparticles

Next to titania anatase nanoparticles, zirconia nanoparticles were synthesised. Zirconia nanoparticles possess interesting properties, e.g. the usage as catalyst.[152,153] As described in chapter 1.2.1 for the synthesis of highly crystalline nanoparticles, often a hydrothermal approach is used.
A pathway, developed by Murase *et al.* was followed.[17] This way, the zirconium

source, zirconium oxychloride octahydrate ($ZrOCl_2 \cdot 8H_2O$), was diluted to a 4 molar solution, and thermally decomposed at $200\,°C$ for 72 hours in an autoclave. After precipitation with acetone and washing with water and ethanol, to remove by-products, such as hydrochloric acid, the particles were subsequently dried. XRD experiments reveal the presence of baddeleyite, monoclinic ZrO_2, as the only phase (Figure 4.2). The other two phases, possible for ZrO_2, tetragonal and cubic, are formed only at high temperatures. From the XRD patter a crystallite size of $4.5 \pm 0.5\,nm$ could be calculated by applying the Scherrer's equation, described above, on the relexion at $29°$ (-111). These findings were compared with the TEM images (Figure 4.2). Thereby, rice-shaped nanoparticles can be seen, with an aspect ratio of about 2 to 3, and a equivalent spherical diameter of about 6 to $7\,nm$. These findings are slightly smaller as for the calculated values from the XRD, but are nevertheless in the same range.
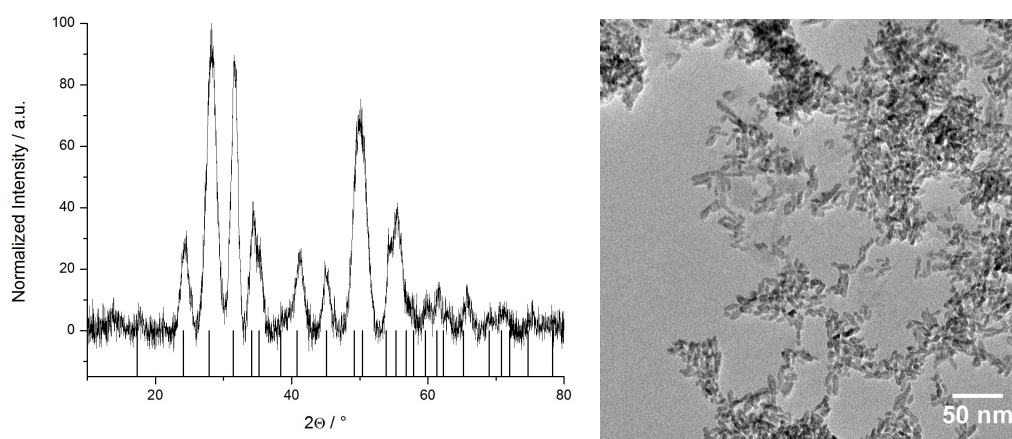
Figure 4.2: XRD of zirconia nanoparticles (left, bars: JCPDS # 01-0750 for baddeleyite) and TEM (right).

However, as shown by DLS (Figure 4.3), the particles are good redisperseable in water, a signal centred around $10\,nm$ radius can be found. This large deviation from the values obtained through the other methods was already reported in literature,[154] and is ascribed, on the one hand to the interaction of the surface with the solvent, thus representing the equivalent hydrodynamic radius, and on the other hand, the presence of agglomerates, due to the drying of the nanoparticles prior to measuring though DLS. Therefore, for further calculations the diameter obtained through XRD will be used.

Figure 4.3: DLS measurements of zirconia nanoparticles.

Iron Oxide Nanoparticles

The third system, under investigation, are magnetite, Fe_3O_4, nanoparticles. Magnetite nanoparticles have a broad field of applications, such as magnetic recording or for biomedical materials,[155,156] due to their magnetic properties. As described in chapter 1.2.1, for the synthesis of mixed oxide systems, magnetite consists of iron in the oxidation states 2+ and 3+, coprecipitation methods can be used.
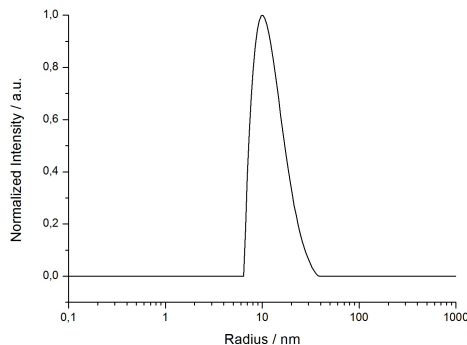
In order to obtain magnetic nanoparticles, a mixture of $FeCl_3$ and $FeCl_2$, in a molar ratio of 2 to 1, this ratio is also present in magnetite, dissolved in hydrochloric acid was coprecipitated.[56,157] Thereby, the precipitation was induced through the drop-wise addition of a base, in this case through a 25 % aqueous $N(CH_3)_4OH$ solution. The black precipitate, which appeared after some minutes, was dried and washed with water and ethanol, through magnetic decantation. Afterwards XRD measurements were carried out (Figure 4.4). In the pattern it can be seen, that magnetite is present as the only phase. Through the Scherrer equation (Equation 4.1), applied on the magnetite (311) relexion at 35°, an average diameter of magnetite crystallites of 21 nm $\pm$ 1 nm is afforded. In the TEM image spherical particles with a broad size distribution can be seen. Thereby, the diameter ranges from about 17 to 21 nm. These size distributions were already reported in literature,[157] and is due to the synthesis method. Through the drop-wise addition of the precipitation agent, the nuclei of the nanoparticles are not forming simultaneously, leading to differently growing nanoparticles.
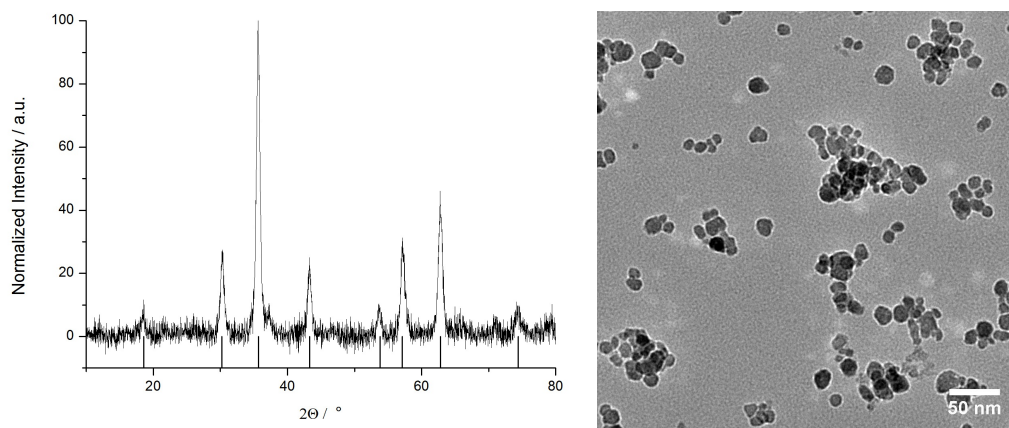
Figure 4.4: XRD of iron oxide nanoparticles (bars: JCPDS # 01-1111 for magnetite) and TEM micrograph.

A DLS measurement of in water redispersed and sonicated particles (Figure 4.5) shows a signal at around 21 ± 4 nm radius, which is about twice the size of the values obtained through XRD and TEM. This can be explained by the fact, as for the zirconia nanoparticles, that again the hydrodynamic radius is measured through DLS. Furthermore a small signal around around 80 nm radius represents agglomerates of magnetite nanoparticles. These agglomerates can be seen, besides in the TEM image, with the naked eye when the nanoparticles are, once dried, redispersed in water.

Figure 4.5: DLS measurements of magnetite nanoparticles.

4.1.2   Surface Functionalisation of Metal Oxide Nanoparticles

Unlike silica nanoparticles, transition metals, in particular titanium dioxide, can form labile, hydrolyzeable bond, when silanes are used as ligands.[77,158] As discussed in Chapter 1.2.3, organophosphonates form covalent M-O-P bonds, but not in the

case of silica. For the construction of nanoparticle networks, two phosphonic acids had to be synthesized, one bearing a chloride funcionality, and the complimentary containing an imidazole moiety.

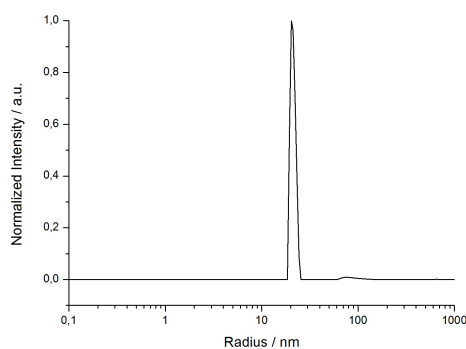3-Chloropropylphosphonic is prepared via a modified *Michaelis-Becker* reaction and subsequent hydrolysis with hydrochloric acid (Figure 4.6).[159] This reaction, where dimethylphosphite is deprotonated with a base, offers the advantages that neither high reaction temperatures nor distillation of the product are necessary. Afterwards, the potassium dimethlyphosphite salt is directly reacted with 1-bromo-3-chloropropane. Thereby, potassiumbromide is obtained and the phosphite selectively attacks the alkyl bromide site, since bromide is a much better leaving group than chloride. After the hydrolysis of the ester the phoshonic acid is recrystallised from chloroform.
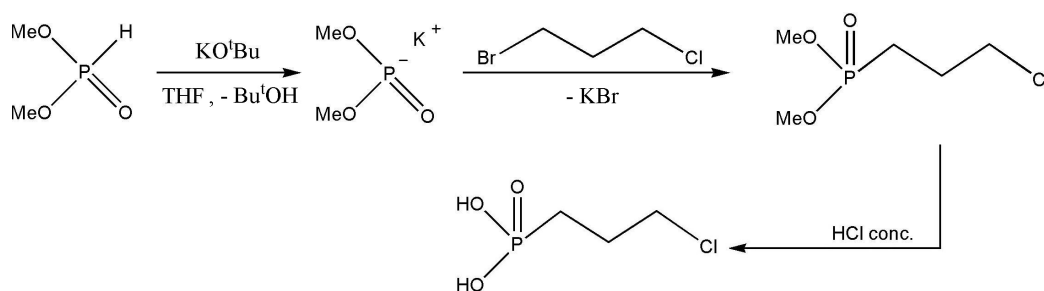
Figure 4.6: Synthesis of 3-chloropropylphosphonic acid.

It has to be noted, that the *Michaelis-Becker* reaction is less used than the well known *Michaelis-Arbuzov* reaction,[160] as it it used for the formation of the imidazole counterpart, *N*-imidazolylpropylphosphonic acid (Figure 4.7), since two synthesis steps are requires.[161] The *Michaelis-Arbuzov* process proceeds through a S_{N2} mechanism. The trialkyl phosphite is used in an excess compared to the 1,3-dibromopropane. Again, the phosphor attacks on the alkylbromide with its lone pair and, in the transition state, a rearrangement takes place to eliminate an alkyl bromide. It is obvious, that by using dibromine compounds also disubstituted alkyl-chains can be formed. Therefore, distillation of the diethyl-3-bromopropylphosphonate is necessary. Afterwards the addition of the imidazole moiety takes places as for the silane coupling agents (Chapter 3.2). After the addition is complete, the hydrolysis of the ester can be achieved through addition of hydrochloric acid, as it was done for 3-chloropropylphosphonic acid, or through the usage of trimethylsilyl bromide (TMSBr).[162] In both ways the the protonated form of *N*-imidazolylpropylphosphonic acid is obtained.
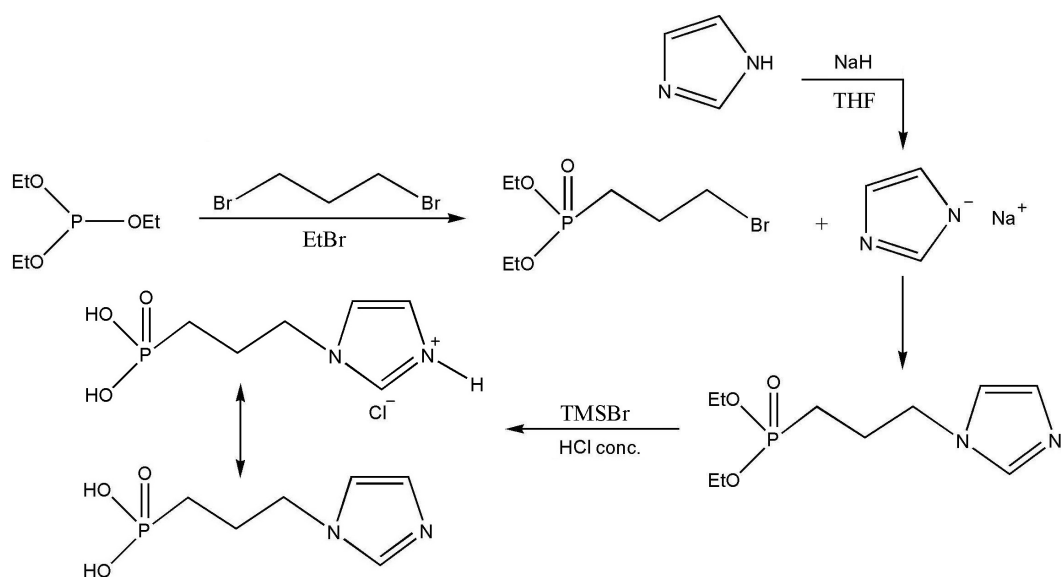
Figure 4.7: Synthesis of N-imidazolylpropylphosphonic acid.

The reason for this protonation of the imidazole can explained by its chemical nature.[163] Since the pk_a, the logarithmic acid dissociation constant, of imidazole is about 7, imidazole acts as a proton acceptor above a pH of 7, whereas at lower pH values the protonated, imidazolium form is present. Since the proton is only loosely bound the imidazole, it still can be used to create nanoparticle networks through nucelophilic substitution reaction with halogen bearing counterparts.

An important point, using this pathway is, that at least three CH_2 groups between the bromide and the phosphour atom are needed. Experiments with diethyl-3-bromoethylphosphonate showed that β-elimination reactions occur, when a base, in this case sodium imidazolide, is added if a shorter alkyl chain is used (Figure 4.8). Thereby, the base deprotonates the β-C atom and diethyl-vinylphosphonate is formed.
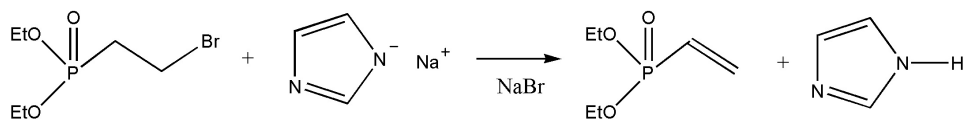

Figure 4.8: Elimination reaction of diethyl-3-bromoethylphosphonate leading to diethyl-vinylphosphonate.

Titania Nanoparticles

The modifications of titania nanoparticles with the synthesised phosphonic acids were carried out in water. Therefore, $1\,g$ dried titania nanoparticles together with $1.54\,mmol$, either $0.244\,g$ 3-chloropropylphosphonic acid (TiO$_2$_Cl) or $0.293\,g$ N-imidazolylpropylphosphonic acid (TiO$_2$_Im) respectively, were redispersed or dissolved in water. Although the kinetics of the formation of Ti-O-P bonds is known to be completed within minutes,[41] the reaction mixture was allowed to stir for 24 hours. To investigate the success of the modificiation of the titania nanoparticles, FTIR measurements of the dried, modified nanoparticles were carried out (Figure 4.9). Here, the free phosphonic acids were compared to the surface-bound ones. In the spectra, three regions are of great importance. The first is located between 700 to $800\,cm^{-1}$. These vibration bands stem from the P-OH bonds. Their disappearance in the spectra of the modified nanoparticles, are a logical step, because of the deprotonation of the phosphonic acids prior to formation of the Ti-O-P bonds. The second region of interest lies between 900 and $1050\,cm^{-1}$, containing different P-O vibrations. This region is not only shifted to higher wavenumbers, but also broadened significantly. This is due to the weakening of the P-O bonds, because of the formation of Ti-O-P bonds. The last area of concern, are the P=O vibrations between 1050 and $1150\,cm^{-1}$. These vibration bonds are greatly diminished, but can still be present, since the P-O vibrations may superpose their signal. Considering all these results at least a bidentate bonding of the phosphonic acids seems most likely. This finding was also reported in literature, where the bonding of phosphonic acids to transition metals was investigated (Chapter 1.2.3).[53,55,80]
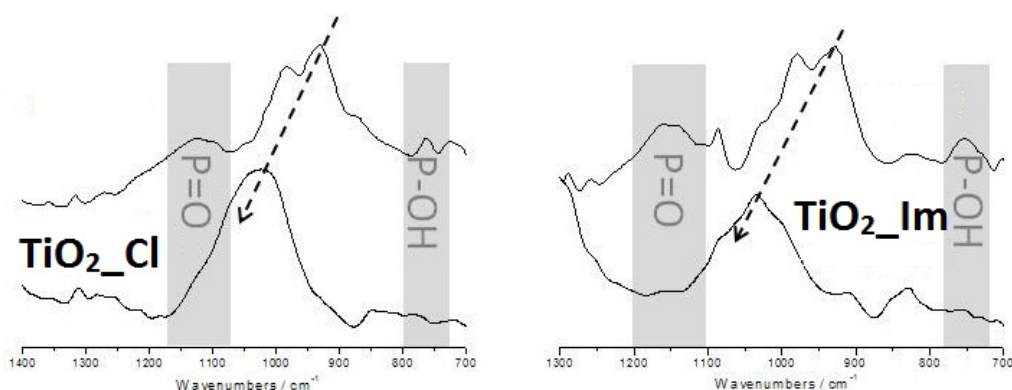

Figure 4.9: FTIR spectra of free (top) and coordinated to titania surface (bottom) of 3-chloropropylphosphonic acid (left) and N-imidazolylpropylphosphonic acid (right).

Another possibility to confirm the covalent binding of the phosphonic acid molecules to the surface of the titania nanoparticles is delivered through solid state CP MAS [13]P NMR (Figure 4.10). A broad peak around 30 ppm, can be observed. This broad peak was already reported in literature,[164] and is, on the one hand, attributed to the different binding modes of the phosphonic acid to the surface (Chapter 1.2.3) and on the other hand, deriving from field inhomogenities during the solid-state NMR measurement. This seem comprehensible, since the surface of nanosized objects offer a broad range of different geometry, surface energy and, therefore, chemical reactivity.[165] These results are in good agreement with the data obtained through FTIR measurements.
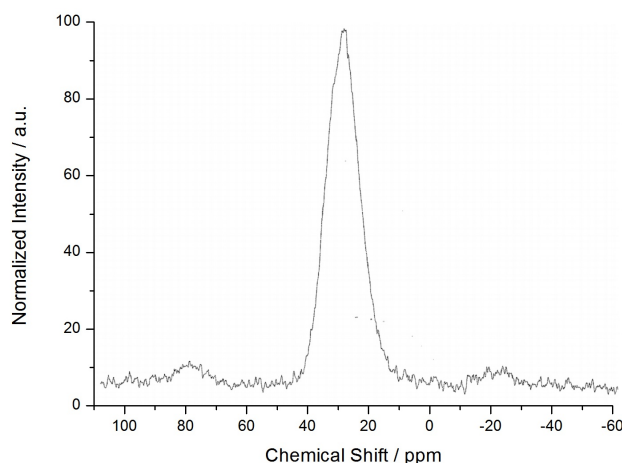
Figure 4.10: CP MAS [13]P NMR of 3-chloropropylphosphonic acid bond to the surface of titania nanoparticles.

In order to estimate the surface coverage of the titania nanoparticles TGA measurements were conducted (Figure 4.11). For both modified nanoparticle batches the weight loss from 25 to about 200 °C can be attributed to the evaporation of absorbed solvent molecules. Above 200 °C, with a climax around 300 to 350 °C, the degradation of the respective phosphonic acid ligand can be observed. Knowing the weight losses before and after 200 °C, the molecular masses of the ligand, the decomposed material and the substrate, it is possible to calculate the number of phosphorous ligands present on the surface of the titania nanoparticles after modification.[131] To calculate the number of ligands per nm^2 the number of particles contained in 1 g, the average diameter, obtained with XRD, has to be considered. By taking 4.0 nm as the diameter and a density of 4.24 g·m^{-3} for TiO_2, we can estimate to have 7.0x10^{18} nanoparticles in 1 g, each nanoparticle possessing a surface

area of about $50\,\text{nm}^2$. For further calculations the molecular mass of, for example, pure 3-chloropopylphosphonic acid, $158.52\,\text{g·mol}^{-1}$, and the molecular mass for the thermally degraded material, a chloride with an alkyl chain, $78.54\,\text{g·mol}^{-1}$, have to be considered. Thereby, after degradation the phosphor molecules remain on the surface, most likely as phosphates,[76] a coverage of 120 ligands per nanoparticle is calculated. This value is equivalent to about 2.4 ligands per nm^2.
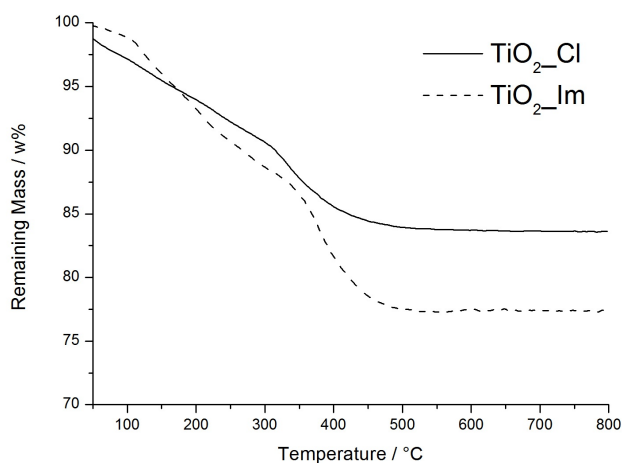
Figure 4.11: TGA measurements of modified titania nanoparticles.

If this value is calculated purely from a theoretical point of view, with $1.54\,\text{mmol}$ of ligands per $1\,\text{g}$ titania nanoparticles, 132 ligand molecules for each nanoparticle are calculated, which leads to 2.6 Ligands per nm^2. This obtained value for $1\,\text{nm}^2$ of 2.6 is slightly higher, but still in very good agreement with the empirical found one.

From the TGA data for the imidazole functionalised titania nanoparticles—the molecular mass of pure N-imidazolylpropylphosphonic acid, $190.14\,\text{g·mol}^{-1}$, and the molecular mass for the thermally degraded material, an imidazole with an alkyl chain, $79.86\,\text{g·mol}^{-1}$, have to be considered—a surface coverage of 133 ligands per nanoparticle. This leads to a value of 2.6 ligands per nm^2.

Grafting densities of around 4.2 to 4.8 ligands per nm^2 for octadecylphosphonic acid due to its high crystalline packing, by assuming a theoretical demand of $24\,\text{Å}$ per anchor group, were reported in literature.[72,166] Considering these results as values for a monolayer of ligands, for both modified nanoparticle batches about $60\,\%$ of a monolayer could be achieved.

Zirconia Nanoparticles

As for the titania nanoparticles, the surface modifications of the obtained zirconia nanoparticles were also carried out in water. Therefore 1 g of dried nanoparticles and 1 mmol, 0.159 g and 0.190 g, of 3-chloropropylphosphonic acid and N-imidazolylpropylphosphonic acid respectively were redispersed or dissolved in water. Here, less amounts as for the titania nanoparticles were used, since the zironica nanoparticles are slightly larger and therefore presenting a smaller total surface. Again, FTIR experiments show the expected vibrational bands (Figure 4.12). A broad peak between 900 and 1100 cm^{-1} is visible, pointing out the successful bonding of the phosphonic acid to the surface of the zirconia nanoparticles. The second region, around 750 cm^1, derives from Zr-O vibrations, thus the P-OH vibrations can not be observed.

Figure 4.12: FTIR spectra of ZrO$_2$ nanoparticles modified with of 3-chloropropylphosphonic acid (top) and N-imidazolylpropylphosphonic acid (bottom).

As for the funtionalised titania nanoparticles, the surface coverages are calculated through TGA measurements (Figure 4.13). Nearly the same values as for the modified titania nanoparticles are obtained, when an equivalent spherical radius of 4.5 nm, obtained through XRD, is taken into account. For the nanoparticles functionalised with 3-chloropopylphosphonic acid, a mass loss of 2.47 % between 25 and 200 °C, and 6.78 % between 200 and 800 °C leads to a surface coverage of 2.3 ligands per nm^2. When calculated only theoretically a value of 121 ligands for one nanoparticles, thus 2.6 ligands per per nm^2, is gained. This number is also in good agreement with the one, found through TGA experiments. When functionalised with N-imidazolylpropylphosphonic acid, a mass loss of 4.87 % between 25 and 200 °C,

and 7.38 % between 200 and 800 °C is measured. Therefore, a value of 1.9 ligands per per nm^2 is calculated. This is about 20 % lower than for the nanoparticles with chloro moieties.
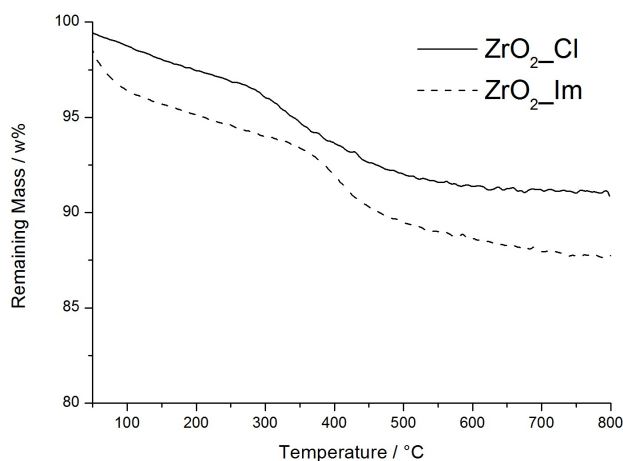
Figure 4.13: TGA measurements of modified zirconia nanoparticles.

This significant decrease can be explained, when looking at the TEM pictures obtained on the zirconia nanoparticles (Figure 4.2). The presence of a low curvature, can influence the surface coverage dramatically. For the imidazole functionalistation this could lead to a steric hindrance, whereas the alkyl chains of the 3-chloropopylphosphonic acid can align more easily.

Iron Oxide Nanoparticles

The dried magnetite nanoparticles were dispersed and sonicated in water and the respective phosphonic acid was added. For 50 mg of nanoparticles 0.25 mmol, equivalent to about 5 mmol per gram nanoparticle, of phoshphonic acid ligand was added. The reason for using such a small amount of nanoparticles is given by the poor redisperseability of magnetite in water. Once more, FTIR measurements were employed to determine the success of the surface modification reaction (Figure 4.14).

Similar to the tiania and zirconia systems, the broad peak between 900 and 1100 cm^1 can be observed, giving the information of a successful bonding of the ligand to the surface of the magnetite nanoparticles.
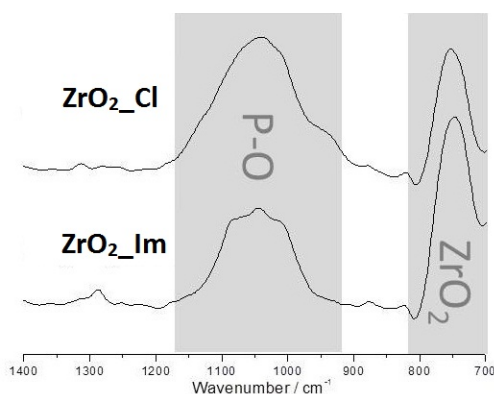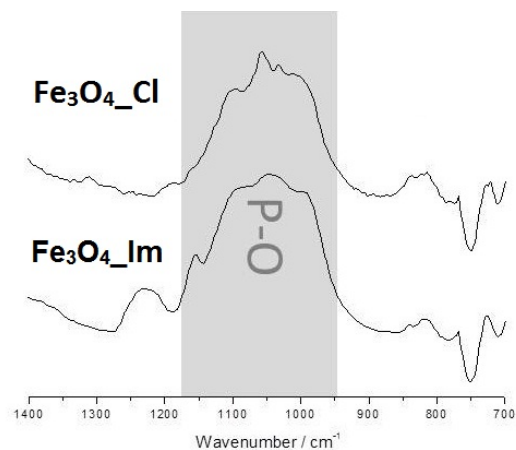
Figure 4.14: FTIR spectra of iron oxide nanoparticles modified with of 3-chloropropylphosphonic acid (top) and N-imidazolylpropylphosphonic acid (bottom).

As for the calculation of the number of ligands of the respective phosphonic acid, connected to the surface, TGA measurements cannot be employed in the case of magnetite nanoparticles (Figure 4.15). The reason for this is due to a competitive effect between a weight gain due to oxidation of the nanoparticles to Fe^{2+} and the weight loss due to the decomposition of the phosphonic acid ligands.[56] Nevertheless the total weight loss of about 13 to 15 % lies in the range as for the other metal oxide systems.
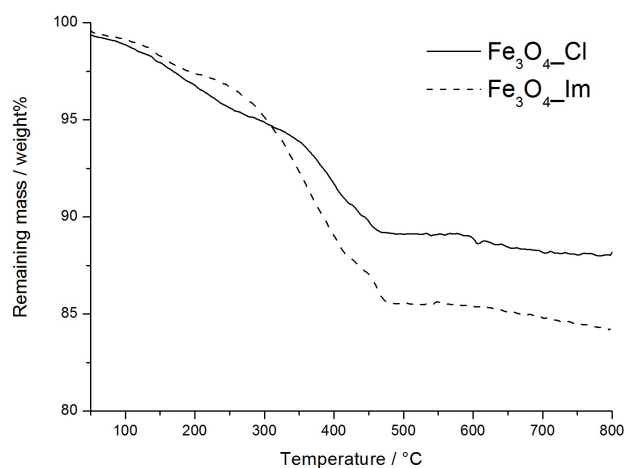
Figure 4.15: TGA measurements of modified magnetite nanoparticles.

4.1.3   Synthesis of Titania Nanoparticle Networks

The formation of the titania nanoparticle networks was obtained in the same way as for the silica nanoparticle networks (Chapter 3.3), through a nucleophilic substitution reaction between two differently modified nanoparticles batches. Therefore, the differently modified batches, as described in the previous chapter, were mixed and reacted for 24 hours. The crude product was gathered by centrifugation and washing extensively with ethanol and water, to eliminate unreacted, or unbound phosphonic acid molecules. To demonstrate the feasibility to construct transition metal oxide nanoparticle networks, titania nanoparticles were linked exemplarily.

To investigate and quantify the success of the linking reaction, a CP MAS ^{15}N NMR was measured (Figure 4.16). As for systems containing solely silica nanoparticles a broad peak around 145 ppm, with a shoulder at 135 ppm, can be observed. Through the described reference HMBC experiments (Figure 3.7) the two peaks can be distinguished. Thereby, the shoulder at 135 ppm corresponds to the unreacted imidazole moieties and the main peak at 140 ppm to imidazolium units. Thus, it could be shown, that, compared to silica based nanoparticle networks, again no complete reaction was achieved, but nevertheless imidazolium units did form.
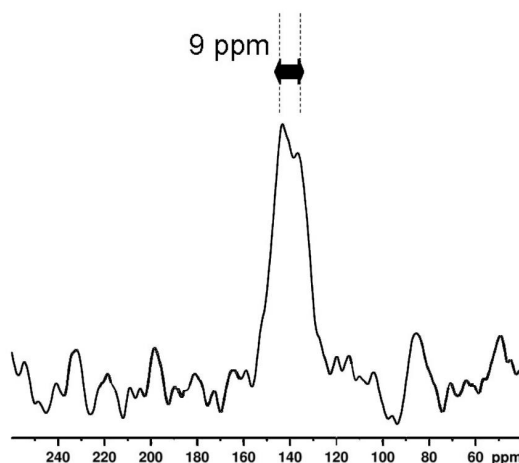
Figure 4.16: CP MAS ^{15}N NMR spectrum of titania nanoparticle networks.

A closer look on the characteristics of the obtained titania nanoparticle networks can be gained through nitrogen sorption experiments at 77 K (Figure 4.17). As reference the unmodified sol-gel derived nanoparticles were measured. The isotherm of the bridged sample can be described as a combination of a type Ib and IV isotherm with a H2 hysteresis loop, considering IUPAC classifications.[167]

The first pressure region of the isotherm, type Ib, is due to the high absorbed volume at very low relative pressure (P/P_0) values. This type of isotherm corresponds to the filling of micropores, pores with less than 2 nm diameter according to IUPAC notification. The kink of the isotherm is relatively smooth, indicating the presence of wide micropores. Further, the isotherm, starting from a relative pressure of around 0.2, here nitrogen is still adsorbed into the pores of the material, merges into a plateau, type IV isotherm. After the plateau, the desorption branch seems to be steeper than the adsorption loop, which is a hint for a porous network percolation effect.

The distribution of the pore diameter was calculated from the Barrett, Joyner and Halenda (BJH) equation from the desorption branch (Figure 4.17, insert). Here, the pore diameter is centered around 2 to 3 nm, corresponding to wide micropores or very small mesopores (pores with a diameter between 2 and 50 nm). The corresponding specific surface area of the titania nanoparticle networks was calculated with the Brunauer, Emmett and Teller (BET)[168] equation to be around 205 m^2·g^{-1}, which is comparable to the reported surface area of recently reported titania nanomaterials.[169,170] By plotting the experimental data of the isotherms against the statistical thickness of the layer, a t-plot can be constructed (Figure 4.17, right). Here, the contribution of the micropores of 81 m^2·g^{-1} to the total surface area is calculated. It has to be noted, that the profile of the t-plot is characteristic of a microporous material.

The obtained isotherms for the unmodified anatase nanoparticles measured as reference, show an almost non-porous material (Figure 4.17). This derives from the fact, that the nanoparticles, as well as the nanoparticle networks, are dried over P_2O_5 in vacuum prior to measuring. Therefore, aggregation of the particles occurs and the surface area of the untreated particles of about 0.5 m^2·g^{-1} is not surprising.

Further, a BET constant, C_{BET}, can be calculated on the mesopore monolayer deposition region of the isotherm (Equation 4.2), where E_L is a variable for the heat of condensation, which is equal for all the layers except the first and E_1 the heat of adsorption of the first layer:

$$C_{BET} \approx exp^{\frac{E_1 - E_L}{RT}} \tag{4.2}$$

This C_{BET} constant is proportional to the difference of the adsorption enthalpy for a monolayer and the upper layers. Therefore, this value is related to the affinity of the surface for the nitrogen molecules. Thus, the affinity can be related to the information about the polarity of the surface.[53] In our case the C_{BET} rises from 46 for unmodified anatase nanoparticles to about 81 for the nanoparticle networks.
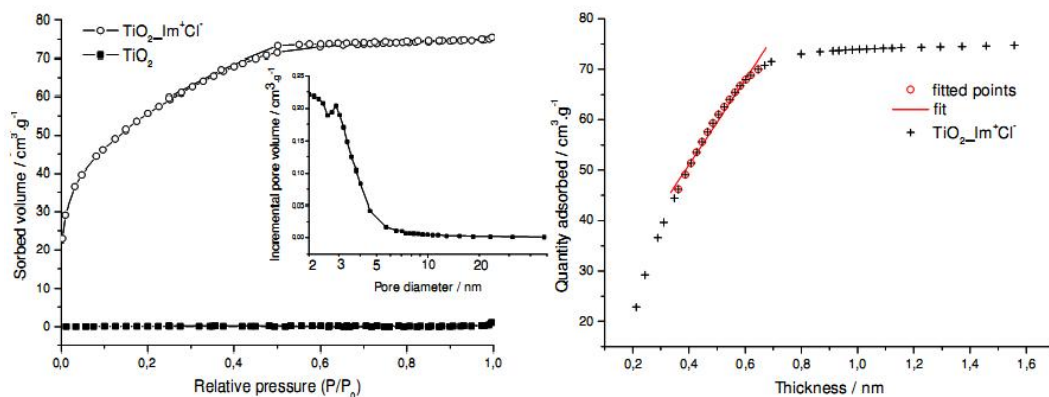
Figure 4.17: Nitrogen adsorption - desorption isotherm at $77\,\mathrm{K}$ (left) with a BJH pore distibution on the adsorption branch (insert) and Harkin and Jura t-plot of the titania nanoparticle networks (right).

This effect can be explained by the increase of the hydrophilicity through the modification of the nanoparticles with hydrophilic imidazolium units.

In an additional TEM micrograph of the final hybrid material (Figure 4.18), the titania nanoparticles can still be observed.
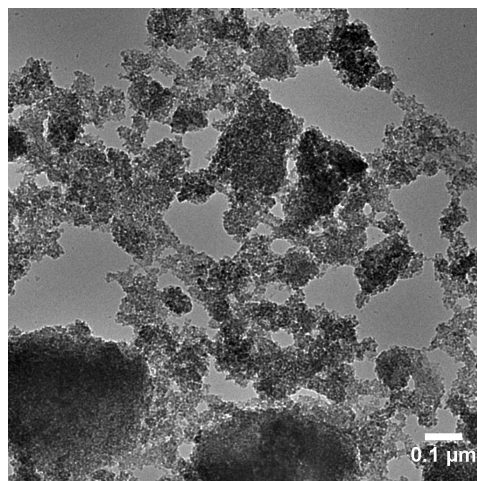
Figure 4.18: TEM image of titania nanoparticle networks.

Next to NMR and nitrogen sorption measurements, SAXS experiments were carried out to enhance the understanding of the structure of the nanoparticle networks (Figure 4.19). Here, a trimodality can be seen. Fitting the SAXS experimental curve with the Beaucage equation for multiple structural levels, as done for the nanoparticle networks based on silica (Chapter 3.3), leads to three different radii of

gyration. Thereby, the radius of gyration can directly be related to the diameter of spherical nanoobjects. This relationship is expressed through Equation 3.3.
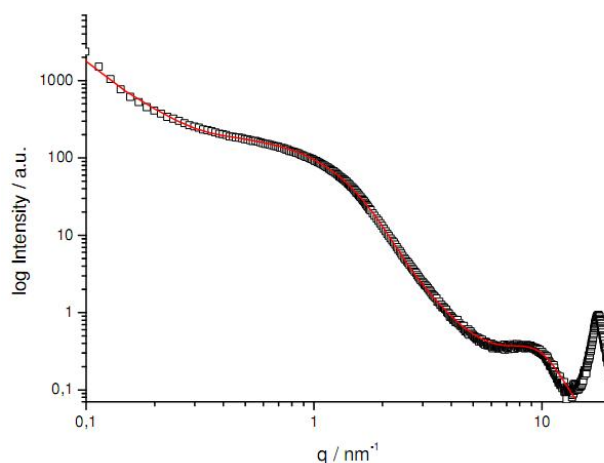
Figure 4.19: SAXS measurement with mathematical fitting of anatase nanoparticle networks.

Three diameters of the structural levels can be calculated: 0.5, 3.8 and 20 to 25 nm. The fist, 0.5 nm appears at a q value of about $9 \, \text{nm}^{-1}$ in the fitted plot. This value was interpreted as the molecular size of sol-gel prepared nanocrystalline anatase materials.[171] Additionally, the peak around $18 \, \text{nm}^{-1}$ derives from the (100) reflexion of titania anatase nanoparticles. Further, in the range from 0.1 to about $5 \, \text{nm}^{-1}$ the main feature can be spotted. Here, the kink at $q = 1.5 \, \text{nm}^{-1}$ corresponds to the size of the nanoparticles. The intensity of this peak points out the narrow size distribution with a mean diameter of 3.8 nm. This value is in good agreement with the diameter of 4.0 nm calculated through applying the Scherrer's equation on the reflexion of the anatase phase in the XRD pattern. The last diameter of 20 to 25 nm are obtained from refining the mathematical fit. Thereby, the intensity is very low, which makes it difficult to quantify the size very precisely. Nevertheless, it shows that an assembly of large domains of nanoparticles is present within the system. However, this lack of organization, compared to the silica based materials, could be useful, when thinking about hosting gas molecules in small pores, as supported by nitrogen sorption measurements. As a consequence from this measurement the pore diameter of about 2 nm, as seen through nitrogen sorption experiments, derives from an inter-particle spacing, smaller than the size of the nanoparticles.

To determine, if the porous character of the titania nanoparticle networks, examined through nitrogen sorption and SAXS measurements, affects the physicochemical

properties of the anatase nanoparticles, photocatalytic oxidation tests were carried out. It is known from literature that a high photocatalytic activity of titania is obtained for nanoparticles ranging from 1 to 10 nm in diameter.[170,172] Following literature known procedures,[51,170,173] the degradation of methylene blue (Figure 4.20) was chosen, since it is a fast and reproducible method and can easily be detected through Ultraviolet-visible (UV-vis) measurements.
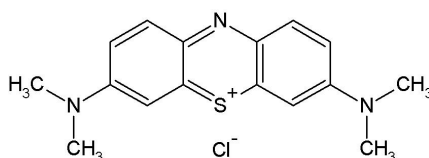
Figure 4.20: Chemical structure of methylene blue

For comparison, neat, unmodified titania nanoparticles were measured as reference. Dispersions of nanoparticles and nanoparticle networks were prepared by suspending 5 mg of the respective sample in 18 ml dionised water and 2 ml of a 200 μM aqueous methylene blue solution. It is known, that the adsorption of organic molecules on the surface of titania nanoparticles is dependent on the pH,[174] therefore, and also to ensure comparable results, the pH values were adjusted to a value of about 4. Illumination was carried out with two 9 W UVA black light lamps. The photocatalytic efficiencies of the networks and neat particles were calculated, based on the decrease of the maxima in the absorption spectra, measured over a time period of 320 min of illumination, of methylene blue dye solution with respect to the intensity corresponding to the λ_{max} of the dye, at 661 nm (Figure 4.21).
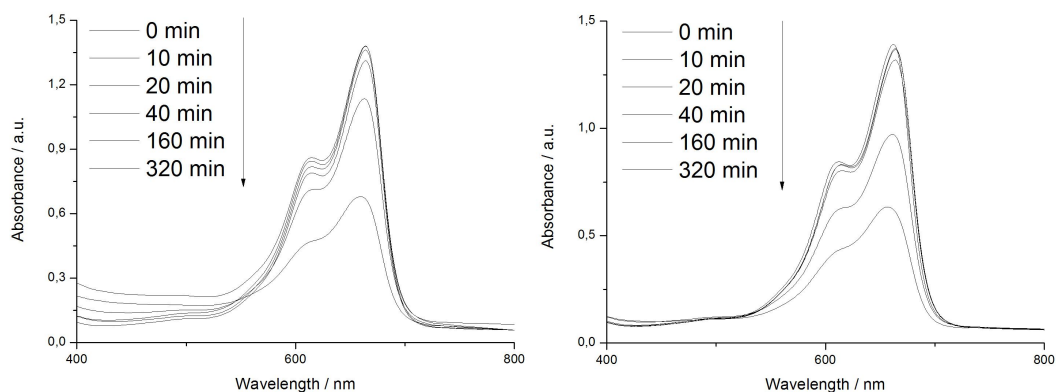
Figure 4.21: Photocatalytic degradation of methylene blue using pure anatase nanoparticles (left) and anatase nanoparticle networks (right).

Thereby, the photocatalytic degradation of methylene blue can be expressed through the following equation:

$$k[A] = -\frac{dA}{dt} \tag{4.3}$$

Here, A is the concentration of methylene blue, t is the time of exposure of UV-irradiance, thus $\frac{dA}{dt}$ is the rate of the change of the concentration of methylene blue, and k the first-order reaction rate constant, which is a direct indication of the rate of the photocatalytic activity. After integrating Equation 4.3 the following linear relation between the concentration and time is obtained:

$$kt = ln(\frac{A_0}{A}) \tag{4.4}$$

where A_0 is the initial concentration of methylene blue. Plotting $ln(\frac{A_0}{A})$ versus time, the rate constant k, (Figure 4.22), which is a direct indication of the rate of the photocatalytic activity, can be calculated.
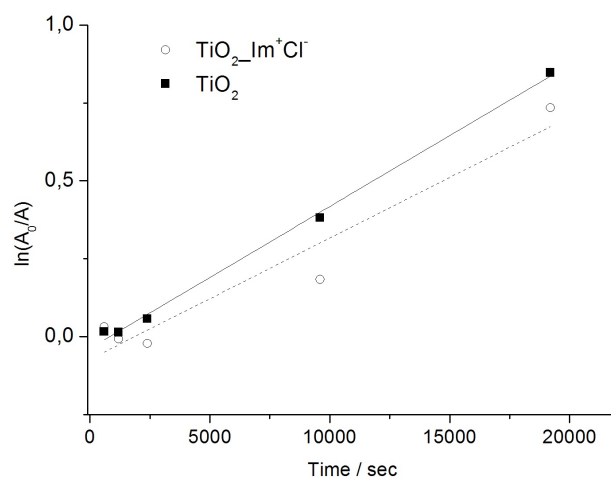
Figure 4.22: The evolution of the concentration over time of methylene blue under UV-irradiance of pure and linked titania nanoparticles.

The calculated k values for neat anatase nanoparticles $k = 4,5\text{x}10^{-5} \cdot \text{s}^{-1}$, and for the nanoparticle networks $k = 3,9\text{x}10^{-5} \cdot \text{s}^{-1}$ samples can be thus compared. Equivalent rate constants were reported in literature for Degussa P25 nanoparticles.[172] The maintained photocatalytic activity of the titania nanoparticle networks is an indication, that the hybrid material does not consists of agglomerated nanoparticles, even though some imidazole units did not react. Further, it also shows the accessibility of the titania nanoparticles surface to host molecules, even at the presence of

a functionalised surface.

4.1.4   Conclusion

In this chapter the methodology to create ionic silica nanoparticle networks was extended to other metal oxide nanoparticles, titania, zirconia and iron oxide, with investigating titania nanoparticle networks closer. To this purpose, phosphonic acid ligands, containing either chloride or imidazole end groups, had to be synthesized in order to modify the particles. The formation of the networks occurs, as for silica, by nucleophilic substitution reactions between the functionalities introduced on the nanoparticles surfaces. The success of, on the one hand functionalisation of the particles, and the networking on the other hand, was investigated with FTIR and NMR spectroscopy. As for the systems based on silica nanoparticles the imidazole groups did not react entirely. The porous character of the network was investigated through nitrogen sorption measurements. Here, a pore diameter around 2 nm was detected, deriving from an inter-particle spacing. Further, SAXS investigations suggest an arrangement of the material with three structural levels, one being around 20 nm indicating assemblies of large domains. Last, it could be shown, that the photocatalytic activity is still present within the system, through the degradation of methylene blue.

4.2 Variation of the Linking Unit

After the variation of the metal oxide, as shown in the previous chapter, the influence of the chemical structure, rigidity and length of linking unit between the silica nanoparticles was investigated. Therefore, silica nanoparticle networks containing two imidazolium entities in the bridging units, were compared to networks with one imidazolium unit, as presented in the last chapter. These systems with two imidazolium units were synthesised through reaction of molecular compounds bearing two chloro funtionalities (Figure 4.23), with silica nanoparticles modified with *N*-(trimethoxysilylpropyl)imidazole (Chapter 3.2).
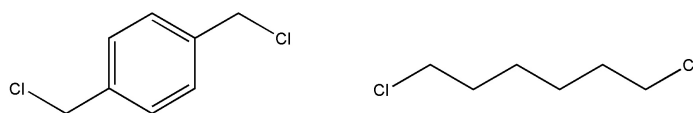
Figure 4.23: Chemical structure of 1,4-bis(chloromethyl)benzene and 1,6-dichlorohexane, used as linking units.

Using this path of synthesis, silica nanoparticle networks containing two imidazolium units are synthesised (Figure 4.24). Within this chapter the silica nanoparticles bridged with 1,4-bis(chloromethyl)benzene should be referred as xylene, 1,6-dichlorohexane as hexyl and the systems containing one imidazolium unit as imidazolium.
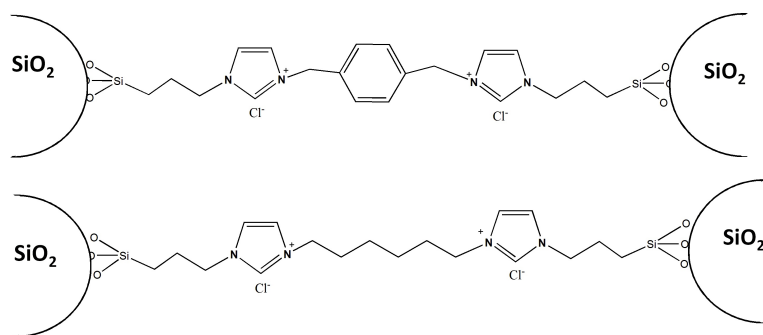
Figure 4.24: Silica nanoparticles bridged either by xylene or hexyl entities.

Through SAXS experiments a qualitative description of the efficiency of the respective synthesis method to link the nanoparticles can be estimated (Figure 4.25). As shown in Chapter 3.2, with SAXS investigations of hybrid materials, concerning ionic silica nanoparticle networks containing one imidazolium unit, a short-range ordering of the nanoparticles can be seen. For the measurements with systems containing two imidazolium units, a different model for the calculations was used. In

the spectrum the pronounced peak in the range of about $5\,\mathrm{nm}^{-1}$, is attributed to the distance between the silica nanoparticles. In the case of hexyl and xylene as linking units, a shift to lower q values, which correspond to longer distance in real space, can be observed.
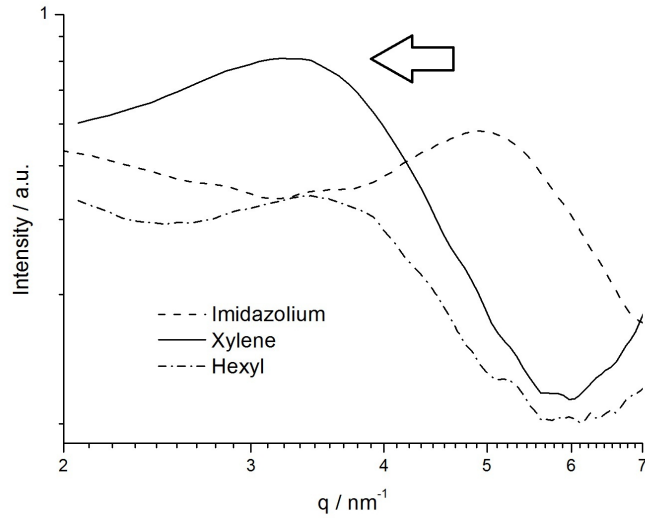
Figure 4.25: SAXS measurements of the materials containing one imidazolium unit, two imidazolium units or hexyl as linking unit.

The maxima of the scattering peaks, characteristic for the short-range ordering, are reported in Table 4.1, can be related to the length of the ligand introduced to connect the silica nanoparticles. This confirms the correct hypothesis to assign the peaks around 5 nm-1 to a short-range ordering of the nanoparticles within the system.

Table 4.1: Numerical data obtained from SAXS measurements.

Linker	Peak Maximum / nm^{-1}	Length / nm	k_1	k_2
Imidazolium	5.01	1.25	2.2	7.4
Hexyl	3.54	1.78	—	7.5
Xylene	3.33	1.89	2.3	7.3

Furthermore, two packing factors can be calculated from the mathematical approach, k_1 and k_2. These two factors describe the amount of the short-range order of

the ligands and the nanoparticles. Thereby, k_2 is attributed to the strong stacking of the ligands with high values, around 7.3 and k_1 highlights the short-range ordering of the nanoparticles. The numerical values obtained for the packing factors of monoimidazolium based networks, support the assumption of a short-range ordering of the silica nanoparticle (Table 4.1). Extending the investigation to diimidazolium linking units, it turns out, that with increasing length of the bridging units, the flexibility of the ligand plays an important role. For ligands with a high flexibility, having a long alkyl chain between two imidazolium groups, like hexyl, the ordering of the particles within the network becomes weaker. This effect can be explained, by the fact, that the hexyl chain can interact with imidazolium moieties covalently bonded on the same nanoparticle (Figure 4.26).
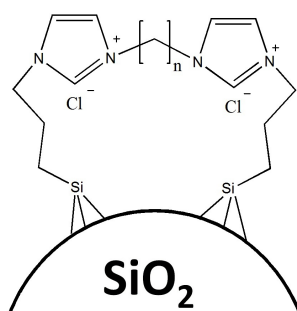
Figure 4.26: Flexible Linkers can lead to possible "backbiting" of the chains on the same particle.

By using a xylene unit instead of the alkane part between two imidazoliums the rigidity is enhanced. Furthermore, the quality and the extension of the network are improved.

It could be shown by Czakler,[175,176] that these hybrid materials possess photoluminescence properties due to a self-organization of the aromatic imidazolium rings by $\pi-\pi$ stacking (Figure 4.27). Comparing the differently connected nanoparticles—for the monoimidazolium an excitation wavelength of 337 nm was used, whereas hexyl and xylene samples were excited at 350 nm respectively—a relationship to the SAXS measurements can be drawn. Through the usage of flexible alkyl chains, very weak or none fluorescence can be seen. This effect is due to the insufficient self-organization of the material, as seen from the measured packing factors, k_1 (Table 4.1), because of the flexibility of the ligand, which hinders $\pi-\pi$ stacking phenomenons. As for the xylene as ligand, a shift of the emission maximum from 395 nm, for the systems containing one imidazolium unit, to 415 nm, and therefore towards lower energies, can be observed. Since 415 nm is already in the visible spectrum, a blue emission of the

measured powder can be seen with the naked eye, when excited at 350 nm. This shift is accompanied by a decrease in the quantum yield, from 0.26 for systems with one imidazolium to about 0.13 for xylene bridged silia nanoparticle systems, and nearly none for hexyl. This decrease could be caused by aggregation quenching through the introduction of additional aromatic moieties, which enhance $\pi-\pi$ stacking effects.[177]
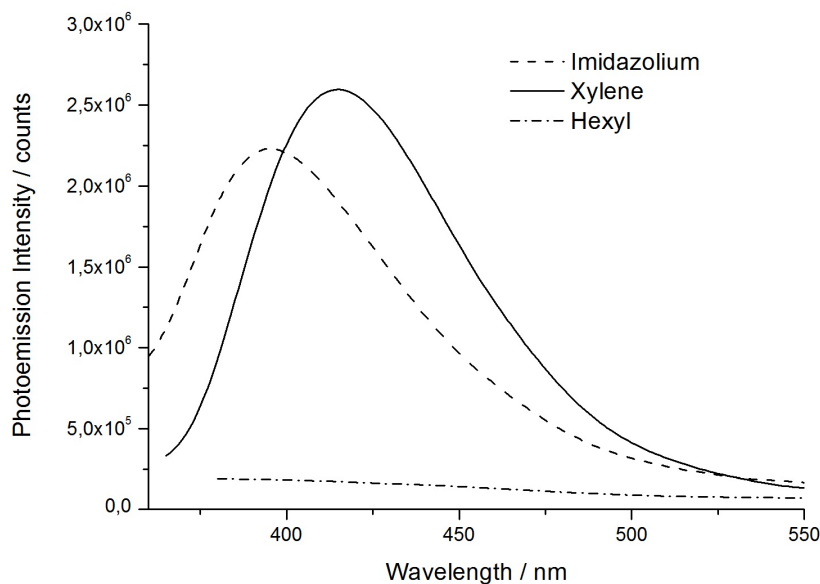
Figure 4.27: Emission spectra of various hybrid materials.

4.2.1 Conclusion

In this chapter the linking unit between silica nanoparticles was altered, using dichloro compound to undergo nucleophilic substitution reaction with imidazole functionalised nanoparticles. Through SAXS and photoluminescent investigations, it could be shown, that more rigid ligands lead to networks with higher packing factors. Through the usage of long flexible alkyl chains, networks with no short-range order are obtained. This is an effect of possible "backbiting" reactions of the ligand on the same silica nanoparticle.

4.3   Variation of the Anion

As the third, and last alteration possibility, the anions of network of silica nanoparticles containing either one or two, with xylene entities in between (see Chapter 4.2), imidazolium units, were exchanged. The exchange of the anion follows a metathesis reaction, as it is used to exchange the anion of ionic liquids. This was achieved by addition of a salt of the to be introduced anion, to the hybrid material ($SiO_2\_Im^+Cl^-$). The metathesis reaction can be expressed, for materials with one imidazolium unit, as follows:

$$SiO_2\_Im^+Cl^- + Y^+X^- \longrightarrow SiO_2\_Im^+X^- + Y^+Cl^- \quad\quad (4.5)$$
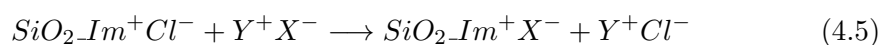
Thereby, the nanoparticle networks, which were obtained after drying as a powder ($SiO_2\_Im^+Cl^-$), where dispersed in acetone and the respective salt (Y^+X^-), either NaBF$_4$, KPF$_6$ or LiT$_{f2}$N, a bis(trifluoromethylsulfonyl)imide anion, was added in a weight ratio of 1 to 1, 0.25 g each. It is obvious, that the used salts were introduced in an excess, with regard to the amount of anions within the system. The reason for choosing acetone is, that the chloride salts, e.g. NaCl, are insoluble in acetone. Therefore, the metathesis reaction is driven by the precipitation of these salts (Y^+Cl^-).[178] After 24 hours of stirring the silica nanoparticle networks with the exchanged anions ($SiO_2\_Im^+X^-$) were gathered through centrifugation and washing extensively with water, ethanol and acetone. The collected washing fractions were evaporated and the gathered, thus resulting corresponding chlorine salts (Y^+Cl^-) investigated.

The success of the metathesis reactions were evaluated by two methods. First, the gathered salts (Y^+Cl^-) were investigated using XRD. This pathway offers an indirect proof for the reaction. Second, NMR of the obtained materials ($SiO_2\_Im^+X^-$) delivers a direct proof for the presence of the newly introduced anions within the systems.

In the XRD pattern of the washing fractions, obtained after treatment of the nanoparticle networks containing one imidazolium unit with NaBF$_4$ or KPF$_6$, the signals for the corresponding chlorine phases, NaCl and KCl, can be observed (Figure 4.28). However, as NaBF$_4$ and KPF$_6$ were introduced in a large excess, the predominant phases can be attributed to these. In the case for LiT$_{f2}$N only an amorphous pattern (not included) was obtained. This effect can be explained by the fact, that LiCl is a very hygroscopic compound, and therefore a non-negligible water uptake occurred during the XRD measurement, also observed as a liquifida-

tion of the sample. Additionally, XRD measurement of the systems with the newly introduced anions were measured ($SiO_2\_Im^+X^-$), showing only amorphous pattern. This indicates, with the results obtained from Figure 4.28 that not only an adsorption of the different salt occurred, but an exchange. Furthermore, systems with two imidazolium units were treated the same way. Thereby, the same results were obtained, when measuring XRD.
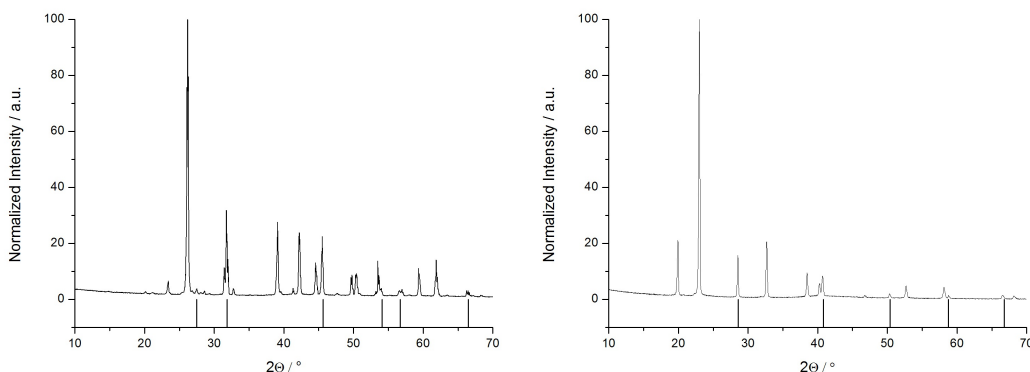
Figure 4.28: XRD patterns of the used and corresponding salts: $NaBF_4$ and $NaCl$ (left, bars: JCPDS # 74-0199 for NaCl) and KPF_6 and KCl (right, bars: JCPDS # 01-0790 for KCl).

As said in the beginning, solid-state NMR studies could deliver a direct proof of the presence of the anions. Figure 4.29 shows the respective NMR measurements for each anion. For each new anion the respective nucleus was measured. For BF_4^- a ^{11}B NMR detected the presence of boron atoms, with a chemical shift of -0.5 ppm typical for BF_4^- species. In the case of phosphorous, PF_6^-, the presence was evidenced by a ^{31}P NMR. Here, the multiplicity of the heptet signal originates from the ^{31}P-^{19}F coupling. As for the bis(trifluoromethylsulfonyl)imide anion a ^{15}N NMR was employed. As investigated in Chapter 4.1 the peak at higher field, around 140 ppm, can be attributed to imidazole and imidazolium units, whereas the peak at lower field, 210 ppm, comes from unreacted imidazole and the nitrogen atom of the imide anion.

As for the systems containing two anions, the same signals for the respective anion were obtained, showing the presence of the desired anions, BF_4^-, PF_6^- and $T_{f2}N^-$, and therefore presenting a direct proof for the exchange of the anions in the systems.
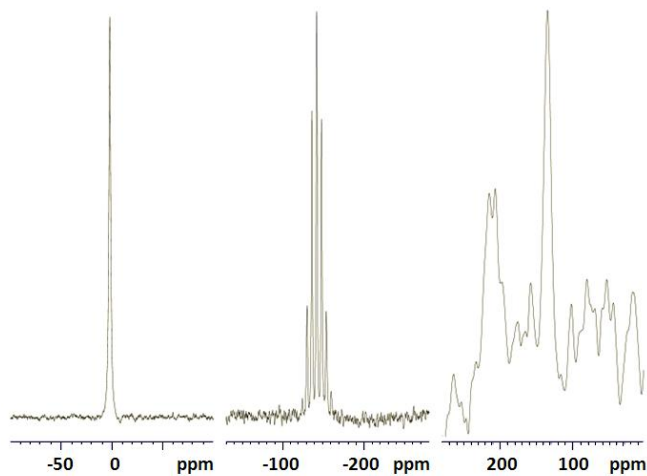
Figure 4.29: CP MAS NMR measurements of materials containing one imidazolium unit with an ^{11}B NMR (left), a ^{31}P NMR (middle) and a ^{15}N NMR (right) spectrum.

In addition, scanning electron microscopy (SEM) coupled with energy dispersive X-ray spectroscopy (EDX) measurements were carried out. As for the nanoparticle networks containing two imidazolium units the SEM image shows a sharp edged material with a smooth surface (Figure 4.30). This morphology most probably derives from the drying step, and is not be investigated further, since it was recorded to gain a reference which could be compared to the samples obtained after the anion exchange. The EDX spectra shows the expected peaks for the silica nanoparticles (Si and O), ligands (C, a nitrogen signal should be around 0.3 keV, but is superposed by the neighbouring signals) and, around 2.8 keV, chloride.
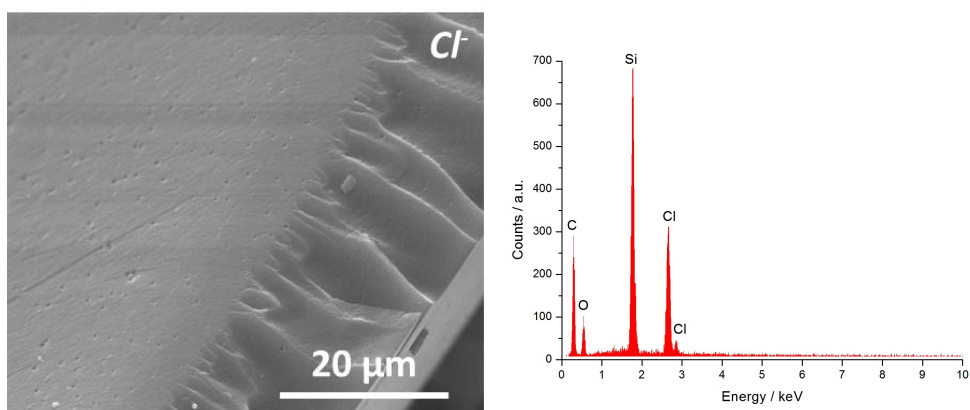
Figure 4.30: SEM and EDX measurements of silica nanoparticle networks containing two imidazolium units with chloride as anion.

After the anion metathesis reaction, for systems with two imidazolium units, the SEM images (Figure 4.31) do not show any significant changes. It can be concluded that the macroscopic morphology of the samples, sharp edges and smooth surface, is not altered by the chemical nature and size of the new introduced anions.
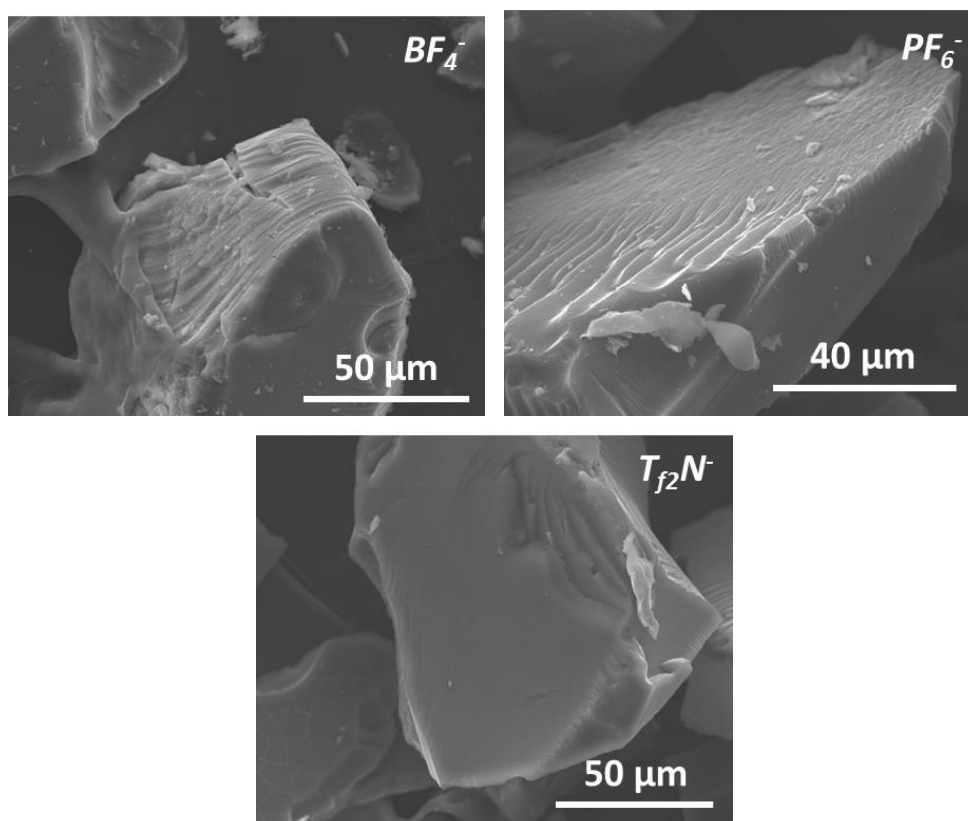
Figure 4.31: SEM measurement of silica nanoparticle networks containing two imidazolium units with BF_4^- (upper left), PF_6^- (upper right) and $LiT_{f2}N$ (bottom) as anion.

By looking at the EDX spectra (Figure 4.32) the typical signals for the introduced anions, BF_4^-, PF_6^- and $T_{f2}N^-$ can be observed. For the first two samples, a fluorine signal at $0.6\,keV$ is clearly visible. Only for the last sample, here the imide anion was introduced, the fluorine, as well as the sulphur signal at $2.3\,keV$, disappear in the noise of the spectrum. Further, a phosphor peak at $2\,keV$ for the second sample, PF_6^-, appears. However, the B signature for the material containing the BF_4^- anion, is superposed by the carbon peak at $0.2\,keV$. Interestingly, the signal at $2.8\,keV$ for chlorine is still present in all samples. Although the EDX data can not be quantified, because this technique is based on the electron density of the elements,

it is obvious that, compared to the initial chloride concentration (Figure 4.30), a certain amount of anions were not exchanged in the systems. Further, it appears, that with increasing size of the anion, a decrease in the metathesis yield is obtained.
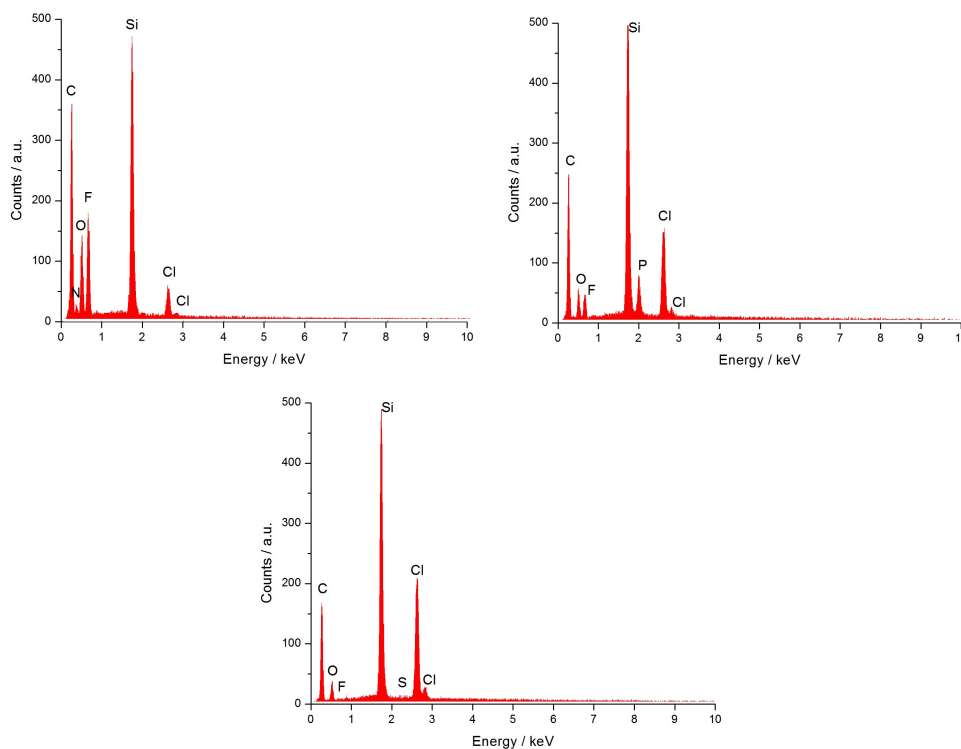
Figure 4.32: EDX measurements of silica nanoparticle networks containing two imidazolium units with BF_4^- (upper left), PF_6^- (upper right) and $T_{f2}N^-$ (bottom) as anion.

For a quantitative evaluation, elemental analysis of the samples containing one imidazolium and different anions, were measured (Table 4.2). Here, the assumption of incomplete exchange ratios made after EDX experiments, is confirmed. As reference, the initial starting compound with chlorine as anion is taken. Afterwards, the yield of the metathesis reaction can be calculated by comparing the percentage of remaining chlorine in the material, with the weight percentage of chlorine of the reference.

Thereby, the indicated incertitudes on the metathesis yields are due to the evolution of the molar weights of the anions. Nevertheless an almost linear relationship between the yields, ranging from 85 % for BF_4^- to 25 % for $T_{f2}N^-$, and the molecular weight of the anion can be calculated.

Table 4.2: Elemental analyses, in weight percent, for nanoparticle networks with one imidazolium unit.

	Cl content / %	Anion / g·mol^{-1}	Yield / %
Cl$^-$	6.50	35	
BF$_4^-$	0.98	87	85 ± 3
PF$_6^-$	2.61	145	60 ± 6
T$_{f2}N^-$	5.20	280	25 ± 10

Furthermore a relationship between the excesses of the introduced salts and the metathesis yields can be drawn. Therefore, the amount of chloride inside the starting material has be calculated. By using 0.25 g of the material, 16 mg (0.46 mmol) of chloride anions are available for the exchange reaction. Since 0.25 g of the salts were used, the excesses of the salts can be calculated, 1.82 mmol of NaBF$_4$, 0.9 mmol of KPF$_6$ and 0.41 mmol of LiT$_{f2}N$. By dividing these values through the metathesis yields for the respective anions, almost the same results are obtained for the three different salts (Table 4.3). This leads to the conclusion, that the metathesis reaction is mainly driven by the used excess and not by the size of the newly introduced anions.

Table 4.3: Relationship between used excesses of the salts and metathesis yields.

	Yield / %	Excess / mmol	Ratio Excess/Yield / %
BF$_4^-$	85	1.82	0.021
PF$_6^-$	60	0.90	0.015
T$_{f2}N^-$	25	0.41	0.016

To get more information, whether the network structure changed after the anion metathesis reaction, SAXS measurements were carried out. In Figure 4.33 the results with silica nanoparticle networks with one imidazolium unit are displayed. Again, for the numerical description of the data, an approach by Beaucage as in the previous chapters, was used. Through that, structures with multiple orders of hierarchy can be investigated. As in Chapter 3.3, two organisations in the networked material can be identified. First, the arrangement of the nanoparticles (d_1) at lower q values, and second a short range order of the imidazolium rings at around 5 nm^{-1}(d_2). Comparing the hybrid materials obtained after anion exchange, the basic network structure appears to be unchanged. In the case of PF$_6^-$ and T$_{f2}N^-$, an additional peak at 9 nm^{-1} indicates an arrangement of the imidazolium units as a one-dimensional chain. A third diffraction peak at higher q values would be superposed by the silica peak at around 15 nm^{-1}. This arrangement of the aromatic

units may be a results of the incomplete metathesis reaction as shown by elemental analysis.
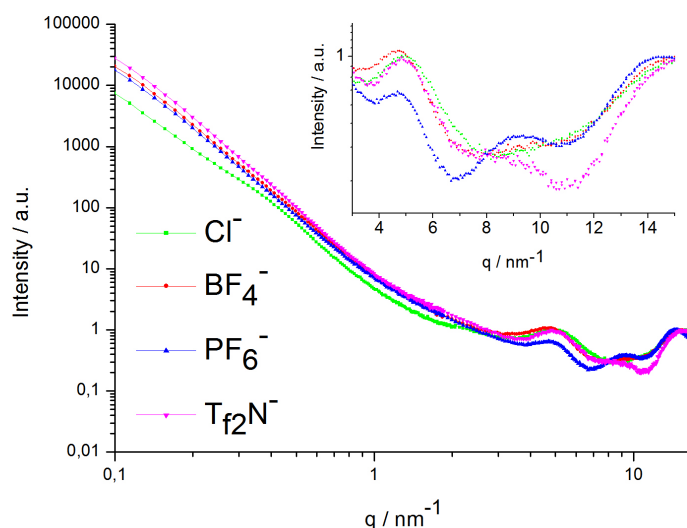
Figure 4.33: SAXS measurements of the materials containing one imidazolium unit, with the exchanged anions and enlargement at large q values (insert).

Further, the packing factor (k_2), thus the amount of short-range ordering within the system, can be calculated. Here, the values range from 8.2 for the starting compound, to about 8.9 for the hybrid material containing $T_{f2}N^-$ as anion (Table 4.4). These findings correlate with the evaluation of the radii of gyration (Equation 3.3), which increase from 0.63 nm to 0.82 nm when the imide anion is introduced. These values could derive from the effect, that the imidazolium rings are slightly less packed when the counter anion has less interaction with the aromatic entity, rather than a real difference in their size. However, their correlation distances (d_2) are identical. The higher value of r_g for PF_6^- and $T_{f2}N^-$ is due to the smaller electronegativity of these two anions in comparison to the initial, chlorine, samples and BF_4^-. The electron densities of PF_6^- and $T_{f2}N^-$ could appear in SAXS not as clearly separated but partly overlapping objects, which leads to a higher value for the radius of gyration.

Table 4.4: Packing factor (k_2), radius of gyration of units (r_g) and correlation distance (d_2) of systems with one imidazolium unit, containing different anions.

	k_2	r_g / nm	d_2
Cl^-	8.2	0.63	1.1
BF_4^-	8.1	0.66	1.1
PF_6^-	8.3	0.88	1.1
$T_{f2}N^-$	8.9	0.82	1.1

For the nanoparticle networks containing two imidazolium units a similar picture is obtained (Figure 4.34). Here the scattering peak at a q value of around $3.3\,\text{nm}^{-1}$, correlating to a real space of about $1.9\,\text{nm}$, stays unchanged during the exchange of the anion.
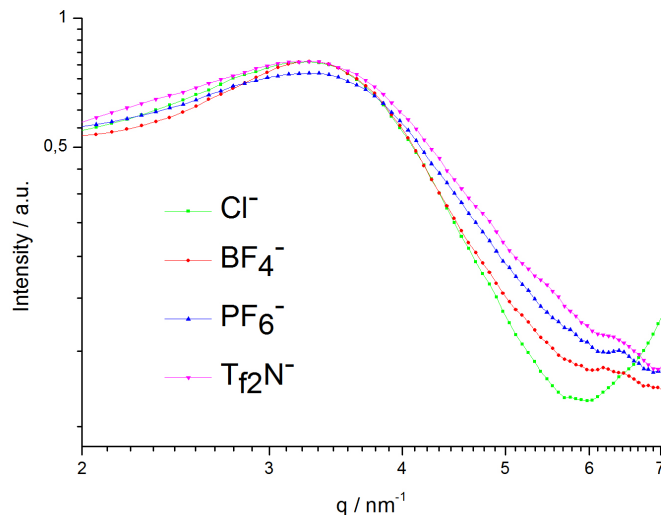
Figure 4.34: SAXS measurements of the materials containing two imidazolium unit.

As discussed in Chapter 1.3, the hydrophilic or hydrophobic character of ionic imidazolium compounds can be tuned by the choice of the anion.
Considering 1-butyl-3-methylimidazolium as an example, it can be hydrophilic when the counter part is a chloride and hydrophobic with a PF_6 or $T_{f2}N$ as the anion.
Considering the hybrid material an easy to perform test, to see if the hydrophilicity of the silica nanoparticle networks containing chloride changes when the anion is replaced, even partially, by BF_4^-, PF_6^- or $T_{f2}N^-$, is done by dispersing the material in water (Figure 4.35). The images show all four different samples for the networks with one imidazolium unit. If PF_6^- or $T_{f2}N^-$ is present, the materials seem to have

a hydrophobic character, since the material is not very well dispersed in the solvent and most of the powder is floating on the surface, contrary to the samples with Cl^- and BF_4^-.

Figure 4.35: Digital image of silica nanoparticle networks with one imidazolium unit with (from left to right) Cl^-, BF_4^-, PF_6^- and $T_{f2}N^-$ as anion.

4.3.1 Conclusion

In this chapter the anion of the system was exchanged through an anion metathesis reaction. This reaction was performed on silica nanoparticle networks containing either one or two imidazolium units and chloride as the anion. For the exchange reaction different salts, $NaBF_4$, KPF_6 and $LiT_{f2}N$, were used. The presence of the newly introduced anions, BF_4^-, PF_6^- and $T_{f2}N^-$, was evidenced by XRD, solid-state NMR, EDX and elemental analysis. Metathesis yields could be calculated, ranging from 25 % to 85 %. Thereby, the dependencies of the yields could be explained by the used molar ratios, and thereby the excesses, in which the salts where introduced. Further, the structures of the networks were investigated through SAXS measurements. For the samples, with only a partial exchange of the anion, an arrangement of the imidazolium units, as seen by the evolution of a signal, could be observed. The anion metathesis on those compounds, even if not fully completed, allows tailoring the hydrophily / hydrophoby of the hybrid material.

Chapter 5

Silica/Silver Nanoparticle Systems

In the previous chapters, systems containing only one kind of metal oxide nanoparticles were investigated. In this chapter the formation of networks containing metal oxide and metal nanoparticles, for example silica and silver, at the same time, were examined.

5.1 Synthesis of Imidazole/Thiol Systems

The starting point for the synthesis of these mixed nanoparticle systems, is the preparation of imidazole functionalised silica nanoparticles (Chapter 3.2) by using N-(trimethoxysilylpropyl)imidazole. As described in Chapter 4.1 the imidazole moiety, at pH values lower than 7, is present in the protonated imidazolium form. Recently, it was shown by several groups,[179–181] that the imidazole molecule is able to deprotonate weak acids, such as carboyxlic acids to form the corresponding carboxylate salts. Thereby, the effect of the resulting hydrogen bonds can be very significant, leading to the formation of supramolecular layers based on the interaction between imidazole and carboxylic acids.

This effect can also be utilised to create nanoparticle networks by adding 3-mercaptopropionic acid to a solution of imidazole modified silica nanoparticles. Through addition of the carboxylic acid to the imidazole functionalised nanoparticles suspension, the acidic protons of the carboxylic acid group will be transferred to the nitrogen of the imidazole unit. Afterwards, the introduced thiol groups can graft onto the surface of various metal nanoparticle (Chapter 1.2.3), in this case silver, thus creating networks with alternating silica and silver nanoparticles. First, the reaction is

tested in the liquid state, without nanoparticles by mixing *N*-methylimidazole and 3-mercaptopropionic acid in a molar ratio of 1 to 1 without any solvent (Figure 5.1).
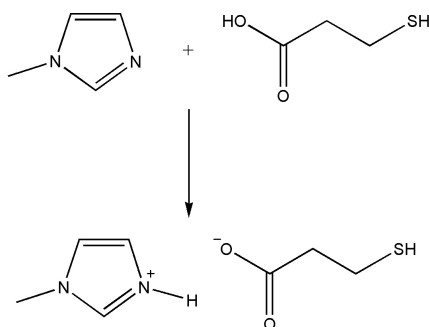
Figure 5.1: Reaction of *N*-methylimidazole and 3-mercaptopropionic acid.

Through ^{1}H NMR spectroscopy this reaction can be followed. In the NMR spectra (Figure 5.2) the formation of the imidazolium unit is characterised by a 1 ppm shift, of the aromatic protons between 6 and 7 ppm, towards lower field, as well as the peak for the methyl groups at 3 ppm. Further, the disappearance of the peak around 11.5 ppm for *N*-methylimidazolium mercaptopropionate, deriving from the carboxylic acid proton of the precursor, can be observed. Instead, a broad peak in the same region can be seen, characteristic for a labile, exchangeable proton. It has to be noted, that the reaction is accompanied by an increase of the viscosity of the solution upon addition of 3-mercaptopropionic acid to *N*-methylimidazole, with additional generation of heat.
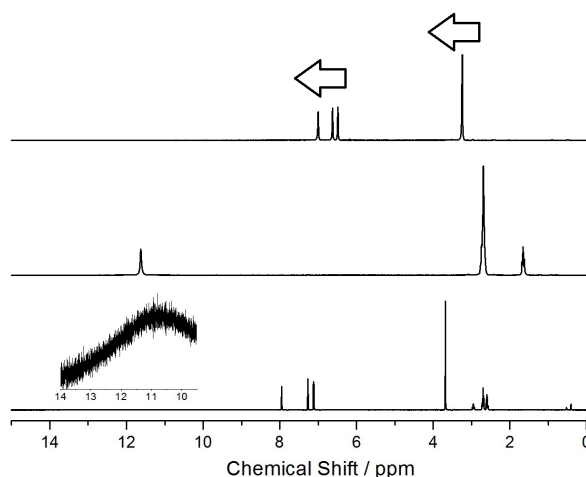
Figure 5.2: ^{1}H NMR spectra of (from top to bottom) *N*-methylimidazole, 3-mercaptopropionic acid and *N*-methylimidazolium mercaptopropionate.

5.2   Synthesis of Silica/Silver Nanoparticle Networks

After this investigations, the reaction is adapted to imidazole functionalised silica nanoparticles. Through addition of an equimolar amount, $5\,mmol$ $(83\,mmol \cdot l^{-1})$, of 3-mercaptopropionic acid to the suspension, thiol groups are now present as end groups. The reaction can be followed through DLS measurements (Figure 5.3). Thereby, the results deliver the distributions of the hydrodynamic radii of the silica nanoparticles, the particles functionalised with N-(trimethoxysilylpropyl)imidazole, and finally after reaction with 3-mercaptopropionic acid. At each step of the nanoparticle functionalisation, an increase of the nanoparticles radii can be observed, growing from initial 8 nm to 11 nm and finally 15 nm for the thiol end capped nanoparticles. For the thiol functionalised nanoparticles it has to be noted, that a broader size distribution can be observed, possibly deriving from interactions with the hydrogen atoms of the thiol and the hydrogen atoms of the solvent molecules.
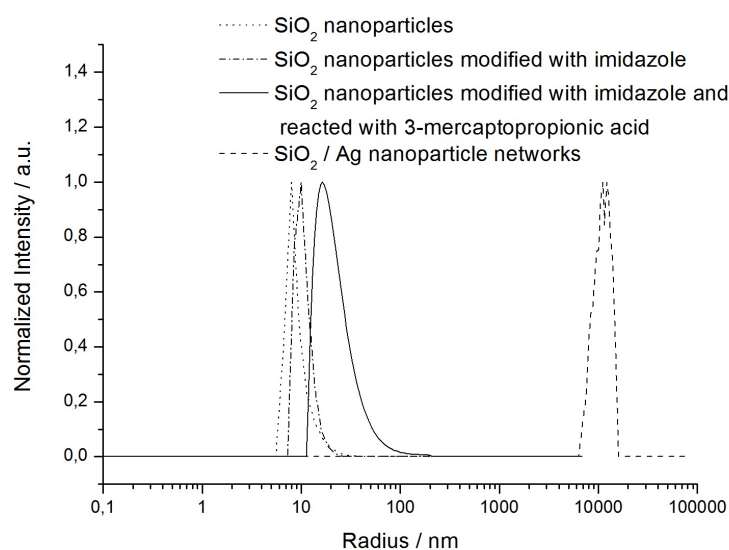
Figure 5.3: DLS measurements of the different stages for the formation of silica/silver nanoparticle networks.

Afterwards, to create the final silica/silver nanoparticle networks, $AgNO_3$ is added prior to reduction with sodium borohydride (Figure 5.4). A black powder was obtained after centrifugation and drying. The thus resulting silver nanoparticles are, as well as the silver cation present before reduction, bonded to the thiol groups pending on the surface of the silica nanoparticles. Through DLS, although this method is not suitable to characterise non-spherical nanoparticle networks, an increase of the measured radius can be observed, indicating a formation of macroscopic networks

(Figure 5.3, dashed line). Furthermore, no more individual nanoparticles at lower radii values can be seen.
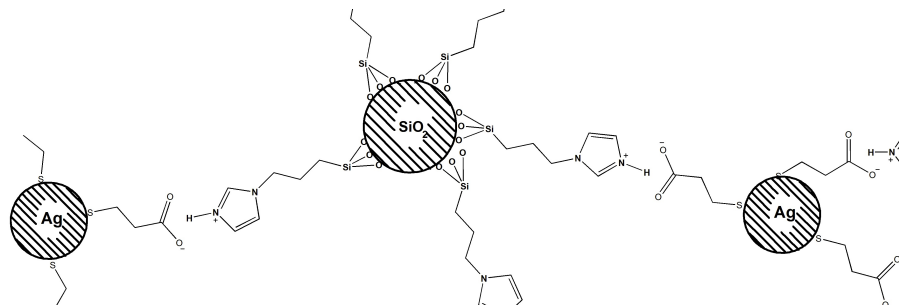
Figure 5.4: Scheme of nanoparticle network based on silica and silver nanoparticles.

In order to determine the size of the synthesised silver nanoparticles, XRD and UV-Vis measurements of the final material were undertaken (Figure 5.5). The X-ray diffractogram obtained, confirms the reduction of the silver cations. The reflexions are characteristic for metallic silver. By applying the Scherrers equation (Chapter 4.1) on the silver (111) reflexion at 38°, an average diameter of silver crystallites of about 14 nm is afforded. Additionally, UV-visible absorption spectroscopy was carried out, since silver shows a strong plasmon absorption band. The maximum of this band can directly be correlated to the size of the nanoparticles.[182] It can be seen, that the maximum of the absorption, the black powder was dispersed in water, is centred around 410 nm for the silica/silver nanoparticle networks. This indicates the presence of silver nanoparticles with a size between 10 and 15 nm, which corresponds to the crystallite size estimated by XRD.
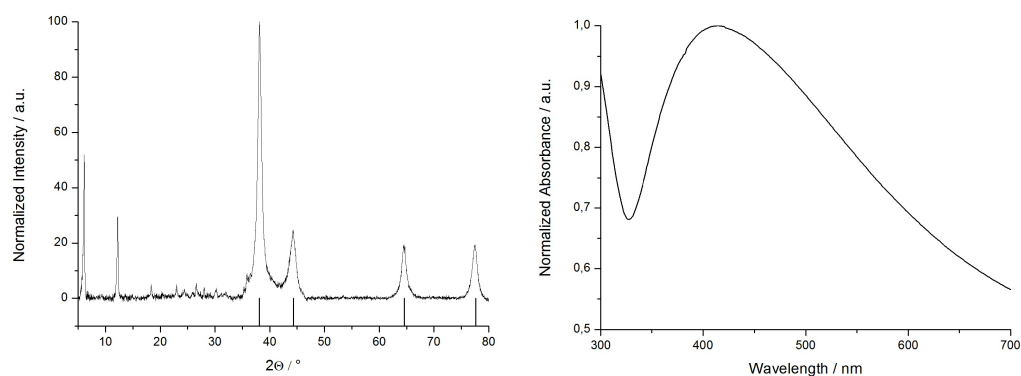
Figure 5.5: XRD and UV-Vis measurements of silica/silver nanoparticle networks.

Further, the signals in the XRD pattern, not belonging to the silver nanoparticles

at very low diffraction angles, 12 and 6°, was already reported for ionic liquids based on imidazolium, 6 to 10 carbon atoms in the alkyl chains, and spherical or highly symmetrical anions.[183] Thereby, this feature is related to intermolecular interactions between the imidazolium species and to the anisotropy of the imidazolium cation, present in the mixed nanoparticles material. Here, the imidazole interacts with the carboxylic acid to form charged imidazolium units, even without long mesogen alkyl chains. Therefore, the charged species are forced to stay close to another.

Another test, which proves that two different kinds of nanoparticles are contained within the system, was performed through treatment of the final material with HF on the one hand and HNO$_3$ on the other. Afterwards DLS measurement were carried out again (Figure 5.6). Through the usage of HF, the silica nanoparticles were dissolved, and therefore also the network is partly destroyed. In the DLS measurement silver nanoparticles with a broad size distribution centred around 7 nm radius are obtained. This findings are in perfect agreement with the size estimated by XRD and UV-Vis. The large aggregates visible in the spectrum can be explained by insufficient treatment of the powder with HF. Further, the usage of HNO$_3$ leads to the dissolution of silver. A DLS measurement shows signals around 200 to 400 nm deriving from agglomerates of silica nanoparticles. These agglomerates are due to the fact, that an aqueous nitric acid was used for dissolving the silver nanoparticles, inducing condensation reaction between the silica nanoparticles. Again, this results correspond to the presence of a silica/silver nanoparticle network.
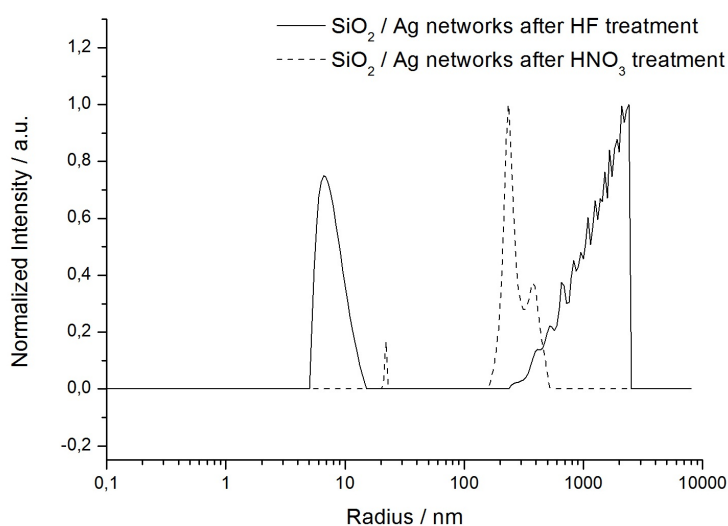
Figure 5.6: DLS measurements of silica/silver nanoparticle networks after HNO$_3$ and after HF treatment.

In Chapter 3.3 it is shown that the transformation of an imidazole into an imidazolium can be followed by means of solid state CP MAS ^{15}N NMR spectroscopy. A solid state CP MAS ^{15}N NMR was measured after the reaction of the imidazole functionalised silica nanoparticles with 3-mercaptopropionic acid (Figure 5.7). In this case the observed nitrogen peak is centred on 139 ppm, with a shoulder at lower field. For the silica nanoparticle networks, the main signal could be divided into two regions. One being around 142 ppm, deriving from the imidazolium species, and one around 135 ppm, attributed to the nitrogen atoms of the imidazole units. For the imidazole/thiol functionalised nanoparticles the peak is slightly shifted towards lower field. The characteristics of the peak are nevertheless an indication for the formation of the imidazolium units. The shift can be a result of the hydrogen bonding of the carboxylate to the imidazolium, and is even more pronounced for solid state NMR spectroscopy.[184] This observation correlates with the evolution of the broad peak at low field, observed for the N-H specie in Figure 5.2 for the liquid *N*-methylimidazolium mercaptopropionate.
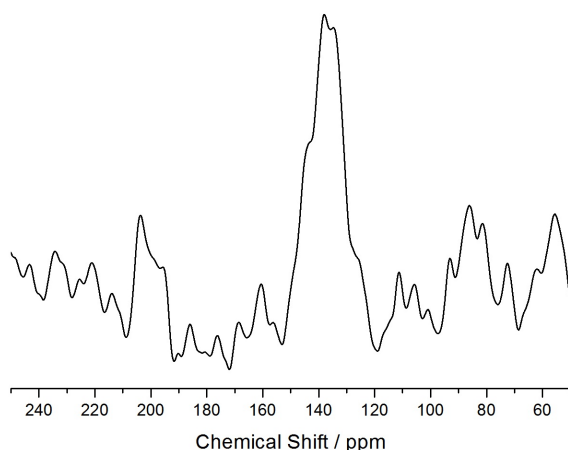
Figure 5.7: ^{15}N CP MAS NMR spectrum of silica nanoparticles modified with imidazole and reacted with 3-mercaptopropionic acid.

Further, FTIR spectroscopy was measured to show the formation of the silica/silver networks (Figure 5.8). The reaction in the liquid state, between *N*-methylimidazole and 3-mercaptopropionic acid without silica nanoparticles, shows the presence of a band at $1950\,\mathrm{cm}^{-1}$. This band is characteristic for the formation of the N-H bond by the transfer of the proton from the carboxylic acid groups to the imidazole group, thus forming the imidazolium unit. The formation of this band was already reported as a signature of imidazolium carboxylate and pyridinium carboxylate species.[180] Further, the reduction and broadening of the C=O stretching

vibration band at $1700\,\mathrm{cm}^{-1}$ is an indication for the presence of CO_2^- moieties. For the material obtained, using the same reaction on imidazole modified silica nanoparticles, these characteristic vibration bands deriving from the proton transfer of the carboxylic acid group can be observed around $1950\,\mathrm{cm}^{-1}$. Here, a very broad adsorption between $1515\,\mathrm{cm}^{-1}$ and $1720\,\mathrm{cm}^{-1}$ reveals the attending presence of carboxylate antisymmetric C-O stretching vibrations.
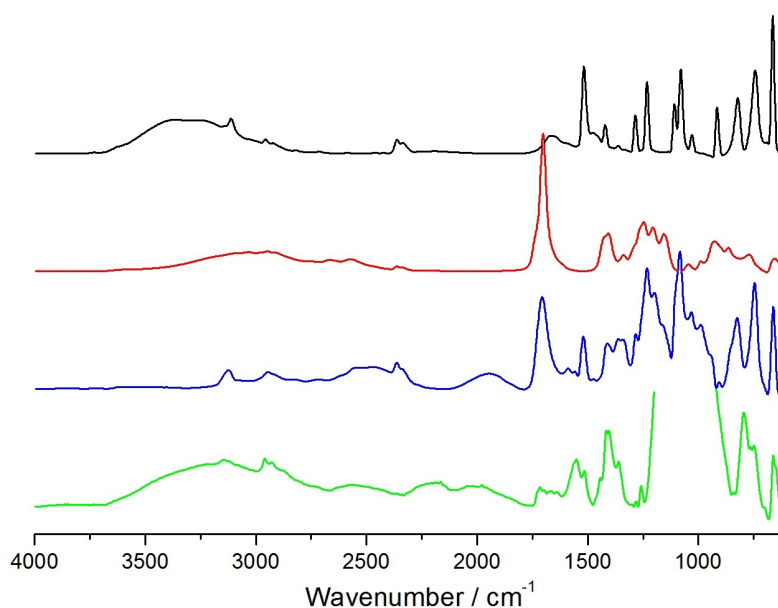
Figure 5.8: FTIR measurements of (from top to bottom) N-methylimidazole, 3-mercaptopropionic acid, N-methylimidazolium propionate and silica nanoparticles modified with N-(trimethoxysilylpropyl)imidazole and reacted with 3-mercaptopropionic acid.

To get a qualitative picture of the formed networks, SEM with EDX analysis were carried out (Figure 5.9). The SEM image shows macroscopic objects with a rough surface, deriving from the broad size distribution for diameter of the silver nanoparticles, as shown in UV-Vis (Figure 5.5). Furthermore, it is visible, that these objects are built up by spherical nanoparticles. The bright spots are due to charge phenomenons of the silver nanoparticles. EDX, obtained of the hybrid material, shows the expected signals for the nanoparticles on the one hand (Ag, Si and O) and for the linking unit on the other (N, C, S). This delivers only a qualitative picture, as EDX analysis is a surface technique.
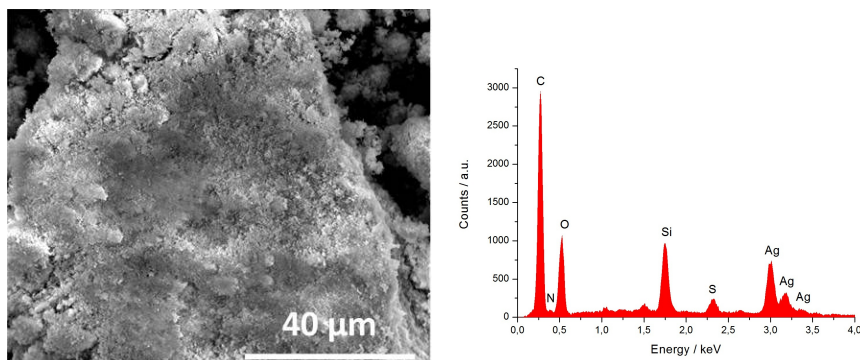
Figure 5.9: SEM and EDX analyses of silica/silver nanoparticle networks.

Since the resolving power of SEM is limited to objects of about 50 nm in size, high resolution (HR) TEM images was were recorded (Figure 5.10). In the images one can distinguish between two differently sized nanoparticles. Thereby, the darker particles seem to be distributed equally, but with a rather broad size distribution. Since silver possess a higher electron density, it appears darker in TEM. If the resolution is increased (Figure 5.10 right) the lattice of the silver nanoparticles can be observed. Furthermore, also the size of the nanoparticles of about 15 nm correlates to the results measured through DLS and XRD.
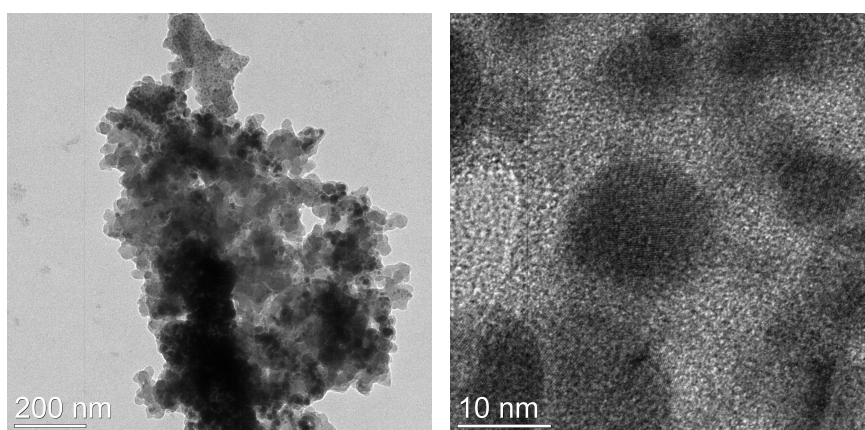
Figure 5.10: HR-TEM images of silica/silver nanoparticle networks.

5.3   Conclusion

In this chapter the formation of silica/silver, nanoparticle networks was shown. For this purpose imidazole modified silia nanoparticle were treated with 3-mercaptopropionic acid. Thereby, the proton from the carboxylic acid group was transferred to the imidazole, thus forming the imidazolium moieties. The mesoscopic arrangement of the imidazolium units, forced by the self-assembly of these, could be verified by means of X-ray diffraction. Afterwards, silver nanoparticle were introduced, thus forming a network were the metal nanoparticles are neighboured by metal oxide nanoparticles and reciprocally. It could be shown through DLS measurements, before and after treatment of either HNO_3 or HF, that two kinds of nanoparticles are present in the hybrid material. Furthermore, SEM and TEM measurements showed an equal distribution of the silver and silica nanoparticles in the material.

Chapter 6

Processing of Nanoparticle Networks

For the fabrication of a thin film of ionic nanoparticle networks, a layer by layer deposition method was used. A silicon wafer with a native oxide layer was coated with N-(trimethoxysilylpropyl)imidazole. In a second step, suspensions of sol-gel derived titania nanoparticles modified with 3-chloropropylphosphonic acid (Chapter 4.1.2) were prepared. The connection of the nanoparticles to the surface was then established through a reaction of these modified nanoparticles with the corresponding imidazole entities on the surface. Using this process either one or several times, mono- and multilayers of titania nanoparticles could be produced.

6.1 Assembly of a Single Layer of Titania Nanoparticles on Silicon Surfaces

In this chapter the fabrication and investigation of a single layer of titania nanoparticles on silicon surfaces will be discussed (Figure 6.1).
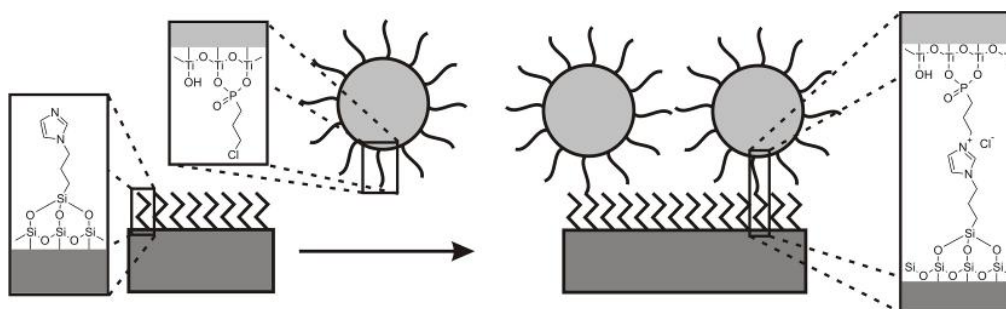
Figure 6.1: Process for the formation of a titania nanoparticle monolayer.

Prior to the first step of the synthesis, the silicon wafers (100 orientation, 0.5 x $1\,cm^2$ in size) were activated through treatment with UV/ozone. This treatment causes excitation and/or dissociation of contaminants, which will form volatile molecules together with oxygen radicals.[185] Afterwards the wafer substrates were immersed into a 0.1 molar solution of N-(trimethoxysilylpropyl)imidazole in ethanol. To remove unreacted ligands from the surface, the silicon samples were ultrasonicated and washed with isopropanol. Through ellipsometric measurements the thickness of the first layer was evaluated. It could be shown, that the height of the layer increases with longer deposition times, leading to a maximum of 0.31 ± 0.05 nm after 30 minutes (Figure 6.2). This value is in good agreement for the expected value for a complete monolayer of this molecule, with a relatively low degree of order. It originates from the short alkyl chain length of the ligand. Longer chains are known to form dense monolayers, caused by a self-assembly on the surface, e.g. octadecyl-chains.[186] Afterwards the silicon wafers were immersed into a $0.1\,mg\cdot ml^{-1}$ solution of titania nanoparticles, surface functionalised with 3-chloropropylphosphonic acid followed by the same cleaning procedure as described above. As shown in the chapters before, the covalent bonding of the nanoparticles proceeds through a nucleophilic substitution reaction between the chloroalkyl and the imidazole functionalities. Again, the thickness values obtained by ellipsometric investigations, varied with the time of deposition. Thereby, the reaction proceeds at a much lower rate, thus requiring several hours to reach saturation. A value of 2.63 ± 0.25 nm was obtained after 21 hours (Figure 6.2).
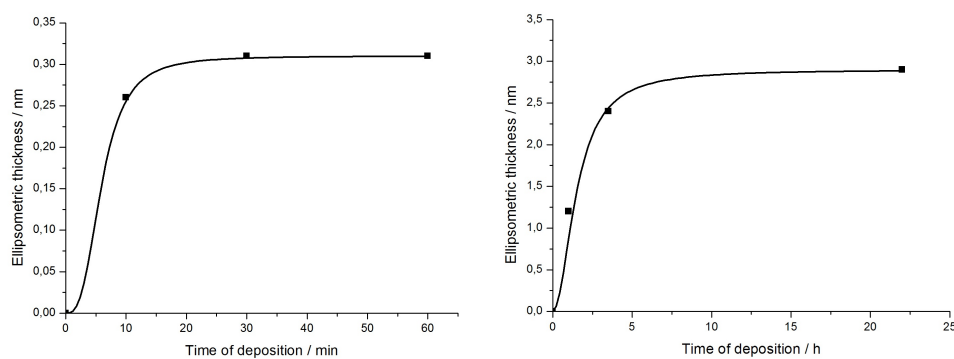
Figure 6.2: Ellipsometric thickness after various minutes/hours of deposition of N-(trimethoxysilylpropyl)imidazole on a silicon surface(left) and chloro modified titania nanoparticles on an imidazole funtionalised silicon surface (right).

Through a mathematical growth model it can be estimated, that this maxima is reached after approximately 10 hours. This much higher deposition time is a results from the, on the one hand, lower concentration of functionalised titania nanoparticles in solution, compared to the solution of the imidazole, and, on the other hand, the kinetically much slower reaction between the two moieties. Although one would expect thicknesses of about 4 nm, the diameter of the nanoparticles, one has to keep in mind, that ellipsometry yields only the equivalent height for a dense layer, whereas the particle layer contains voids. Therefore, the ellipsometric thickness is equivalent to about 60 % of a hexagonal closed packing of 4 nm diameter nanoparticles. Thus, the obtained height is close to the random close packing limit for a system based on spherical shaped nanoparticles.

For further investigations atomic force microscopy (AFM) was measured (Figure 6.3). It can be seen, that a fully covered surface, with titania nanoparticles, was obtained and no spots from the silicon surface are visible. It is obvious, that through the described approach a very homogeneous surface of titania nanoparticles can be obtained. The higher features, observed in the AFM image are caused by either bigger particles or agglomerates.
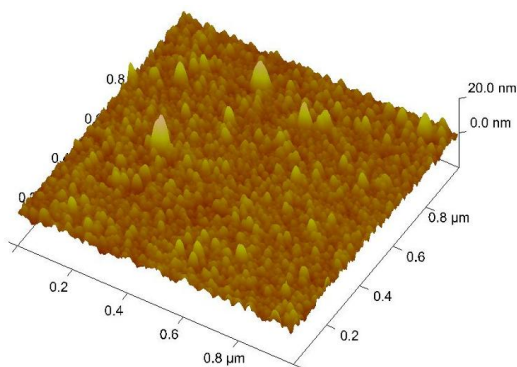
Figure 6.3: AFM image of a nanoparticle monolayer on an imidazole functionalised silicon substrate.

To get more insight on the character of the bonding of the titania nanoparticles onto the silicon surface, X-ray photoelectron spectroscopy (XPS) measurements were carried out (Figure 6.4). As a reference, next to the covalently linked titania nanoparticles, unbound nanoparticles modified with 3-chloropropylphosphonic acid were measured. For the measurement, the nanoparticles were deposited on a carbon pad and transferred into the spectrometer. As for the unbound nanoparticles strong peaks for oxygen (1s at 540 eV), titanium (2s at 560 eV, 2p at 460 eV, 3s at 60 eV and

3p at 40 eV), chlorine (2s at 270 eV and 2p at 200 eV) and phosphor (2s at 191 eV and 2p at 133 eV) are observed. A carbon peak at 290 eV is present, but it is mainly caused by the carbon pad and the remaining gas within the chamber, superposing the signal of the hydrocarbon chain of the particle coating.

For the nanoparticles bond to the silicon substrate, next to the peaks described above, signals for nitrogen at 400 eV, corresponding to the presence of N-(trimethoxy-silylpropyl)imidazole, as well as silicon (2s at 150 eV and 2p at 100 eV) from the substrate and the silane, are present. Again, a carbon peak from the background superposes the expected signals of the sample. Further, the very strong oxygen signal is dominated by the silicon oxide from the substrate, although a low energy shoulder is visible which is due to the Ti-O bonds. As for the chlorine peak, around 200 eV, one would expect a shift, because of a change in the chemical bonding of the atom. Nevertheless, when an imidazole-modified substrate is treated with a free chlorine containing organic linker, without nanoparticles, a shift of the signal is clearly visible, attributed to the conversion of the chlorine to chloride.[187] There are several factors explaining the absence of this effect in the present sample. First, the overall intensity is very low, leading to a poor signal to noise ratio, and second there is only a small number of direct links between the nanoparticles and the substrate, due to the curvature of the nanoparticles. Most of the chlorine entities are 'shielded' by the nanoparticles themselves, and are therefore, not undergoing any chemical changes.
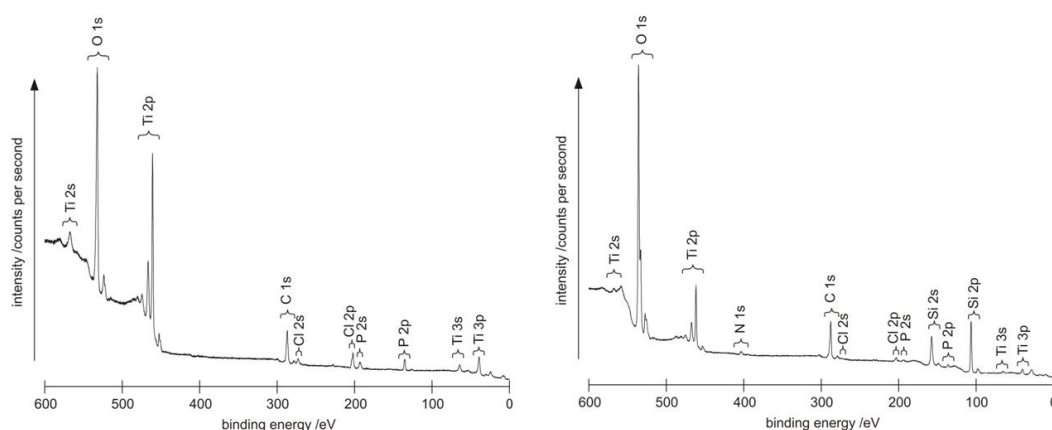
Figure 6.4: XPS spectrum for titania nanoparticles modified with 3-chloropropylphosphonic acid (left) and titania nanoparticles monolayer on a silicon support with thick oxide (right).

Having provided a proof of the formation of the imidazolium binding unit, the next step was to investigate the selectivity of the deposition of the titania nanoparticles. This selectivity, next to the high homogeneity and surface coverage of the monolayers, can be proven by the construction of structured layers of titania nanoparticles. Therefore, native oxide layers where passivated by deposition of an octadecyltrichlorosilane monolayer and locally oxidized using AFM with an applied voltage of -7 V between tip and sample. After this treatment only small changes in height could be detected, attributed to swelling phenomenons of the underlying silica substrate.

Subsequent to the removal of the passivating self-assembled monolayer, the samples were modified with surface functionalised titania nanoparticles in the same manner as described above. To visualise this selectivity AFM images were recorded (Figure 6.5). The images show a highly specific deposition of titania naoparticles on the previously oxidised spots. Only very few particles are visible outside the oxidised pattern.
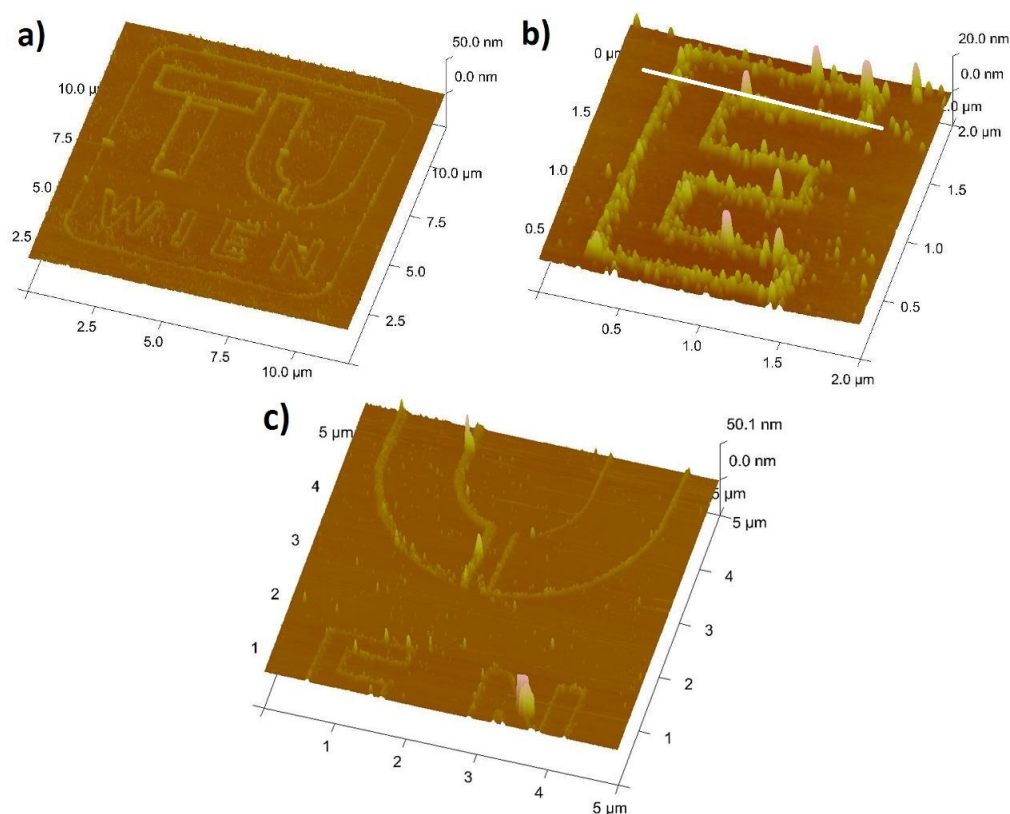
Figure 6.5: AFM images of a structured nanoparticle monolayers deposited onto a pre-patterned surface; a) shows the full pattern and b) and c) show part of this structure at a higher resolution, resolving individual nanoparticles.

Through AFM, also the height of the nanoparticles pattern can be estimated (Figure 6.6). In the image a cross-section through the 'E' of the pattern in Figure 6.5 (indicated with a white line) is shown. An increase of 4 to 6 nm, with only small deviations, can be observed at the expected distance. These values corresponds well with the results obtained for the diameter of the titania nanoparticles through DLS and XRD.
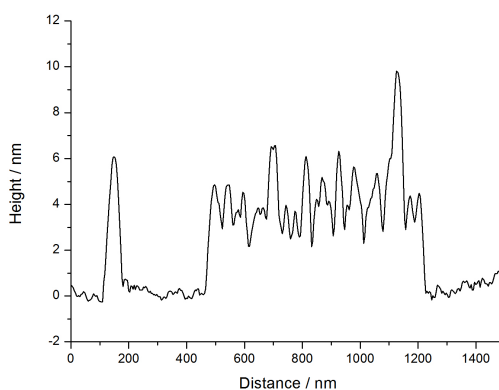
Figure 6.6: Height of selectively deposited nanoparticles, measured by AFM.

6.2 Assembly of a Multilayers of Titania Nanoparticles on Silicon Surfaces

Through the methods described, dense monolayers of titania nanoparticles are fabricated. Since the nanoparticles are homogeneously surface funtionalised, the chloro-alkyl moieties are still available. To form multilayer samples, repeated immersions into the N-(trimethoxysilylpropyl)imidazole and chloride modified titania nanoparticle solutions, or suspensions on the case for the nanoparticles, respectively, were performed. Ellipsomety measurements were performed after each individual layer of either linker or nanoparticles (Figure 6.7). As shown in the previous chapter the first layer of imidazole linkers and chloro-modified nanoparticles exhibit a thickness of about, 0.29 ± 0.05 and 2.63 ± 0.25 nm respectively. After immersion into a solution of linker (layer 3 in Figure 6.7) the value more than doubles to 0.71 ± 0.09 nm. Next to this, it was observed that the deposition time needed for saturation was much higher, increasing from about 30 minutes to several hours. These facts can be explained by the higher specific surface of the nanoparticle layer as compared to the flat silicon substrate. Thus, the deposition of the linker is thereby

governed by a lower diffusion rate between the nanoparticles. The second layer of particles (layer 4 in Figure 6.7) shows the same height as the initial monolayer of titania nanoparticles.

For the fifth layer (third layer of linker) again the same values as before were measured, confirming that the amount of nanoparticles in the previous layers are identical. The sixth (third layer of nanoparticles) and last layer shows a 40 % higher value for the thickness, 3.74 ± 0.27 nm. Again, this increase derives from the higher specific surface, thus offering more anchoring possibilities for the particles.
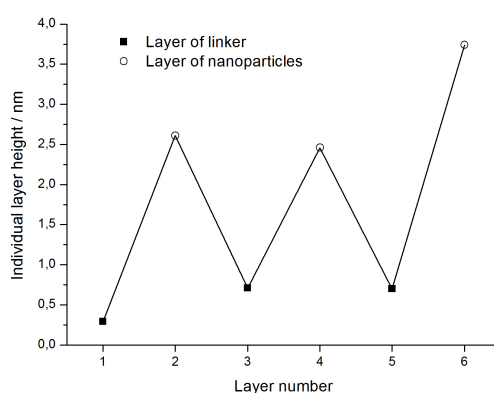
Figure 6.7: Ellipsometrically determined height for each individual layer.

These samples, 3 layers of linker and 3 layers of nanoparticles alternating, were further investigated through AFM (Figure 6.8). It can be seen that the roughness, compared to the samples containing only a monolayer of particles increases.
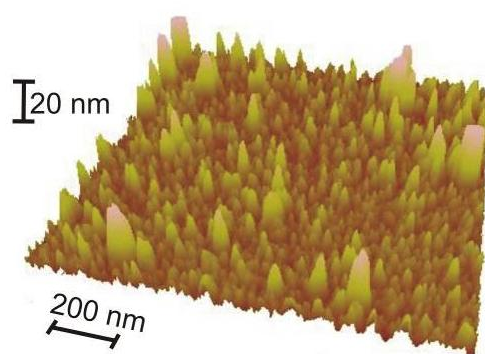
Figure 6.8: AFM image of the surface topography after 3 layers.

6.3   Stability of Mono- and Multilayers of Titania Nanoparticles on Silicon Surfaces

Since the stability of such layers of nanoparticles could be of importance for many applications, e.g. dye-sensitised solar cells, several stability tests were undertaken. A first indication of a strong bond is, that after sonication in isopropanol for prolonged periods, with a minimum of 10 minutes, between the different steps of depositing either a layer of linker or nanoparticles, no degradation, regarding ellipsometric measurements, occurred.

Another test was performed by lateral force microscopy (LFM) of samples containing three layers of nanoparticles and linkers respectively (Figure 6.9). By using LFM with the AFM cantilever, shear forces are applied onto the samples during scanning in contact mode. Thereby, the pressure of the cantilever also changes the shear force and, thus, the mechanical stability can be evaluated. Varying contact forces have been applied. It could be observed, that the surface did not undergo any crucial changes when lower pressures of about 0.7 nN—diagonal forces in Figure 6.9—and 7 nN—horizontal forces— are applied. The changes are only minor (0.2 nm). This effect can be either attributed to a compression of the multilayers of nanoparticles, or to a rearrangement of the particles within the layers. At a pressure of 36 nN—vertically applied forces—the formation of deeper trenches accompanied by a deposition of accumulations of nanoparticles on the edges, was visible. This test indicates that a covalent bonding of the nanoparticles to the silicon surface is present, but since there is only a low number of anchoring points, the overall stability is rather low. When performing a height analysis of the corresponding vertical trench (Figure 6.9), one can see two discrete steps in the height of about 3.5 nm each. This value directly corresponds to the size of the nanoparticles. Since the particles are not directly positioned on a flat surface, but rather in the cavities of the underlying particles layer, this value is slightly smaller than 4 nm, obtained through XRD measurements.
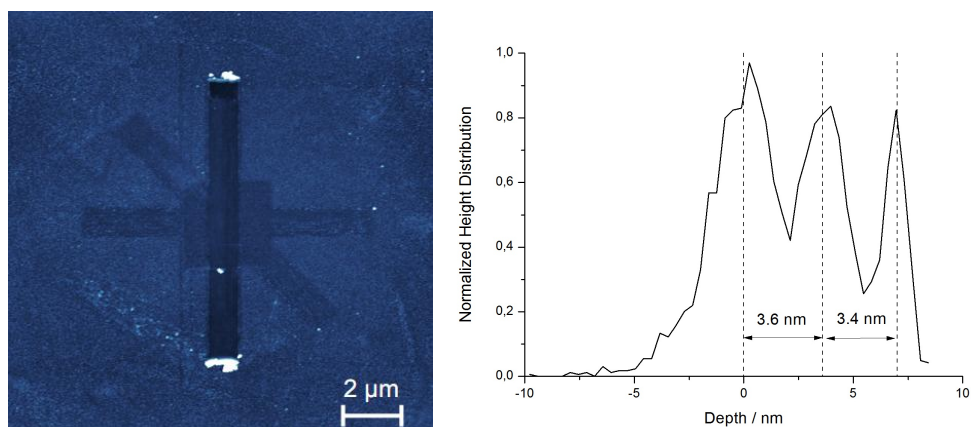
Figure 6.9: AFM image after scratching in LFM mode with various forces (right), and statistical evaluation of the height distribution (right).

Further, as mentioned in Chapter 1.2.3, Si-O-Ti bonds, as for the multilayered system, are in general known to be unstable towards hydrolysis. Nevertheless, many examples of stable monlayers, build up by these bonds can be found in literature.[188–191] Since P-O-Ti bonds are stable, mulitlayers of nanoparticles were formed using the phopshonic acid equivalent. For this purpose a solution of N-imidazolyl-propylphosphonic acid acid was prepared (Chapter 4.1.2) and the multilayers were formed in the same manner as for the alkoxysilane-based ligands. It was found, that by applying the same deposition times as for the alkoxysilane system, a timerange of 21 hours was needed for a full coverage, for the phosphonic acid and a subsequent layer of titania nanoparticles, the ellipsometrically determinded values were significantly lower. For a layer of the phosphonic acid 0.21 ± 0.09 nm and for the adjacent nanoparticles 0.65 ± 0.07 nm were obtained. This values are only about 30 %, compared to the siloxane-based system. By increasing the time of deposition to several days, higher values can be obtained. The stability of these multilayers, based on P-O-Ti bonds were tested. As before, ultrasonication in isopropanol did not lead to any degradation of the layer. LFM investigations showed a slightly lower stability toward mechanical wear. Here, no formation of trenches up to 48 nN was observed. This test points out to a covalent bond between the nanoparticles and the silicon surface.

Since, titania nanoparticles are known to be photocatalytically active and therefore are able to degrade organic moieties (Chapter 4.1.3), the samples containing multilayers were exposed to 254 nm UV-light. This exposure, 100 minutes with 12 mW·cm^{-2}, led to the expected significant reduction in the ellipsometrically de-

termined layer thickness, from 8.97 to 7.42 nm, which is equivalent to the removal of 60 % of the organic ligands within in the film. AFM as well did not show any changes in the surface morphology. By comparing XPS measurements (Figure 6.10) from the multilayers before and after irradiation, however, one can see considerable changes. First the chlorine peaks at 200 eV completely disappear. Second, the nitrogen peak around 400 eV is greatly diminished, which hints to a degradation of the imidazolium units. Further, the phosphorous signal at 133 eV did not change, considering its intensity, but is rather shifted to to higher energies. This shift hints to the fact, that the phosphor of the anchoring unit is oxidised to a phosphate, which remains bond to the surface of the titania nanoparticles. This effect is also reported in literature.[53,192]
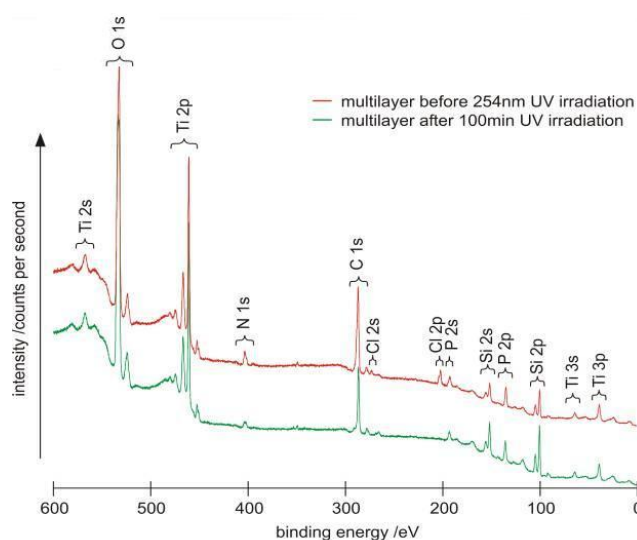
Figure 6.10: XPS spectra of a multilayered sample with phosphonic acid-based linkers between the particle layers.

To see if the titania nanoparticles are still covalently linked to the silicon surface, thus a mechanical stability is still present after illumination with UV-light, again LFM measurements were carried out (Figure 6.11). It can be seen, that the multilayers show higher stabilities towards lower forces. For 0.7 and 7 nN—horizontally and diagonally applied forces in Figure 6.11—no formation of trenches are observed. This indicates, that either weaker bound organic moieties were removed after UV-treatment, or a rearrangement of the nanoparticles took place. By raising the contact forces up to 36 nN—vertical forces—a deep trench is visible caused by the removal of the nanoparticles. This test indicates, that the removal of the organic moieties through UV-irradiation did not cause any drawback considering the mechanical sta-

bility. Moreover, the particles are still covalently connected to the surface through O-Si-O, or O-P-O bonds. In literature this phenomenon was already reported,[193] where the oxidation of organosilanes led to the formation of stable SiO_2 layers covalently linked through O-Si-O bonds.
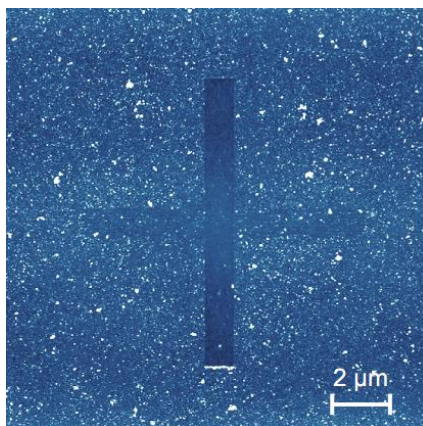
Figure 6.11: AFM image after scratching in LFM mode at various forces after UV-irradiation.

6.4   Conclusion

In this chapter the fabrication of mono- and multilayers of metal oxide nanoparticles on a silicon substrate was shown, by applying the methods to build up ionic nanoparticle layers with high packing densities. Thereby, the nanoparticles are covalently bonded to the substrate through imidazolium units. The nature of the bonding was investigated through XPS and AFM measurements. Further, the deposition of the nanoparticles was controlled by passivation of the silicon wafer with long, self-assembling, alkyl-chains, and selective removal of these. Stability test were carried out using LFM. These test indicated, that both phosphonic acid-titanate as well as siloxane-titanate bonds show sufficient stability for the three dimensional nanoparticle assemblies on surfaces. The mechanical stability of these multilayers was also tested after UV-treatment. It could be shown, that through removal of the organic moieties the mechanical stability was not diminished. The nanoparticle are still covalently linked to the surface through O-P-O or O-Si-O bonds.

Chapter 7

Surface Modification of Cellulosic Aerogels

In the last chapters it was shown, that the surface properties of nanoparticles can be tuned, using coupling agents bearing silane or phosphonic acid functional groups. In each case, the sol-gel functionalisation reaction is possible owing to the presence of hydroxy groups on the surface. In this chapter cellulosic aerogels were modified with alkoxysilane coupling agents, and the properties of the obtained materials were investigated.

7.1 Cellulosic Aerogels

Cellulose is the most abundant natural biopolymer on earth (Figure 7.1),[194–196] and is mainly used in the pulp, paper and fibre industries. Nowadays the fields of applications is shifted to the development of cellulose-based biomaterials,[197] e.g dialysis membranes or as scaffolds to grow functional cardiac cell constructs.[198]
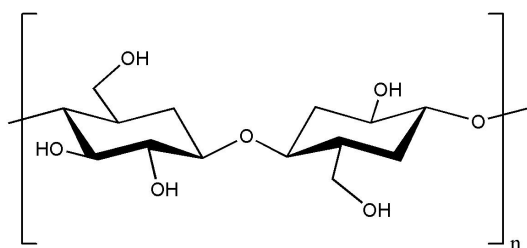
Figure 7.1: Chemical structure of cellulose.

For such applications shaped cellulosic aerogels have been recently developed.[199–204] The route of preparation is similar to the production of silica aerogels (Chapter 1.2.1). The starting material for cellulose gels can be both plant and bacte-

rial resources. As described by Liebner *et al.* cylindrical cellulose alcogels can be prepared by dissolving 3 % cotton linters in molten *N*-methylmorpholine-*N*-oxide monohydrate (NMMO, Figure 7.2), at around 120 °C. Two points are relevant for the usage of NMMO. First, it is a relatively strong oxidant and second, cellulose solutions tend to be unstable in this organic component.
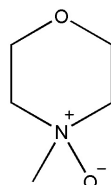
Figure 7.2: Chemical structure of *N*-methylmorpholine-*N*-oxide.

The resulting gels can be casted, by pouring the melt into cylindrical polyamide forms, and regenerated by shaking the alcogels in dry ethanol to remove NMMO and it's side products like tertiary amine *N*-oxide. Aerogels can be further obtained by supercritical drying with CO_2 (Figure 7.3).

Figure 7.3: Lyocell bodies at different stages of the aerogel production: solidified NMMO melt containing 3 % cellulose (left), cellulose gel after regeneration (middle) and supercritically dried cellulose aerogel (right). [203]

Through this route, very lightweight materials with very low specific densities of down to 8 mg·cm^{-3} are obtained. The network of cellulose consists of an interconnected open-pore structure, which preservation is essential for many applications in the field of biomaterials. Beside the positive aspects of cellulose aerogels, however, these new materials lack sufficient mechanical stability. One approach to improve the mechanical properties of cellulosic materials on the one hand, and to maintain the porous network on the other hand, is the surface modification with silica. [205–208] As said before, this chemical modification is possible through the hydroxide groups provided by the chemical structure of cellulose. Through the surface modification, also the tuning of certain properties is possible, e.g. Goncalves *et al.* used fluorosiloxanes as silica precursor to get superhydrophobic surfaces. [207] Other studies evidenced the possible improvement of thermal and mechanical properties

by silica modication.[207–219] It can be seen, that the catalytic hydrolysis of tri- or tetraalkoxysilanes with subsequent condensation of the intermediary formed silanols is obviously the most commonly used approach for silica reinforcement,[214,217,219] thus presenting the starting point of this study.

7.2   Modification of Cotton Linter Alcogels

Following the studies mentioned before, silica modication of cellulose alcogels, prepared as described above from cotton linters, was accomplished according to a sol-gel approach using ethanol as solvent. Four different sols were prepared at varying concentration of tetraethoxysilane (TEOS), 3-chloropropyltrimethoxysilane (CPTMS), and HCl as catalyst (Table 7.1).

Table 7.1: Composition of the sols prepared for silica modification and selected pore characteristics of silica modified and scCO$_2$ dried cellulose aerogels from cotton linters .

	CL	CL1	CL2	CL3	CL4
TEOS:CPTMS:HCl / ml	0:0:0	3:0:0	3:0:6	0:3:0	3:3:0
Surface area / $m^2 \cdot g^{-1}$	255	220	290	265	245
Sorbed volume / $cm^3 \cdot g^{-1}$	0.65	0.55	0.65	0.64	0.61
Average pore diameter / nm	10	10	8.5	8.9	9.3
Elemental analysis C / $w\%$	44.44	41.42	38.41	41.47	41.64

Into these solutions, the cellulose alcogels (1 x 1 x 3 cm^3 in size), prior to supercritical drying, were submerged for 24 hours under stirring. In Table 7.1, CL corresponds to the untreated cotton linter aerogels. In a SEM image a porous network can be seen for the supercritical dried, unmodified sample CL (Figure 7.4). Further, nitrogen sorption at 77 K of this unmodified sample, exhibits a high surface area of 255 m^2·g^{-1}, next to a high sorbed volume of 0.65 cm^3·g^{-1}. These two values are characteristic for cellulosic aerogels and their interconnected pores.
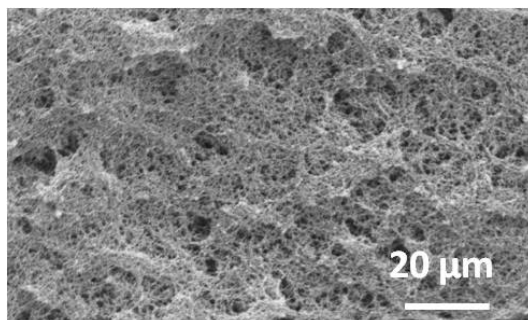
Figure 7.4: SEM picture of cotton linter aerogel prior to silica modification.

Within this chapter this sample will be taken as a reference. Further, the composition of the sol used for sample CL1 corresponds to the protocol published by Maeda *et al.* for silica modication of cellulose xerogels.[214] The aim of their study was neither the preservation of certain pore features nor further functionalization of the cellulose/silica composite, but rather to improve the mechanical stability. The closing of the pores of the system can be seen, as the specific surface area significantly decreases to about $220 \, m^2 \cdot g^{-1}$ for sample CL1. Since this result is not desirable, considering the perpetuation of the porous character of the network, the three other sols, CL2, CL3 and CL4, where chosen to study the effects of an acidic catalyst and of 3-chloropropyltrimethoxysilane–the latter added as a co-precursor to introduce an anchor group for possible further functionalisations. After immersion in one of the different sols, the cellulose bodies were thoroughly rinsed with ethanol and subsequently dried with supercritical carbon dioxide at $40 \, °C$ and $10 \, MPa$.

Nitrogen sorption isotherms were recorded to investigate the effects of the different silica precursor ratios on the porosity of the modified samples (Figure 7.5). At a first glance, the obtained isotherms conveyed the impression that silica deposition by sol-gel processing generally maintained a very high porosity of the modied, $scCO_2$ dried aerogels (Figure 7.5). However, samples CL1, as mentioned above, and CL4 differ from the other variants. The decreasing sorbed nitrogen volume, up to $19 \, \%$ is most likely due to closure of open pores of the cellulosic matrix by deposited silica. Sample CL2 and CL3 show similar characteristics, considering the surface area and sorbed volume, compared to the reference sample. Even a slight increase in the surface areas can be detected, which is most probably caused by a surface-roughening effect of the silica deposition. Looking at the pore size diameter, one can see, that for CL2 and CL3 a reduction from $10 \, nm$ for CL, to about 8.5 to $9 \, nm$ took place. This, and the increased surface area, lead to the conclusion that the silica is deposited mainly at the surface of the pores. Based on the data reported in

Table 7.1 it can be summarized that the silica modication with all four different sols, and subsequent scCO$_2$ drying did neither signicantly alter the pore characteristics nor the cellulose network of the aerogels.
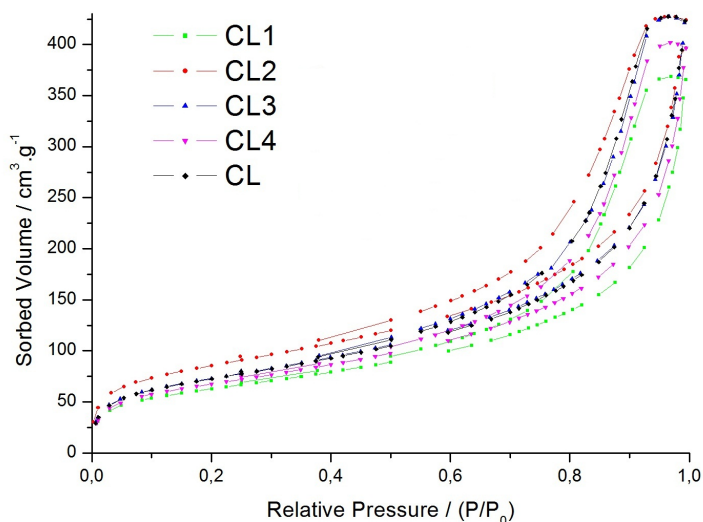
Figure 7.5: N$_2$ sorption at 77 K of the cellulose aerogels prior to (sample CL) and after silica modification (CL1-CL4).

To further confirm and quantify the modification of the cellulose aerogels with an inorganic part, TGA measurements were conducted (Figure 7.6). For all samples similar profiles are obtained. The first initial weight loss, between 25 and 100 °C corresponds to the evaporation of residual solvent, in this case ethanol. In the temperature range of 100 to about 270 °C the TGA curves of all samples behave as reported in literature, and a continuous release of small amounts of water is observed, with a maxima of about 2 w%. Beyond 270 °C all samples start to degrade. The main pyrolysis product is reported to be levoglucosane, which possesses, as cellulose, a six carbon ring structure.[220,221] This degradation is almost finished around 370 °C with weight losses ranging from 68 % for sample CL1 to 56 % for CL2. Samples CL3 and CL4 behave quite similiar with weight losses of about 64 %. The residual mass, thus the amount of silica within the sample, after 500 °C is the highest for sample CL2. This results fit with elemental analysis, where the carbon amount is the lowest for all samples (Table 7.1).
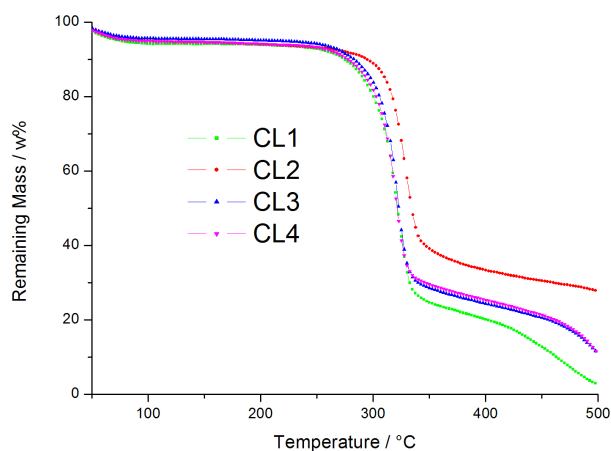
Figure 7.6: Thermogravimetric analyses of silica modified and scCO$_2$ dried cotton linter aerogels.

The difference of about 8 w% between sample CL2 and the other samples may be explained by the fact, that only for this specimen an acidic catalyst was used. Furthermore, sample CL2 seems to be more stable, since a shift of the onset temperature for the degradation, of about 10 °C is visible. This effect is consistent with the results described. Comparing the results obtained for the other samples, it seems, that the use of a functional trialkoxysilane, in our case 3-chloropropyltrimethoxysilane for samples CL3 and CL4, significantly alters the amount of silica left within the samples.

To get a closer look on the structure of the pores, SEM images for the samples CL2, CL3, and CL4 were recorded (Figure 7.7). Sample CL2, with the highest amount of silica, reveals a distinct morphology. Small, between 5 to 10 μm in diameter, spherical objects are covering the surface of the aerogel body in a "crust-like" fashion. Further, it can be seen, that large cracks are crossing the surface. For samples CL3 and CL4 the modification seems to have led to a homogenously distribution on the surface. In the SEM pictures most of the macropores (above 50 nm) observed for the unmodified sample CL (Figure 7.4), seem to be blocked by a silica layer. However, the SEM micrographs do not show the mesopores (from 2 to 50 nm) that were characterized by nitrogen sorption experiments, thus the findings do not interfere with the results obtained before.
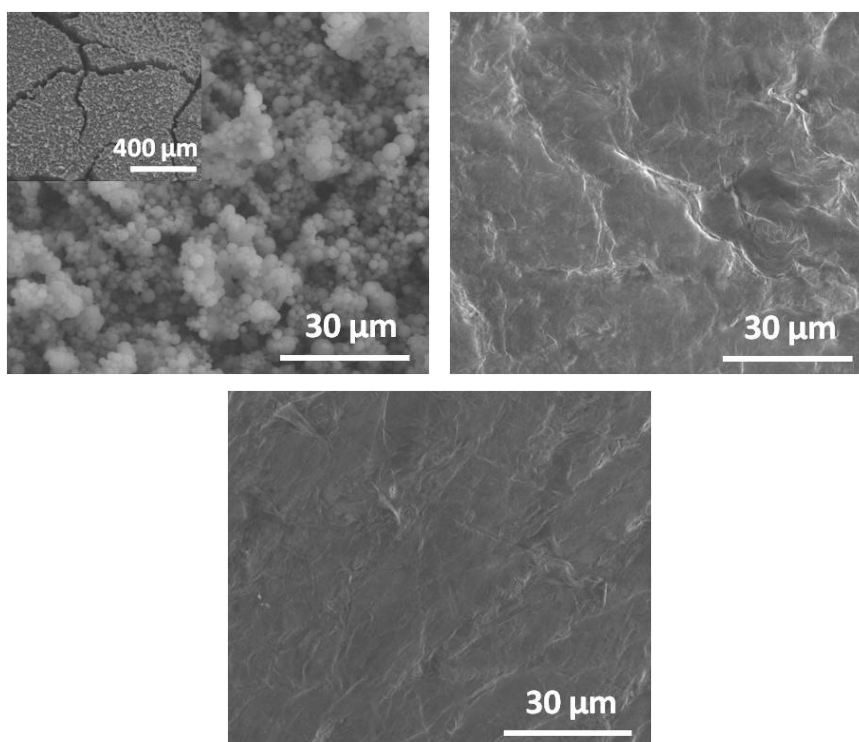
Figure 7.7: SEM pictures of cotton linter aerogels after silica modification (CL2 (upper left), CL3 (upper right) and CL4 (bottom)).

Further, EDX analyses were carried out for the samples measured by SEM (Figure 7.8). The two distinctive signals at lower energies, 0.33 and 0.55 keV, derive from the carbon and oxygen atoms from the cellulosic networks. The signals at 1.75 keV point to the presence of silicon atoms on the surface. Though, the signal for silicon seems to be more pronounced for CL2, for this sample the highest silicon amount was found through TGA measurements, EDX analysis does not allow quantification as it is a surface technique. Further, in the EDX measurements light elements are underestimated. Nevertheless, through EDX the presence of silicon on the surface can be confirmed for all modified cellulose aerogels.
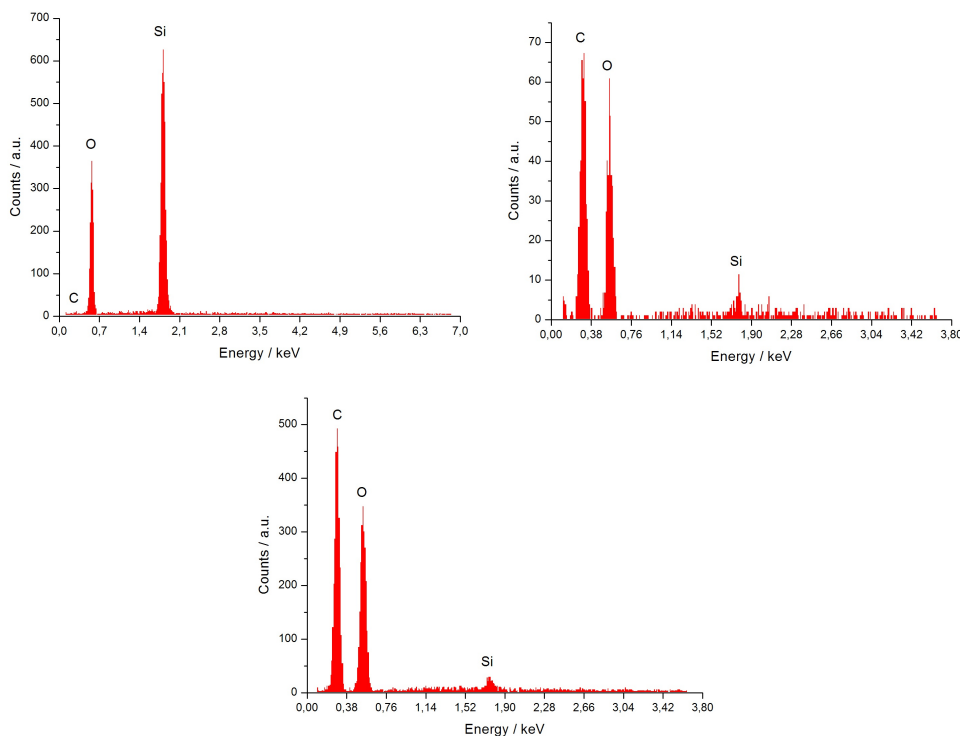
Figure 7.8: EDX measurements of cotton linter aerogels after silica modification (CL2 (upper left), CL3 (upper right) and CL4 (bottom)).

Gel permeation chromatography (GPC) studies were carried out to show the cellulose integrity in terms of molecular weight distribution. For samples CL2 a significant hydrolytic cellulose degradation was observed. Compared to the inital weight distribution of 150 kD for CL a three-times lower value, 54 kD, was obtained. Simultaneously an increasing carbonyl content in sample CL2 was observed. This is mainly attributed to the increasing number of reducing end groups. Here, the value increased from $5\,\mu\text{mol·g}^{-1}$ for the unmodified celulosic aerogel to about $29\,\mu\text{mol·g}^{-1}$ for CL2. This effect, the degradation of the cellulose backbone, next to the already shown formation of a crust at the surface, could be detrimental for several mechanical properties. It seems that the acid catalysed modification, albeit the high amount of silica, is not favourable for cotton linter cellulosic materials. As a conclusion it seem, that for samples, CL1, CL3 and CL4, the network is maintained.

7.3 Modification of Hardwood Pre-hydrolysis Kraft Pulp Alcogels

To support the results obtained with cotton linter derived cellulose materials, the modification of comparable cellulosic alcogel bodies from hardwood pre-hydrolysis kraft pulp was investigated. Again, four different sols were prepared, in which the alcogels were immersed for 24 hours, prior to drying with supercritical CO_2 (Table 7.2).

Table 7.2: Composition of the sols prepared for silica modification and selected pore characteristics of silica modified and $scCO_2$ dried cellulose aerogels.

	Sol	**Sol1**	**Sol2**	**Sol3**	**Sol4**
TEOS:CPTMS:HCl / ml	0:0:0	3:0:0	1.5:0:3	3:0:6	3:3:12
Surface area / $m^2 \cdot g^{-1}$	310	320	330	350	320
Sorbed volume / $cm^3 \cdot g^{-1}$	0.80	0.86	0.81	0.84	0.80
Average pore diameter / nm	10.2	10.2	9.8	9.6	10
Elemental analysis C / $w\%$	44.53	41.74	30.54	34.50	41.63

The sample Sol refers to the unmodified cellulose aerogels and therefore is taken as the reference sample. As for the cotton linter aerogels, Sol1 follows the work of Maeda *et al.*.[214] Further, Sol2 and Sol3 follow the compositions of CL 2, since the use of an acidic catalyst exhibited results, which should be investigated further. To see if the concentration effects the results of the modification, for Sol2 half of the amount of silane and catalyst, as for Sol3, was used. In the last composition, Sol4, again the co-silane, CPTMS, was used, next to a hydrochloric acid as an acidic catalyst. Here, double the amount of catalyst was used, since also the total amount of silanes is twice as much as normally used.

Nitrogen sorptions measurements at 77 K were conducted to examine the specific surface area, the sorbed volume and the average pore diameter of the different samples. Keeping in mind the surface area for the unmodified cotton linter derived materials with 255 m²·g⁻¹ (Table 7.1), one can see a significant increase of about 20 % to about 310 m²·g⁻¹ for the unmodified Sol samples (Table 7.2). For all the

other Sol samples, after modification, the surface areas increase for about 10 to $20\,m^2{\cdot}g^{-1}$, in comparison to the starting values. These results are surprising, since for Sol1 a decrease, keeping CL1 in mind, would have been expected. Further, Sol2 and Sol3, the same compositions as for sample CL2 was used, follow the results obtained for the cotton linter specimen, being the samples with the highest increases regarding the surface areas. Again, the last sample, Sol4 showed only a slight raise. As for the nitrogen sorption isotherms no significant differences between the unmodified and silica modified samples can be examined (Figure 7.9). Only sample Sol1 shows a slight increase concerning the sorbed volume. From these results it can be presumed, that, again, the porous character of the cellulosic material is preserved.
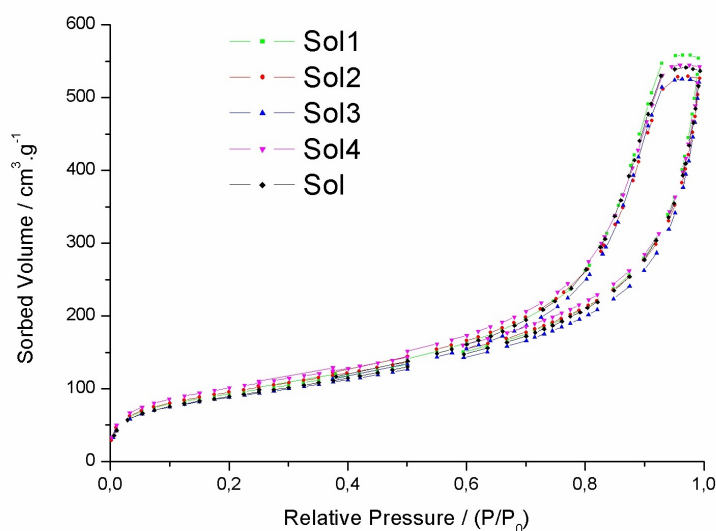
Figure 7.9: N_2 sorption at $77\,K$ of the cellulose aerogels prior to (sample Sol) and after silica modification (Sol1-Sol4).

To quantify the different compositions used for the modifications, TGA were measured (Figure 7.10). It can be seen, that the results are similar to that, obtained with the cotton linter derived materials. First, the mass loss, attributed to the evaporation of ethanol and traces of water, between 25 and $270\,^{\circ}C$ is present, and second, the degradation of the cellulosic network, starting at $270\,^{\circ}C$, determines the main weight loss. Further, it can be seen, that the residual masses for all samples are about $10\,\%$ higher than for the cotton linter samples. Thus, it can be concluded, that the silica uptake is much higher for the pre-hydrolysis kraft pulp alcogels. Sol1 exhibits the highest mass loss, $66\,\%$, and Sol3, corresponding to CL2, with $47\,\%$ the lowest. Further it is interesting to see, that the amount of silica remaining, directly correlates with the concentration. The mass loss of Sol2, half of the amount of

precursor and catalyst compared to Sol3 was used, is about 18 % higher than for Sol3, where a total mass loss of about 67 % could be observed. This result correlates with sample CL2 with a total mass loss of about 72 %.
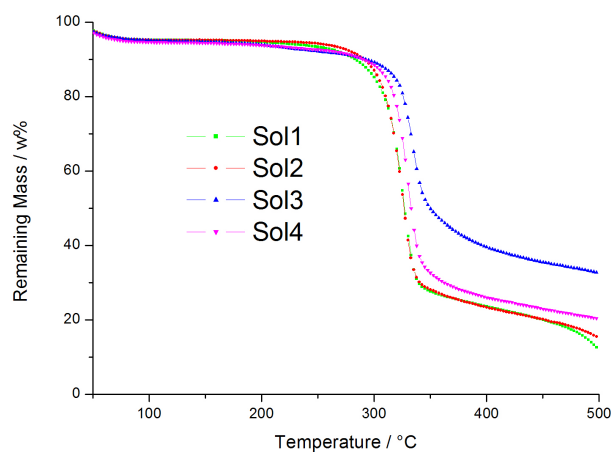
Figure 7.10: Thermogravimetric analyses of silica modified and scCO$_2$ dried hardwood pre-hydrolysis kraft pulp aerogels.

Looking at the SEM images recorded for samples Sol2, Sol3 and Sol4 (Figure 7.11 and 7.12), homogenous surfaces can be seen.
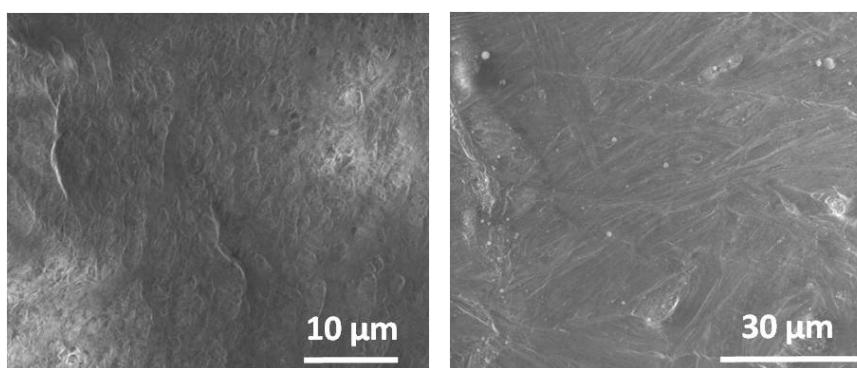
Figure 7.11: SEM pictures of hardwood pre-hydrolysis kraft pulp aerogels after silica modification (Sol2 (left) and Sol3 (right)).

Contrary to the cotton linters derived materials, the usage of hydrochloric acid as a catalyst did not lead to the formation of spherical objects on the surface. Only for Sol4 a slightly different morphology can be distinguished. This roughening of

the surface can be attributed to the usage of CPTMS.
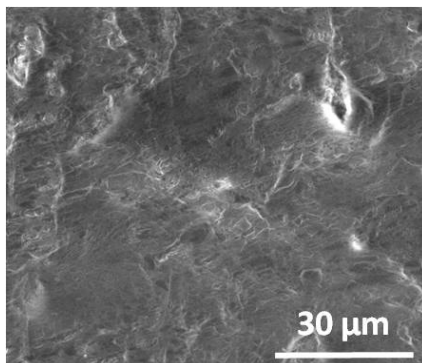
Figure 7.12: SEM picture of hardwood pre-hydrolysis kraft pulp aerogels after silica modification (Sol4).

Further EDX measurements were employed to verify the presence of silica on the surface (Figure 7.13 and 7.14). For all measured samples, Sol2, Sol3 and Sol4, carbon, oxygen and silicon signals are seen, where the first two elements derive from the cellulose itself. Again, the presence of the modification agents is confirmed through signals of silica and/or chlorine for Sol4.
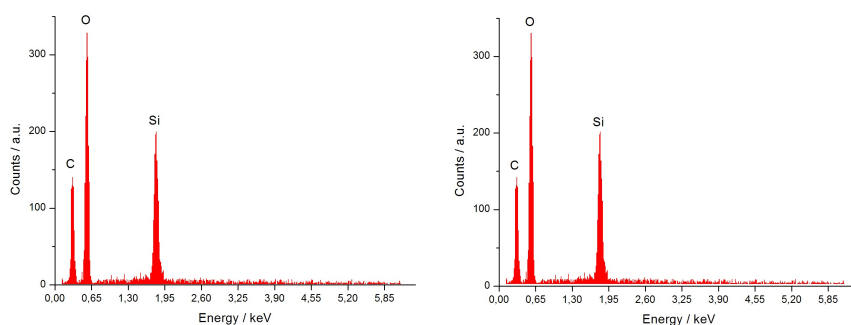
Figure 7.13: EDX of hardwood pre-hydrolysis kraft pulp aerogels after silica modification (Sol2 (left) and Sol3 (right)).
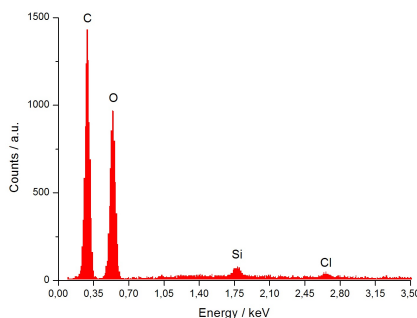
Figure 7.14: EDX of hardwood pre-hydrolysis kraft pulp aerogels after silica modification (Sol4).

7.4   Conclusion

Cylindrical cellulosic alcogels were modified with silica by means of sol-gel chemistry. Thereby, the alcogels were prepared from two different plant resources, cotton linters on the one hand and hardwood pre-hydrolysis kraft pulp on the other. To determine the optimal conditions to maintain the porous character of the cellulose networks, four different sols, for each different type of alcogel, were prepared to investigate the effects of different silica precursors, tetraethoxysilane and 3-chloropropyltrimethoxysilane, and/or the presence of an acidic catalyst, hydrochloric acid. After dyring the acogels with supercritical CO_2, aerogels high surface areas are obtained. To verify the success of the modification, TGA, nitrogen sorption, SEM, GPC and EDX measurements were employed.

In the case of the cotton linter samples, the use of an acidic-catalyst did not lead to the desired smooth surface, rather a "crust-like" morphology with spherical silica. Further, it could be seen, that, next to the average pore diameter, also the degree of polymerization of the sample significantly decreased. For the other samples the cellulose integrity and open-porous network structure of the cellulose aerogels were preserved. Through the usage of 3-chloropropyltrimethoxysilane as the only silica source the most satisfying results, concerning surface area, $265\,\mathrm{m^2 \cdot g^{-1}}$, and pore volume, $0.65\ \mathrm{cm^3 \cdot g^{-1}}$, were obtained. 3-Chloropropyltrimethoxysilane, in addition, is a suitable donor to introduce anchor groups for further functionalisation.

For the Sol samples a slightly different picture was found. Here, the use of hydrochloric acid did not lead to a change considering the surface area, sorbed volume and the average pore diameter. This could derive from the different preparation techniques of the cellulose. For this type, the hardwood pre-hydrolysis kraft pulp, the process itself involves very acidic components. Nevertheless it could also be shown, that the results obtained with cotton linter aerogels, can also be accomplished with different types of cellulose resources.

Chapter 8

Experimental Part

8.1 General Methods and Materials

All chemicals used for syntheses were obtained by commercial suppliers (Aldrich, Fluka, ABCR, Acros) and used as received. Solvents were purified by conventional purification methods and stored under argon over molecular sieve (3 or 4 Å). Dichloromethane, THF, Toluene and Methanol were dried by a commercial apparatus (PureSolv) comprising dynamic drying using molecular sieve. Manipulations under an inert atmosphere were carried out by standard Schlenk techniques.

8.2 Instrumentations

Atomic force microscopy (AFM) measurements were performed using a NanoMan V system from Veeco. For topographic measurements, PPP-NCHR cantilevers (Nano and More) were used in tapping mode. Tune parameters for the system were $0.5\,V$ target amplitude and the measurement frequency set to $5\,\%$ off-resonance. The measurement was performed at a damping of approximately $25\,\%$ and scan rates of $1\,Hz$ for 1x1 to 5x5 μm^2 images.

Dynamic light Scattering (DLS) measurements were carried out on an ALV/CGS-3 compact goniometer system, equipped with an ALV/LSE-5003 light scattering electronics and multiple τ digital correlator, and a $632.8\,nm$ JDSU laser 1145P. For the measurement the solid was dispersed in distilled water or dry ethanol. The run time of one measurement cycle was 10 seconds. Every size distribution curve was obtained by averaging 10 measurements.

Elemental analysis was carried out at the Microanalytical Laboratory at the University of Vienna.

Energy dispersive X-ray (EDX) spectroscopy was performed on a JEOL 5410 connected to an EDX detector RÖNTEC. The spectra were analysed with the Edax Genesis software. Before measurement the samples were coated with either gold or carbon.

Ellipsometric measurements were performed with the alpha-SE® system from J.A.Woolam Co, Inc, under an angle of 70°. Ellipsometric spectra between 380 and 900 nm wavelengths were recorded and fitted using a simple two layer model with silicon substrate and a layer with a refractive index of 1.45; which has been shown to yield suitable results for thin films.

Fourier transform infrared spectroscopic (FT-IR) measurements were performed on a Bruker Tensor 27 spectrometer under ambient atmosphere (32 scans at a resolution of $4 \, cm^{-1}$) equipped with an Interferometer RockSolid^{TM} and a DigiTect^{TM} detector system, high sensitivity DLATGS, using KBr disks for powder samples or an ATR unit (ZnSe crystal for liquids, diamond for powder samples). The spectra were processed by using the OPUS^{TM} software.

Lateral force microscopy (LFM) measurements were undertaken using a PPP-CONTR cantilever (Nano and more) with a spring constant of $0.179 \, N{\cdot}m^{-1}$. Approach was performed with a deflection setpoint of 1 V to ensure engaging of the system. After contact, the setpoint was changed to the value of interest, covering a range between 0.2 to 5 V (12-300 nN tip force). In-situ control of LFM induced surface modification was undertaken with the same tip at a deflection setpoint of 0.1 V (6 nN tip force). High resolution images of the modified surfaces were obtained in tapping mode as described above.

Nitrogen sorption measurements at 77 K were carried out on a Micromeritics ASAP 2020 or an ASAP 2010 instrument. The samples were degassed at least 5 hours at room temperature prior to measurement. The surface area and C_{bet} were calculated using the adsorption model by Brunauer, Emmet and Teller (BET) and the average pore diameter were evaluated by the Barrett, Joyner and Halenda (BJH) equation on the desorption branch of the isotherm.

Nuclear magnetic resonance (NMR) in liquid state for ^{1}H, ^{13}C and ^{31}P nucleus were recorded on a Bruker AVANCE 250 (^{1}H at 250.13 MHz, ^{13}C at 62.86 MHz, ^{31}P at 101.26 MHz) equipped with a 5 mm inverse-broadband probe head with a z-gradient unit. 2D-Experiments: ^{1}H/^{15}N - hetero nuclear multiple-bond correlation (HMBC) were measured with a long range coupling constant of 5 Hz respectively 10 Hz.

Solid state NMR spectra were recorded on a Bruker AVANCE 300 (^{13}C at 75.40 MHz, ^{11}B at 96.21 MHz, ^{31}P at 121.38 MHz and ^{15}N at 30.38 MHz) equipped with a 4 mm broadband MAS probe head. ^{13}C, ^{11}B, ^{31}P and ^{15}N spectra were recorded with ramped CP MAS experiments (Cross Polarization and Magic Angle Spinning). The sample holders were spun at 6 kHz for the ^{31}P, ^{15}N and ^{13}C experiments and at 10 kHz for the ^{11}B measurements.

Small-angle X-ray scattering (SAXS) was performed using a rotating anode generator equipped with a pinhole camera (Nanostar from Bruker AXS with Cu-K$_\alpha$ radiation from crossed Göbel mirrors). The X-ray patterns were recorded with an area detector (VANTEC 2000) and radially averaged to obtain the scattering intensity in dependence on the scattering vector $q = (4\pi/\lambda)sin\Theta$, with 2Θ being the scattering angle and $\lambda = 0.1542$ nm the X-ray wavelength.

Scanning electron microscopy (SEM) was performed on a JEOL-6400 instrument using a tungsten filament.

Transmission electron microscopy (TEM) measurements were prepared by dispersing the materials in ethanol prior to deposition on a carbon coated TEM Cu grid. TEM measurements were performed on a FEI TECNAI G20 (USTEM, Vienna University of Technology).

Thermogravimetric analyses (TGA) were performed on a Netzsch Iris TG 209 C with a 414 TASC controller in a platinum crucible with a heating rate of 10 K·min^{-1} under synthetic air.

Ultraviolet-visible (UV-Vis) spectroscopy measurements were carried out on a PerkinElmer Lambda 35 with scan speed of 480 nm·min^{-1} and a slit width of 1 nm.

X-ray photoelectron spectroscopy (XPS) measurements were carried out with a system from SPECS Surface Nano Analysis GmbH with a XR-1000 X-ray source and a PHOIBOS-3500 hemispherical analyser. The spectra were recorded using the Mg source. For overview scans (0-600 eV), a resolution of 0.1 eV and a dwell time of 0.1 s were chosen and the average of 3 scans was recorded. Peaks for the individual elements were recorded at 0.02 eV resolution averaging 5 scans.

X-ray diffraction (XRD) measurements were performed on a Philipps XPert diffractometer using the Cu-Kα radiation ($\lambda = 1.542$ Å), equipped with an XCelerator multi-channel detector, Bragg Brentano geometry, silicon single crystal sample holder. The diffraction pattern was recorded between 5 and 90° with 1 scan/step and a step size of 0.02°.

8.3 Synthesis of Silica Nanoparticle Networks

8.3.1 Synthesis of Silica Nanoparticles

In a 250 ml round bottom flask, 60 μl ammonia solution (32 %) and 1.98 g (110 mmol) water were added to 100 ml dry methanol. The solution was stirred for 5 minutes before adding drop-wise 10.41 g (500 mmol) TEOS. The final solution was stirred for three days at ambient temperature.

8.3.2 Surface Modification of Silica Nanoparticles

Synthesis of N-(Trimethoxysilylpropyl)imidazole

Synthesis of 3-Iodopropyltrimethoxysilane
Under argon atmosphere 36.9 g (0.246 mol) of sodium iodide were dissolved in 150 ml dry acetone and 48.9 g (0.246 mol) 3-chloropropyltrimethoxysilane were added drop-wise under stirring. The mixture was heated to reflux under stirring overnight. Afterwards, the formed precipitate (sodium chloride) was filtered off and the product distilled under vacuum (3 mbar at 80 °C). A yellowish liquid was obtained. Yield: 37.12 g (53 %, 127.92 mmol).

^{1}H NMR (250 MHz, CDCl$_3$): 0.69 (t, 2H, Si-CH2), 1.89 (q, 2H, I-CH2-CH2), 3.15 (t, 2H, I-CH2), 3.52 (s, 9H, Si-O-CH3) ppm.

Synthesis of N-(Trimethoxysilylpropyl)imidazole

Under argon atmosphere 2.9 g (0.120 mol) sodium hydride were suspended in 150 ml dry THF, the mixture was cooled to 4 °C with an ice bath and 8.2 g (0.120 mol) of imidazole were added over a period of 30 minutes. The suspension was stirred for 2 hours until no release of hydrogen was observed anymore. Then 26.12 g (0.090 mol) of 3-iodopropyltrimethoxysilane was added and the mixture was heated to reflux overnight. The orange suspension was filtered and the solvent removed under reduced pressure. Afterwards 150 ml dry dichloromethane was added and the formed white precipitate was filtered off. The product, a transparent liquid, was gained by distillation (1 mbar at 150 °C).
Yield: 11.6 g (55.7 %, 50.2 mmol).

^{1}H NMR (250 MHz, CDCl$_3$): 0.54 (t, 2H, Si-CH2), 1.83 (q, 2H, N-CH2-CH2), 3.53 (s, 9H, Si-O-CH3), 3.88 (t, 2H, N-CH2), 6.88 (s, 1H, N-CH-CH-N), 7.01 (s, 1H, N-CH-CH-N), 7.54 (s, 1H, N-CH-N) ppm.
^{13}C NMR (250 MHz, CDCl$_3$): 7.4 (Si- CH2), 25.1 (N-CH2-CH2), 55.7 (N-CH2), 56.2 (Si-O-CH3), 120.7 (N-CH-CH-N), 128.1 (N-CH-CH-N), 136.8 (N-CH-N) ppm.

Surface Modification of Silica Nanoparticles

16 ml of the previously prepared silica nanoparticles suspension were transferred into a Schlenk tube and degassed in vacuum several minutes to remove excessive ammonia. Either 1.42 g (7.147 mmol) of 3-chloropropyltrimethoxysilane, or 1.65 g (7.147 mmol) of *N*-(trimethoxysilylpropyl)imidazole were added drop-wise. The solution was stirred under argon, at room temperature overnight.

8.3.3 Synthesis of Silica Nanoparticle Networks

The synthesis was carried out under argon atmosphere. 5 ml suspension of silica nanoparticles modified with *N*-(trimethoxysilylpropyl)imidazole and 5 ml suspension of silica nanoparticles modified with 3-chloropropyltrimethoxysilane were introduced in a 50 ml round bottom flask. Additionally 10 ml of dry methanol were added. The solution was refluxed over 2 days and finally the solvent removed under vacuum (3 mbar). A white powder was obtained, which was washed with acetone, ethanol and water, 20 ml respectively.

8.4   Variation of the Metal Oxide Nanoparticles

8.4.1   Synthesis of Metal Oxide Nanoparticles

Titania Nanoparticles

10 ml (33.96 mmol) of $Ti(O^iPr)_4$ were dissolved in 25 ml dry ethanol. This mixture was added drop-wise under vigorous stirring to 250 ml water, adjusted to a pH of 1.7 with nitric acid. During the addition the final reaction mixture was cooled to 4 °C using an ice bath. After complete addition the ice bath was removed and the mixture was stirred for 3 days at room temperature. Afterwards the solvent was removed under reduced pressure and the white, crystalline product was dried in a desiccator over P_2O_5 under vacuum.

Zirconia Nanoparticles

20 ml of an aqueous 4 molar solution of $ZrOCl_2 \cdot 8H_2O$ (80 mmol) were heated to 200 °C for 72 hours in a stainless-steel autoclave with a PTFE inlay. The particles were collected through precipitation with acetone and centrifugation at 8000 rpm. Afterwards the nanoparticles were washed 3 times with ethanol and acetone, 20 ml respectively. Finally the crystalline, white powder was dried in a dessicator over P_2O_5 under vacuum.

Iron Oxide Nanoparticles

Iron oxide, Fe_3O_4, nanoparticles were prepared through a coprecipitation method. Therefore, 10.53 g (38.97 mmol) of $FeCl_3 \cdot 6H_2O$ and 4.28 g (21.51 mmol) of $FeCl_2 \cdot 4H_2O$ were dissolved in 80 ml distilled water. Afterwards the yellow solution was heated to 70 °C and 40 ml of a 25 % aqueous $N(CH_3)_4OH$ solution were added drop-wise. A black precipitate could be observed after some minutes. Upon complete addition the mixture was stirred for additional 2 hours. Then, the mixture was allow to cool to room temperature and the precipitate was collected through magnetic decantation. Finally, the black particles were washed three times with ethanol. 20 ml respectively, and dried in a dessicator over P_2O_5 under vacuum.

8.4.2   Surface Modification of Metal Oxide Nanoparticles

Synthesis of 3-Chloropropylphosphonic acid

Synthesis of Dimethyl-3-chloropropylphosphonate
18 g (160.41 mmol) potassium tert-butoxide were suspended in 150 ml THF. Afterwards 22.01 g (200 mmol) dimethylphosphite were slowly added under vigorous stirring. After 2 hours of stirring the whole suspension was slowly added to a stirred suspension of 47.23 g (300 mmol) 1-bromo-3-chloropropane in 120 ml THF in a 500 ml round bottom flask. A white suspension was formed immediately. The mixture was heated to reflux for 20 minutes. After cooling to room temperature the formed precipitate, potassium bromide, was filtered off and washed twice with 100 ml diethylether. Then the solvents and by-products were removed under vacuum (20 mbar at 170 °C). A slightly colored liquid was obtained.
Yield: 17.9 g (60 %, 96.25 mmol).

^{1}H NMR (250 MHz, CDCl$_3$): 1.82-1.92 (m, 2H, P-CH2-CH2), 1.93-2.10 (m, 2H, P-CH2), 3.58 (t, 2H, Cl-CH2), 3.72 (d, 6H, P-O-CH3) ppm.
^{31}P NMR (250 MHz, CDCl$_3$): 45.99 ppm.

Synthesis of 3-Chloropropylphosphonic Acid
6.169 g (33.07 mmol) dimethyl-3-chloropropylphosphonate were mixed with 40 ml hydrochloric acid (37 %) and heated to reflux for 24 hours. Afterwards the solvent was removed under reduced pressure and residues of water were removed through azeotropic distillation by adding 20 ml of toluene. The yellowish liquid residue was crystallized from 50 ml chloroform and filtered. The colorless crystalline product was dried in a desiccator over P$_2$O$_5$ under vacuum.
Yield: 3.73 g (70 %, 23.53 mmol).

^{1}H NMR (250 MHz, DMSO-*d6*): 1.63-1.69 (m, 2H, P-CH2-CH2), 1.83-1.90 (m, 2H, P-CH2), 3.67 (t, 2H, Cl-CH2), 7.29 (s, 2H, P-OH) ppm.
^{31}P NMR (250 MHz, DMSO-*d6*): 37.85 ppm.
^{13}C-NMR (DMSO-*d6*): 24.2 (P-CH2-CH2), 26.4 (P-CH2), 46.1 (Cl-CH2) ppm.

Synthesis of *N*-Imidazolylpropyl Phosphonic Acid

Synthesis of Diethyl-2-bromoethylphosphonate
18 g (105.3 mmol) triethylphosphite and 36 g (412.2 mmol) 1,2-dibromoethane were heated under vigorous stirring to 160 °C for 30 minutes. Unreacted 1,2-dibromoethane

was removed under reduced pressure and diethyl-2-bromoethylphosphonate distilled under vacuum (2 mbar at 165 °C). A colorless liquid was obtained.
Yield: 23 g (88 %, 92.7 mmol).

^{1}H NMR (250 MHz, CDCl$_3$): 1.23 (t, 6H, P-O-CH2-CH3), 2.28 (m, 2H, P-CH2), 3.43 (m, 2H, Br-CH2), 4.02 (m, 4H, P-O-CH2) ppm.
^{31}P NMR (250 MHz, CDCl$_3$): 37.6 ppm.
^{13}C NMR (250 MHz, CDCl$_3$): 16.3 (P-O-CH2-CH3), 23.6 (Br-CH2), 30.6 (P-CH2), 61.9 (P-O-CH2) ppm.

Synthesis of Diethyl-3-bromopropylphosphonate

30 g (180.55 mmol) triethylphosphite and 150 g (722.20 mmol) 1,3-dibromopropane were heated under vigorous stirring to 160 °C for 30 minutes. Unreacted 1,3-dibromopropane was removed under reduced pressure and diethyl-3-bromopropylphosphonate distilled under vacuum (2 mbar at 165 °C). A colorless liquid was obtained.
Yield: 23.45 g (50 %, 90.5 mmol).

^{1}H NMR (250 MHz, CDCl$_3$): 1.20 (t, 6H, P-O-CH2-CH3), 1.80 (m, 2H, P-CH2-CH2), 1.99 (m, 2H, Br-CH2), 3.35 (t, 2H, P-CH2), 3.97 (m, 4H, P-O-CH2) ppm.
^{31}P NMR (250 MHz, CDCl$_3$): 30.4 ppm.
^{13}C NMR (250 MHz, CDCl$_3$): 16.3 (P-O-CH2-CH3), 23.1 (P-CH2-CH2), 25.8 (P-CH2), 33.5 (Br-CH2), 61.5 (P-O-CH2-CH3) ppm.

Synthesis of Sodium Imidazolide

Under argon 1,2 g (50 mmol) of sodiumhydride were suspended in 150 ml dry THF. This suspension was cooled to 4 °C with an ice bath and 3.404 g (50 mmol) imidazole were added over a period of 10 minutes. The suspension was further stirred for 2 hours until no evolution of hydrogen was visible. Afterwards the white product was filtered off and dried in a desiccator over P$_2$O$_5$ under vacuum.
Yield: 4.41 g (98 %, 49 mmol).

Synthesis of Dimethyl-N-imidazolpropylphosphonate

Under argon, in an 25 ml round bottom flask, 0.9 g (10 mmol) of sodium imidazolide were dissolved in 5 ml dry DMF. The solution was cooled to 4°C with an ice bath and 2.59 g (10 mmol) diethyl-3-bromopropylphosphonate were added at once. Afterwards the ice bath was removed and the suspension was heated to 55 °C for 8 hours under vigorous stirring. The solvent was removed under reduced pressure

at 40 °C. The liquid residue was extracted with chloroform and water, 3 times, with 10 ml respectively. The collected organic phases were dried over $MgSO_4$ and the solvent evaporated under vacuum. A colorless liquid was obtained.
Yield: 0.78 g (26 %, 3.16 mmol).

^{1}H NMR (250 MHz, CDCl$_3$): 1.26 (t, 6H, P-O-CH2-CH3), 1.61 (m, 2H, P-CH2-CH2), 1.99 (m, 2H, P-CH2-CH2-CH2), 3.98 (m, 4H, P-CH2, P-O-CH2), 6.91 (d, 2H, N-CH-CH-N), 7.43 (s, 1H, N-CH-N) ppm.
^{31}P NMR (250 MHz, CDCl$_3$): 30.21 ppm.
^{13}C NMR (250 MHz, CDCl$_3$): 16.3 (P-O-CH2-CH3), 21.1 (P-CH2-CH2), 24.4 (P-CH2), 46.7 (N-CH2), 61.7 (P-O-CH2-CH3), 118.7 (N-CH-CH-N), 129.5 (N-CH-CH-N), 137.1 (N-CH-N) ppm.

Synthesis of N-Imidazolylpropylphosphonic Acid
Under argon, in a 10 ml round bottom flask, 0.43 g (1.75 mmol) of dimethyl-*N*-imidazolpropylphosphonate were dissolved in 5 ml dry dichloromethane and stirred for 5 minutes. Afterwards 0.80 g (5.24 mmol) bromotrimethylsilane were added and stirred for 24 hours. Then the solvent was removed under reduced pressure and the brownish viscous liquid dissolved in 5 ml dry methanol. Afterwards the excessive methanol was removed under reduced pressure. A viscous brown liquid was obtained. Yield: 0.213 g (64 %, 1.12 mmol).

^{1}H NMR (250 MHz, D$_2$O): 1.58 (m, 2H, P-CH2-CH2), 1.98 (m, 2H, P-CH2-CH2-CH2), 4.20 (t, 2H, P-CH2), 7.38 (d, 2H, P-CH2, N-CH-CH-N), 8.63 (s, 1H, N-CH-N) ppm.
^{31}P NMR (250 MHz, D$_2$O): 27.19 ppm.
^{13}C NMR (250 MHz, D$_2$O): 22.2 (P-CH2-CH2), 24.3 (P-CH2), 49.4 (N-CH2), 119.8 (N-CH-CH-N), 121.9 (N-CH-CH-N), 135.5 (N-CH-N) ppm.

Surface Modification of Titania Nanoparticles

1 g of previously synthesised TiO_2 nanoparticles were dispersed in 50 ml water. To this suspension either 0.244 g (1.54 mmol) of 3-chloropropylphosphonic acid, or 0.293 g (1.54 mmol) of *N*-imidazolylpropyl phosphonic acid, dissolved in 100 ml distilled water, respectively, were added. The white suspensions were stirred at room temperature for 24 hours. The modified particles were isolated via centrifugation, washed several times with ethanol and water and finally dried in a desiccator over P_2O_5 under vacuum. The chloro modified titania nanoparticles will be referred to

as TiO_2_Cl, whereas the imidazole modified will be written as TiO_2_Im.

Surface Modification of Zirconia Nanoparticles

1 g of previously synthesised ZrO_2 nanoparticles were dispersed in 50 ml water. To this suspension either 0.159 g (1 mmol) of 3-chloropropylphosphonic acid, or 0.190 g (1 mmol) of N-imidazolylpropyl phosphonic acid, dissolved in 50 ml distilled water, respectively, were added. The white suspensions were stirred at room temperature for 24 hours. The modified particles were isolated via centrifugation, washed several times with ethanol, acetone and water and finally dried in a desiccator over P_2O_5 under vacuum.

Surface Modification of Iron Oxide Nanoparticles

50 mg of previously synthesised Fe_3O_4 nanoparticles were suspended through ultrasonication in 50 ml toluene. To this suspension either 40 mg (0.25 mmol) of 3-chloropropylphosphonic acid, or 48 mg (0.25 mmol) of N-imidazolylpropyl phosphonic acid were added. The brown suspensions were placed in an ultrasonic bath at room temperature for 150 minutes. The modified particles were isolated via magnetic decantation, washed several times with ethanol, acetone and water and finally dried in a desiccator over P_2O_5 under vacuum.

8.4.3   Synthesis of Titania Nanoparticle Networks

75 ml of the modified particles suspensions, TiO_2_Cl and TiO_2_Im, described above, were transferred into a 250 ml round bottom flask and refluxed for 24 hours. Afterwards the connected particles were centrifuged, washed two times with ethanol and finally dried in a desiccator over P_2O_5 under vacuum.

8.4.4   Photocatalytic Reactions

In a snapcap vessel 5 mg of the sample (TiO_2 or linked TiO_2 nanoparticles) were dispersed in 18 ml deionised water. Afterwards the pH of the suspensions was adjusted to 4 with NaOH and HCl. Then 2 ml of a 200 μM aqueous methylene blue solution were added. The vessels were then placed in a UV-light box (Sylvania UVA-BLB Lynx S, irradiance ranges from 1.5 to 2.2 mW·cm^{-2}) and magnetically stirred for 1 hour in the dark. To investigate the photocatalytic degradation of the samples,

3 ml of the suspensions were taken after 0, 10, 20, 40, 160 and 320 minutes respectively of irradiation, centrifuged and measured through UV/Vis spectroscopy.

8.5   Variation of the Linking Unit

Introduction of Xylene as Linking Unit

In a 100 ml round bottom flask, 1.88 g (10.7 mmol) of 1,4-bis(chloromethyl)benzene were added at once to 48 ml of a methanol suspension of silica nanoparticles modified by the means of 4.95 ml (21.5 mmol) N-(trimethoxysilylpropyl)imidazole. Afterwards additional 20 ml of dry methanol were added. The solution was heated to reflux for 24 hours. The solvent was then removed under reduced pressure (3 mbar) and the product was washed twice with respectively 20 ml deionised water and ethanol and dried in a desiccator over P_2O_5. A white powder was obtained.

Introduction of Hexyl as Linking Unit

In a 25 ml round bottom flask 0.52 g (4.1 mmol) of 1,6-dichlorohexane were added to a 9 ml suspension of imidazole modified silica nanoparticles suspension. The solution was stirred 24 hours at room temperature. The solvent was then removed under reduced pressure (3 mbar) and the crude product was washed twice with respectively 20 ml deionised water and ethanol and dried in a desiccator over P_2O_5. A brownish powder was obtained.

8.6   Variation of the Anion

8.6.1   Variation of the Anion of Systems Containing One Imidazolium Unit

In a snapcap vessel 0.25 g of previously obtained silica nanoparticle network containing one imidazolium unit, were dispersed in 20 ml acetone. Afterwards 0.25 g of either $NaBF_4$, KPF_6, or $LiT_{f2}N$ were added at once. The dispersions were stirred 24 hours at room temperature. Then, the products were centrifuged and washed twice with deionised water and ethanol, 20 ml respectively. The reaction solvent and washing phases were combined and evaporated under vacuum. The salts obtained after evaporation, NaCl, KCl, or LiCl, were isolated for further analyses to monitor the exchange ratio.

The obtained products were dried 24 hours under vacuum at 90 °C.

8.6.2 Variation of the Anion of Systems Containing Two Imidazolium Units

For the systems containing two imidazolium units, the same procedure, salts and amount were used as for the systems with one imidazolium unit.

8.7 Synthesis of Silica/Silver Nanoparticle Systems

8.7.1 Synthesis of N-Methylimidazolium Mercaptopropionate

In a 10 ml snapcacp vessel, 1 g (12.18 mmol) of N-methylimidazole were mixed with 1.290 g (12.18 mmol) 3-mercaptopropionic acid. By addition an exothermic reaction could be observed. The transparent solution was stirred overnight.
Yield: 2.28 g (99 %, 12.1 mmol).

^{1}H NMR (250 MHz, CDCl$_3$): 2.59 (t, 2H, HS-CH2), 2.70 (t, 2H, HS-CH2-CH2), 3.68 (s, 3H, N-CH3), 7.11 (d, 2H, N-CH2-CH2-N), 7.27 (s, 1H, SH), 7.95 (s, 1H, N-CH-N), 11.95 (s, 1H, N-H) ppm.

8.7.2 Modification of Silica Nanoparticles with N-(Trimethoxy-silylpropyl)imidazole and 3-Mercaptopropionic Acid

60 ml of a previously prepared silica nanoparticle suspension, obtained by reacting 15 mmol of TEOS, were transferred into a 250 ml round bottom flask and degassed in vacuum several minutes to remove excessive ammonia. Afterwards 1.152 g (5 mmol) of N-(trimethoxysilylpropyl)imidazole were added drop-wise. The solution was stirred under argon, at room temperature overnight. Afterwards 0.531 g (5 mmol) of 3-mercaptopropionic acid were added (imidazole : thiol = 1:1). The solution was stirred overnight. For analyses the solvent was removed in vacuum (3 mbar), and the product was washed two times with water, acetone and ethanol, 20 ml respectively. Finally the white powder was dried in a desiccator over P$_2$O$_5$.

8.7.3   Synthesis of Silica/Silver Nanoparticle Systems

20 ml of the above prepared solution of thio-imidazole functionalized silica nanoparticles, 1.032 g (6.1 mmol) dispersed in 50 ml water were added (thiol-imidazole : Ag^+ = 1:4). A white suspension was formed immediately. Afterwards 0.252 g (6.1 mmol) sodium borohydride dissolved in 25 ml water was added within some seconds. Under a violent reaction a black precipitate was formed immediately. The suspension was allowed to stir overnight at ambient temperature. Afterwards the product was gained by centrifugation and washing two times with ethanol, water and acetone respectively. Finally the black powder was dried under reduced pressure (2 mbar) at 80 °C.

8.8   Assembly of Mono- and Multilayers of Metal Oxide Nanoparticles on Silicon Surfaces

8.8.1   Modification of Silicon Wafers

Silicon wafers with a native oxide layer were cut into small pieces (about 0.5 x 1 cm^2), washed, and activated using UV/ozone treatment. These substrates were immersed into a 100 mmolar solution of N-(trimethoxysilylpropyl)imidazole in ethanol for varying times. Cleaning of the samples was performed by sonicating at low power for 1 minute in dry isopropanol and subsequent blow-drying of the substrates.

8.8.2   Deposition of Titania Nanoparticles onto Silicon Wafers

Deposition of the titania nanoparticles onto the, with N-(trimethoxysilylpropyl)-imidazole modified, silicon wafers was undertaken by immersion of the slides into a 0.01 mg·ml^{-1} suspension of titania nanoparticles capped with 3-chloropropylphosphonic acid in ethanol for 21 hours, followed by the same cleaning procedure used for the first step (sonication in isopropanol and blow-drying).

8.8.3   Deposition of Multilayers of Titania Nanoparticles onto Silicon Wafers

For the formation of multilayers of nanoparticles, silica substrates containing a monolayer of titania nanoparticles were immersed into the linker, N-(trimethoxysilylpropyl)imidazole or N-imidazolylpropyl phosphonic acid, and titania nanoparticles

functionalised with 3-chloropropylphosphonic acid, suspensions repeatedly.

8.9 Preparation of Silica Modified Cellulosic Aerogels

8.9.1 Preparation of Cellulosic Alcogels

Shaped cellulose alcogels were prepared from solutions of 3 w% cotton linters, or hardwood pre-hydrolysis Kraft pulp in N-methylmorpholine-N-oxide monohydrate as described by Liebner *et al.*.[203]

8.9.2 Silica Modification of Cellulosic Alcogels

Silica modication of those alcogels was carried out in snap-cap vessels, equipped with a magnetic stirrer, containing the desired amount of TEOS, 3-chloropropyltri-methoxysilane, hydrochloric acid (0.12 N) and ethanol, in order to reach a total volume of 10 ml (Table 7.1 and 7.2). The silanisation mixtures were stirred at about 50 rpm for 24 hours. Subsequently, the samples were washed thoroughly with ethanol before they were subjected to supercritical carbon dioxide drying (scCO$_2$).

8.9.3 Supercritical Drying of Cellulosic Alcogels

The drying step was performed in a laboratory-scale autoclave (Alltech Grom GmbH, Germany) at 40 °C (LC4 controller, Julabo Labortechnik GmbH). The modified cellulose aerogel was placed on a stainless steel filter panel inside the autoclave. After equilibrating the closed autoclave at 40 °C for 15 minutes, the system was pressurised over the bottom valve with liquid, pre-heated CO$_2$ using a HPLCpump (miniPump, TSP Thermal Separation Products, USA) until a final pressure of 100 bar was reached. This state was maintained for 15 minutes before the top valve was opened. The bottom valve was subsequently switched to the separator, where ethanol and CO$_2$ were separated by an isothermal flash. In a first step, the ethanol-rich phase was flushed out if the autoclave. Then, ethanol was drained from the gel pores at constant CO$_2$ flow rate of 1 g·min^{-1}. After 60 minutes, the top valve was closed and the autoclave was depressurised over the separator.

Chapter 9

Summary

The primary goal of this work was to synthesise new hybrid inorganic-organic materials based on metal or metal oxide nanoparticles and imidazolium containing ionic connectors. Thereby, the influences of the different components were investigated in respect of the properties of the final material. Furthermore, the processing of the resulting nanoparticle networks was investigated through deposition on silicon substrates.

9.1 Silica Nanoparticle Networks

A facile approach for the synthesis of silica nanoparticles networks was found. Thereby the approach can be divided into three subsequent steps. In the first step an approrpiate approach was found to synthesise silica nanoparticles with sizes of 15 nm, determined through DLS and TEM measurements. The second step was the surface functionalisation of these nanoparticles with trialkoxysilanes, bearing either an imidazole or a chloride functionality. The last step, the nucleophilic substitution reaction between these two moieties, resulted in covalently connected silica nanoparticles (Figure 9.1). Nitrogen solid state NMR measurements showed, that a majority, but not every imidazole unit undergoes a bridging reaction. Nevertheless, SAXS measurements and the corresponding mathematical fitting of the data, exhibit short-range ordering within the silica nanoparticle networks. Furthermore, $\pi - \pi$ stacking phenomenons between the imidazolium entities can be observed.
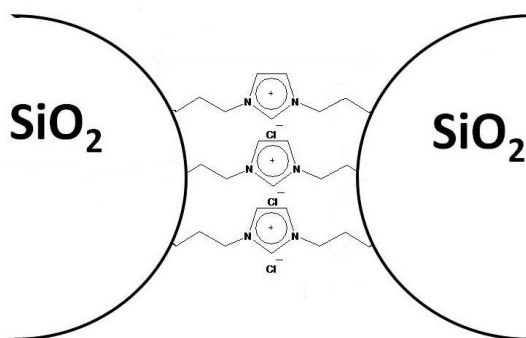
Figure 9.1: Silica nanoparticles bridged through imidazolium moieties.

9.2   Alteration of the Networks

In order to investigate the influence of the nanoparticles, linking unit and counter anions on the properties of the hybrid material, these components were varied or exchanged. For the nanoparticles, different metal oxide nanoparticles, TiO_2, ZrO_2 and Fe_3O_4 were synthesised using various routes; hydrothermal synthesis, precipitation or sol-gel process. The functionalisation of these nanoparticles was carried out either with trialkoxysilanes or phosphonic acids. The bonding was followed through FTIR measurements. Through TGA the surface coverage could be calculated, which was for all cases in acceptable ranges, from about 1.9 to 2.6 ligands per nm^2, which is for all cases about 60 % of a complete monolayer. Further, networks constructed from titania nanoparticles revealed an inter-particle porosities, with cavities of an average diameter of 2 nm and a total specific surface area of $205\,m^2 \cdot g^{-1}$. Through UV-Vis measurements the accessibility of the surface of the anatase nanoparticles was proven through the photocatalytical degradation of methylene blue. Further, SAXS investigations suggest an arrangement of the material with three structural levels, with first the titania clusters building up nanoparticles, second the nanoparticles and third a weak assembly of large domains of nanoparticles.

Extending the investigation to diimidazolium bridged silica nanoparticle systems, it could be found, that with increasing length of the bridging unit, the flexibility of the ligand has also to be considered as playing an important role. For ligands with a high flexibility, e.g. a hexyl chain between two imidazolium groups, the order of the particles within the network became weaker, as evidenced through SAXS. Contrary to this, if a xylene unit was introduced instead of the alkane part, the rigidity was enhanced, leading to higher packing factors.

For the variation of the anion, different salts were used, NaBF$_4$, KPF$_6$ and LiT$_{f2}$N, to exchange the chloride anions from systems containing one or two imidazolium units. To qualify and quantify the exchange ratio, XRD and solid state NMR measurements were employed as indirect and direct methods. Through elemental analyses measurements, it could be seen, that the metathesis yields decreased with increasing molar weight of the introduced anions. Interestingly, the anion metathesis on those compounds, even if not fully completed, allows to tailor the hydrophily / hydrophoby of the considered hybrid material.

9.3 Silica/Silver Nanoparticle Systems

Additionally to the second part, systems containing silica and silver nanoparticles reciprocally were synthesised. Imidazole functionalised silica nanoparticles were treated with 3-mercaptopropionic acid. Thereby, the imidazole moiety was converted to the protonated form, imidazolium, and thiol groups were present as anchor groups for silver nanoparticles. These particles were synthesised through the reduction of silver ions with sodium borohydride, and yielded metallic silver nanoparticles with sizes around 15 nm, evidenced through DLS, XRD and UV-Vis. Thereby, XRD measurements showed a mesoscopic arrangement of the imidazolium units.

9.4 Processing of Nanoparticle Networks

In the third part the fabrication of three-dimensional nanoparticle scaffolds with control over the lateral dimensions and the number of nanoparticle layers was demonstrated. The starting point for this synthesis presented the immersion of silicon wafers into a solution of N-(trimethoxysilylpropyl)imidazole. It could be shown, that a full monolayer could be achieved after 30 minutes. Afterwards the wafers were dipped into a suspension of chloride functionalised titania nanoparticles, resulting in covalent bonding to the surface (Figure 9.2). These sol-gel derived nanoparticles possessed a diamter of about 4 nm. Through various deposition times, it was found, that after 10 hours a fully covered surface was received.

Through tests with pre-patterned silicon surfaces, it was demonstrated, that the deposition of the nanoparticles proceeds selectively. AFM measurements showed structured layers of titania nanoparticles. Moreover, this approach could be extended to multilayers, by repeating the immersion steps. Thereby, the individual

heights of the layers increased significantly, particularly for the third layer of titania nanoparticles, mainly due to the higher specific surface of the underlying layers of particles.

LFM measurements showed high stabilities of these nanoparticle layers against shearing forces, up to about 36 nN. Further, these hybrid organic-inorganic layers can be converted to purely inorganic layers via photocatalytic oxidation utilising the optical properties of the titania nanoparticles.
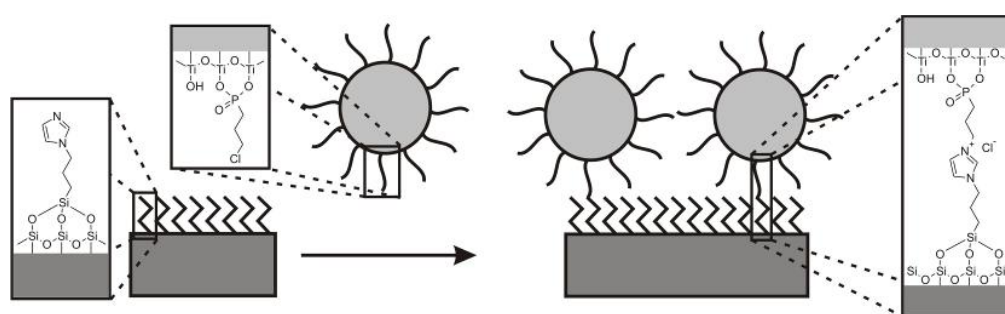
Figure 9.2: Process for the formation of a nanoparticle monolayer.

9.5   Surface Modification of Cellulosic Aerogels

Cellulose aerogels are highly interesting materials due to their low weight on the one hand, while maintaining high surface areas on the other hand. Through sol-gel reactions either cotton linter or pre-hydolisis kraft pulp alcogels were surface functionalised using two different kind of silicon sources, tetraethoxysilane and 3-chloropropyltrimethoxysilane, prior to supercritical drying. Different compositions of silica precursor, solvent, water and catalyst were investigated.
Through nitrogen sorption measurements at 77 K it could be shown, that in most cases the porous character of the aerogels was preserved. For the cotton linter derived materials, the usage of an acidic catalyst led to the disadvantage of the formation of a "crust" on the surface, as investigated through SEM. As a result a decrease of the overall porevolume of about 15 % can be seen through nitrogen sorption measurements. Contrary to this the pore system of pre-hydrolysis kraft pulp as the cellulose source was not affected through the utilisation of a catalyst.

Bibliography

1 Sanchez, C.; Julian, B.; Belleville, P.; Popall, M. *Journal of Materials Chemistry* **2005**, *15*, 3559–3592.

2 Kickelbick, G., Ed. *Hybrid Materials*; Wiley-VCH, Weinheim, 2006.

3 Ajayan, P. M.; Schadler, L. S.; Braun, P. V. *Nanocomposite Science and Technology*; Wiley-VCH, Weinheim, 2003.

4 Schubert, U.; Hüsing, N. *Synthesis of Inorganic Materials*, 2nd ed.; Wiley-VCH, Weinheim, 2005.

5 Roduner, E. *Chemical Society Reviews* **2006**, *35*, 583–592.

6 Crick, C. R.; Parkin, I. P. *Chemistry - A European Journal* **2010**, *16*, 3568–3588.

7 Allsopp, R. E., W. J.and Van Doren *American Paint Journal* **1972**, *57*, 66–9.

8 Lee, C. Y.; Hupp, J. T. *Langmuir* **2010**, *26*, 3760–3765.

9 Farokhzad, O. C.; Langer, R. *ACS Nano* **2009**, *3*, 16–20.

10 Park, Y.-S.; Liz-Marzan, L. M.; Kasuya, A.; Kobayashi, Y.; Nagao, D.; Konno, M.; Mamykin, S.; Dmytruk, A.; Takeda, M.; Ohuchi, N. *Journal of Nanoscience and Nanotechnology* **2006**, *6*, 3503–3506.

11 Ghosh, P.; Han, G.; De, M.; Kim, C. K.; Rotello, V. M. *Advanced Drug Delivery Reviews* **2008**, *60*, 1307 – 1315.

12 Liu, R.; Rallo, R.; George, S.; Ji, Z.; Nair, S.; Nel, A. E.; Cohen, Y. *Small* **2011**, *7*, 1118–1126.

13 Donthu, S.; Sun, T.; Dravid, V. *Advanced Materials* **2007**, *19*, 125–128.

14 Zhong, Z.; Halilovic, A.; Muhlberger, M.; Schaffler, F.; Bauer, G. *Applied Physics Letters* **2003**, *82*, 445–447.

15 Giri, P. K.; Bhattacharyya, S.; Singh, D. K.; Kesavamoorthy, R.; Panigrahi, B. K.; Nair, K. G. M. *Journal of Applied Physics* **2007**, *102*, 093515.

16 Dabhade, V.; Mohan, T. R.; Ramakrishnan, P. *Powder Technology* **2007**, *171*, 177 – 183.

17 Murase, Y.; Kato, E. *Journal of the American Ceramic Society* **2001**, *84*, 2705–2706.

18 Qu, S.; Yang, H.; Ren, D.; Kan, S.; Zou, G.; Li, D.; Li, M. *Journal of Colloid and Interface Science* **1999**, *215*, 190 – 192.

19 Niederberger, M.; Pinna, N. *Metal Oxide Nanoparticles in Organic Solvents*; Springer London, 2009; Chapter Aqueous and Nonaqueous Sol-Gel Chemistry.

20 Brinker, C. J.; Scherer, G. W. *Sol-Gel Science: The Physics and Chemistry of Sol-Gel Processing.*; Academic Press, 1990.

21 Livage, J.; Sanchez, C. *Journal of Non-Crystalline Solids* **1992**, *145*, 11 – 19.

22 Livage, J.; Henry, M.; Sanchez, C. *Progress in Solid State Chemistry* **1988**, *18*, 259 – 341.

23 Garnweitner, G.; Niederberger, M. *Journal of the American Ceramic Society* **2006**, *89*, 1801–1808.

24 Djerdj, I.; Arčon, D.; Jagličić, Z.; Niederberger, M. *Journal of Solid State Chemistry* **2008**, *181*, 1571 – 1581.

25 Niederberger, M. *Accounts of Chemical Research* **2007**, *40*, 793–800.

26 Yonezawa, T.; Sutoh, M.; Kunitake, T. *Chemistry Letters* **1997**, *26*, 619–620.

27 Doty, R. C.; Tshikhudo, T. R.; Brust, M.; Fernig, D. G. *Chemistry of Materials* **2005**, *17*, 4630–4635.

28 Kang, Y.-O.; Choi, S.-H.; Gopalan, A.; Lee, K.-P.; Kang, H.-D.; Song, Y. S. *Journal of Non-Crystalline Solids* **2006**, *352*, 463 – 468.

29 Kim, K.-S.; Demberelnyamba, D.; Lee, H. *Langmuir* **2004**, *20*, 556–560.

30 Faraday, M. *Philosophical Transactions of the Royal Society of London* **1857**, *147*, 145–181.

31 Malenovska, M.; Neouze, M.-A.; Schubert, U.; Peled, A.; Lellouche, J.-P. *Dalton Trans.* **2008**, 4647–4651.

32 Neouze, M.-A.; Malenovska, M.; Peterlik, H. *Polyhedron* **2010**, *29*, 569 – 573.

33 Turkevich, J. *Gold Bulletin* **1985**, *18*, 86–91.

34 Turkevich, J.; Stevenson, P. C.; Hillier, J. *Discussions of the Faraday Society* **1951**, *11*, 55–75.

35 Frens, G. *Nature Physical Science* **1973**, *241*, 20–22.

36 Brust, M.; Walker, M.; Bethell, D.; Schiffrin, D. J.; Whyman, R. *Chemical Communications* **1994**, 801–802.

37 Martin, M. N.; Basham, J. I.; Chando, P.; Eah, S.-K. *Langmuir* **2010**, *26*, 7410–7417.

38 Pukánszky, B.; Fekete, E. In *Mineral Fillers in Thermoplastics I*; Jancar, J., Fekete, E., Hornsby, P., Jancar, J., Pukánszky, B., Rothon, R., Eds.; Advances in Polymer Science; Springer Berlin / Heidelberg, 1999; Vol. 139; pp 109–153.

39 Kickelbick, G.; Schubert, U. In *Synthesis, Functionalization and Surface Treatment of Nanoparticles*; Baraton, M.-I., Ed.; American Scientific Publishers, Stevenson Ranch, CA, USA, 2003; Chapter Organic Functionalization of Metal Oxide Nanoparticles.

40 Grancharov, S. G.; Zeng, H.; Sun, S.; Wang, S. X.; O'Brien, S.; Murray, C. B.; Kirtley, J. R.; Held, G. A. *The Journal of Physical Chemistry B* **2005**, *109*, 13030–13035.

41 Lomoschitz, C. J. Synthesis of Phosphorus Coupling Agents and Their Use in the Modification of ZrO2 and Barium-Glass Surfaces. Ph.D. thesis, Vienna University of Technology, 2011.

42 Feichtenschlager, B. Chemical Tailoring of Metal Oxide Nanoparticle Surfaces to Control Structure and Properties of Polymer Nanocomposites. Ph.D. thesis, Vienna University of Technology, 2011.

43 Svehla, J.; Pabisch, S.; Feichtenschlager, B.; Holzmann, D.; Peterlik, H.; Kickelbick, G. *Macromolecular Materials and Engineering* **2011**,

44 Zabet-Khosousi, A.; Dhirani, A.-A. *Chemical Reviews* **2008**, *108*, 4072–4124.

45 Szekeres, M.; Kamalin, O.; Grobet, P.; Schoonheydt, R.; Wostyn, K.; Clays, K.; Persoons, A.; Dékány, I. *Colloids and Surfaces A: Physicochemical and Engineering Aspects* **2003**, *227*, 77 – 83.

46 Joselevich, M.; Williams, F. J. *Langmuir* **2008**, *24*, 11711–11717.

47 Lummerstorfer, T.; Hoffmann, H. *The Journal of Physical Chemistry B* **2004**, *108*, 3963–3966.

48 Khayet, M.; Villaluenga, J.; Valentin, J.; López-Manchado, M.; Mengual, J.; Seoane, B. *Polymer* **2005**, *46*, 9881 – 9891.

49 Armstrong, N. R.; Shepard, V. R. *The Journal of Physical Chemistry* **1981**, *85*, 2965–2970.

50 Im, H.; Kim, J. *Carbon* **2011**, *49*, 3503 – 3511.

51 Bachinger, A.; Kickelbick, G. *Monatshefte für Chemie / Chemical Monthly* **2010**, *141*, 685–690.

52 Gao, W.; Dickinson, L.; Grozinger, C.; Morin, F. G.; Reven, L. *Langmuir* **1996**, *12*, 6429–6435.

53 Guerrero, G.; Mutin, P. H.; Vioux, A. *Chemistry of Materials* **2001**, *13*, 4367–4373.

54 Sahoo, Y.; Pizem, H.; Fried, T.; Golodnitsky, D.; Burstein, L.; Sukenik, C. N.; Markovich, G. *Langmuir* **2001**, *17*, 7907–7911.

55 Daou, T. J.; Begin-Colin, S.; Grenèche, J. M.; Thomas, F.; Derory, A.; Bernhardt, P.; Legaré, P.; Pourroy, G. *Chemistry of Materials* **2007**, *19*, 4494–4505.

56 Basly, B.; Felder-Flesch, D.; Perriat, P.; Billotey, C.; Taleb, J.; Pourroy, G.; Begin-Colin, S. *Chemical Communications* **2010**, *46*, 985–987.

57 Traina, C. A.; Schwartz, J. *Langmuir* **2007**, *23*, 9158–9161.

58 Brovelli, D.; Hähner, G.; Ruiz, L.; Hofer, R.; Kraus, G.; Waldner, A.; Schlösser, J.; Oroszlan, P.; Ehrat, M.; Spencer, N. D. *Langmuir* **1999**, *15*, 4324–4327.

59 Schulmeyer, T.; Paniagua, S. A.; Veneman, P. A.; Jones, S. C.; Hotchkiss, P. J.; Mudalige, A.; Pemberton, J. E.; Marder, S. R.; Armstrong, N. R. *Journal of Materials Chemistry* **2007**, *17*, 4563–4570.

60 Ulman, A. *Chemical Reviews* **1996**, *96*, 1533–1554.

61 Yee, C.; Kataby, G.; Ulman, A.; Prozorov, T.; White, H.; King, A.; Rafailovich, M.; Sokolov, J.; Gedanken, A. *Langmuir* **1999**, *15*, 7111–7115.

62 Ramirez, E.; Jansat, S.; Philippot, K.; Lecante, P.; Gomez, M.; Masdeu-Bultó, A. M.; Chaudret, B. *Journal of Organometallic Chemistry* **2004**, *689*, 4601 – 4610.

63 Bain, C. D.; Whitesides, G. M. *Angewandte Chemie* **1989**, *101*, 522–528.

64 Stewart, A.; Bell, S. E. J. *Chemical Communications* **2011**, *47*, 4523–4525.

65 Quiros, I.; Yamada, M.; Kubo, K.; Mizutani, J.; Kurihara, M.; Nishihara, H. *Langmuir* **2002**, *18*, 1413–1418.

66 Torma, V.; Peterlik, H.; Bauer, U.; Rupp, W.; Hüsing, N.; Bernstorff, S.; Steinhart, M.; Goerigk, G.; Schubert, U. *Chemistry of Materials* **2005**, *17*, 3146–3153.

67 Weissenbach, K.; Mack, H. In *Functional Fillers for Plastics*; Xanthos, M., Ed.; Wiley-VCH, Weinheim, 2010; Chapter Silane Coupling Agents, pp 59–83.

68 Onclin, S.; Ravoo, B. J.; Reinhoudt, D. N. *Angewandte Chemie* **2005**, *44*, 6282–6304.

69 Elschenbroich, C.; Salzer, A. *Organometallchemie*, 3rd ed.; Teubner, 1993.

70 Altmann, S.; Pfeiffer, J. *Monatshefte für Chemie / Chemical Monthly* **2003**, *134*, 1081–1092.

71 Chi, F.; Guan, B.; Yang, B.; Liu, Y.; Huo, Q. *Langmuir* **2010**, *26*, 11421–11426.

72 Helmy, R.; Fadeev, A. Y. *Langmuir* **2002**, *18*, 8924–8928.

73 Hair, M.; Tripp, C. *Colloids and Surfaces A: Physicochemical and Engineering Aspects* **1995**, *105*, 95 – 103.

74 Tian, R.; Seitz, O.; Li, M.; Hu, W. W.; Chabal, Y. J.; Gao, J. *Langmuir* **2010**, *26*, 4563–4566.

75 Carraro, C.; Yauw, O. W.; Sung, M. M.; Maboudian, R. *The Journal of Physical Chemistry B* **1998**, *102*, 4441–4445.

76 Marcinko, S.; Fadeev, A. Y. *Langmuir* **2004**, *20*, 2270–2273.

77 Neouze, M.-A.; Schubert, U. *Monatshefte für Chemie / Chemical Monthly* **2008**, *139*, 183 – 195.

78 Mutin, P. H.; Guerrero, G.; Vioux, A. *Journal of Materials Chemistry* **2005**, *15*, 3761–3768.

79 Textor, M.; Ruiz, L.; Hofer, R.; Rossi, A.; Feldman, K.; Hähner, G.; Spencer, N. D. *Langmuir* **2000**, *16*, 3257–3271.

80 Brodard-Severac, F.; Guerrero, G.; Maquet, J.; Florian, P.; Gervais, C.; Mutin, P. H. *Chemistry of Materials* **2008**, *20*, 5191–5196.

81 Binder, W. H.; Lomoschitz, M.; Sachsenhofer, R.; Friedbacher, G. *Journal of Nanomaterials* **2009**, *2009*.

82 Woodward, J. T.; Ulman, A.; Schwartz, D. K. *Langmuir* **1996**, *12*, 3626–3629.

83 Pawsey, S.; Yach, K.; Reven, L. *Langmuir* **2002**, *18*, 5205–5212.

84 Randon, J.; Blanc, P.; Paterson, R. *Journal of Membrane Science* **1995**, *98*, 119 – 129.

85 Sellers, H.; Ulman, A.; Shnidman, Y.; Eilers, J. E. *Journal of the American Chemical Society* **1993**, *115*, 9389–9401.

86 Leff, D. V.; Ohara, P. C.; Heath, J. R.; Gelbart, W. M. *The Journal of Physical Chemistry* **1995**, *99*, 7036–7041.

87 Templeton, A. C.; Wuelfing, W. P.; Murray, R. W. *Accounts of Chemical Research* **2000**, *33*, 27–36.

88 Harrell,; Sellers, *Surface Science* **1993**, *294*, 99 – 107.

89 Rousseau, R.; De Renzi, V.; Mazzarello, R.; Marchetto, D.; Biagi, R.; Scandolo, S.; del Pennino, U. *The Journal of Physical Chemistry B* **2006**, *110*, 10862–10872.

90 Rucareanu, S.; Gandubert, V. J.; Lennox, R. B. *Chemistry of Materials* **2006**, *18*, 4674–4680.

91 Ozin, G. A. *Chemical Communications* **2000**, 419–432.

92 Cölfen, H.; Antonietti, M. *Angewandte Chemie* **2005**, *44*, 5576–5591.

93 Das, S. K.; Bhattacharyya, A. J. *The Journal of Physical Chemistry B* **2010**, *114*, 6830–6835.

94 Evans, G.; Duong, G. V.; Ingleson, M. J.; Xu, Z.; Jones, J. T. A.; Khimyak, Y. Z.; Claridge, J. B.; Rosseinsky, M. J. *Advanced Functional Materials* **2010**, *20*, 231–238.

95   Janczewski, D.; Tomczak, N.; Liu, S.; Han, M.-Y.; Vancso, G. J. *Chemical Communications* **2010**, *46*, 3253–3255.

96   Liu, X.; Liu, H.; Zhou, W.; Zheng, H.; Yin, X.; Li, Y.; Guo, Y.; Zhu, M.; Ouyang, C.; Zhu, D.; Xia, A. *Langmuir* **2010**, *26*, 3179–3185.

97   Tchoul, M. N.; Fillery, S. P.; Koerner, H.; Drummy, L. F.; Oyerokun, F. T.; Mirau, P. A.; Durstock, M. F.; Vaia, R. A. *Chemistry of Materials* **2010**, *22*, 1749–1759.

98   Wang, L.; Luo, J.; Schadt, M. J.; Zhong, C.-J. *Langmuir* **2010**, *26*, 618–632.

99   Haldar, K. K.; Sen, T.; Patra, A. *The Journal of Physical Chemistry C* **2010**, *114*, 4869–4874.

100 Wu, M.; Mukherjee, P.; Lamont, D. N.; Waldeck, D. H. *The Journal of Physical Chemistry C* **2010**, *114*, 5751–5759.

101 Gaponik, N. *Journal of Materials Chemistry* **2010**, *20*, 5174–5181.

102 Liu, R.; Aw, J.; Teo, W.; Padmanabhan, P.; Xing, B. *New Journal of Chemistry* **2010**, *34*, 594–598.

103 Wasserscheid, P., Welton, T., Eds. *Ionic Liquids in Synthesis*, 2nd ed.; Wiley-VCH, Weinheim, 2008.

104 Walden, P. *Bulletin of the Russian Academy of Sciences* **1914**, 405 – 422.

105 Belieres, J.-P.; Angell, C. A. *The Journal of Physical Chemistry B* **2007**, *111*, 4926–4937.

106 Scheffler, T. B.; Hussey, C. L.; Seddon, K. R.; Kear, C. M.; Armitage, P. D. *Inorganic Chemistry* **1983**, *22*, 2099–2100.

107 Scheffler, T. B.; Hussey, C. L. *Inorganic Chemistry* **1984**, *23*, 1926–1932.

108 Laher, T. M.; Hussey, C. L. *Inorganic Chemistry* **1983**, *22*, 3247–3251.

109 Boon, J. A.; Levisky, J. A.; Pflug, J. L.; Wilkes, J. S. *The Journal of Organic Chemistry* **1986**, *51*, 480–483.

110 Wilkes, J. S.; Zaworotko, M. J. *Journal of the Chemical Society, Chemical Communications* **1992**, 965–967.

111 Sheldon, R. *Chemical Communications* **2001**, 2399–2407.

112 Gui, J.; Deng, Y.; Hu, Z.; Sun, Z. *Tetrahedron Letters* **2004**, *45*, 2681 – 2683.

113 Bernini, R.; Coratti, A.; Fabrizi, G.; Goggiamani, A. *Tetrahedron Letters* **2003**, *44*, 8991 – 8994.

114 Handy, S. T.; Okello, M. *Tetrahedron Letters* **2003**, *44*, 8395 – 8397.

115 Earle, M. J.; Katdare, S. P.; Seddon, K. R. *Organic Letters* **2004**, *6*, 707–710.

116 Fredin, K.; Gorlov, M.; Pettersson, H.; Hagfeldt, A.; Kloo, L.; Boschloo, G. *The Journal of Physical Chemistry C* **2007**, *111*, 13261–13266.

117 G. Huddleston, J.; D. Rogers, R. *Chemical Communications* **1998**, 1765–1766.

118 Wang, Q.; Baker, G. A.; Baker, S. N.; Colon, L. A. *Analyst* **2006**, *131*, 1000–1005.

119 Bourlinos, A.; Herrera, R.; Chalkias, N.; Jiang, D.; Zhang, Q.; Archer, L.; Giannelis, E. *Advanced Materials* **2005**, *17*, 234–237.

120 Lai, G.; Peng, J.; Li, J.; Qiu, H.; Jiang, J.; Jiang, K.; Shen, Y. *ChemInform* **2007**, *38*.

121 Valkenberg, M. H.; deCastro, C.; Hölderich, W. F. *Green Chemistry* **2002**, *4*, 88–93.

122 Park, M. J.; Lee, J. K.; Lee, B. S.; Lee, Y.-W.; Choi, I. S.; Lee, S.-g. *Chemistry of Materials* **2006**, *18*, 1546–1551.

123 Neouze, M.-A.; Bideau, J. L.; Gaveau, P.; Bellayer, S.; Vioux, A. *Chemistry of Materials* **2006**, *18*, 3931–3936.

124 Göbel, R.; Hesemann, P.; Weber, J.; Moller, E.; Friedrich, A.; Beuermann, S.; Taubert, A. *Physical Chemistry Chemical Physics* **2009**, *11*, 3653–3662.

125 De, M.; Ghosh, P. S.; Rotello, V. M. *Advanced Materials* **2008**, *20*, 4225–4241.

126 Giraldo, L. F.; López, B. L.; Pérez, L.; Urrego, S.; Sierra, L.; Mesa, M. *Macromolecular Symposia* **2007**, *258*, 129–141.

127 Stöber, W.; Fink, A.; Bohn, E. *Journal of Colloid and Interface Science* **1968**, *26*, 62 – 69.

128 Cazin, C. S. J.; Veith, M.; Braunstein, P.; Bedford, R. B. *Synthesis* **2005**, *4*, 622–626.

129 Migowski, P.; Dupont, J. *Chemistry: A European Journal* **2007**, *13*, 32–39.

130 Balaban, A. T.; Klein, D. J.; March, N. H.; Matthai, C. C. *Physics and Chemistry of Liquids* **2005**, *43*, 403–407.

131 Lomoschitz, C. J.; Feichtenschlager, B.; Moszner, N.; Puchberger, M.; Müller, K.; Abele, M.; Kickelbick, G. *Langmuir* **2011**, *27*, 3534–3540.

132 Sofia, L. T. A.; Krishnan, A.; Sankar, M.; Kala Raj, N. K.; Manikandan, P.; Rajamohanan, P. R.; Ajithkumar, T. G. *The Journal of Physical Chemistry C* **2009**, *113*, 21114–21122.

133 Claramunt, R. M.; Lopez, C.; Garcia, M. A.; Denisov, G. S.; Alkorta, I.; Elguero, J. *New Journal of Chemistry* **2003**, *27*, 734–742.

134 Hickman, B. S.; Mascal, M.; Titman, J. J.; Wood, I. G. *Journal of the American Chemical Society* **1999**, *121*, 11486–11490.

135 Marchetti, F.; Pettinari, C.; Pettinari, R.; Cingolani, A.; Gobetto, R.; Chierotti, M. R.; Drozdov, A.; Troyanov, S. I. *Inorganic Chemistry* **2006**, *45*, 3074–3085.

136 Ueda, T.; Masui, H.; Nakamura, N. *Solid State Nuclear Magnetic Resonance* **2001**, *20*, 145 – 155.

137 Peterlik, H.; Fratzl, P. *Monatshefte für Chemie / Chemical Monthly* **2006**, *137*, 529–543.

138 Smarsly, B.; Groenewolt, M.; Antonietti, M. *Scattering Methods and the Properties of Polymer Materials*; Progress in Colloid and Polymer Science; Springer Berlin / Heidelberg, 2005; Vol. 130; pp 127–140.

139 Pedersen, J. S. *Advances in Colloid and Interface Science* **1997**, *70*, 171 – 210.

140 Neouze, M.-A.; Litschauer, M. *The Journal of Physical Chemistry B* **2008**, *112*, 16721–16725.

141 Fitchett, B. D.; Conboy, J. C. *The Journal of Physical Chemistry B* **2004**, *108*, 20255–20262.

142 Zhou, Y.; Schattka, J. H.; Antonietti, M. *Nano Letters* **2004**, *4*, 477–481.

143 Hirano, M.; Nakahara, C.; Ota, K.; Tanaike, O.; Inagaki, M. *Journal of Solid State Chemistry* **2003**, *170*, 39 – 47.

144 Ito, S.; Yoshida, S.; Watanabe, T. *Chemistry Letters* **2000**, *29*, 70–71.

145 Wang, C.-C.; Ying, J. Y. *Chemistry of Materials* **1999**, *11*, 3113–3120.

146 Chen, X.; Mao, S. S. *Chemical Reviews* **2007**, *107*, 2891–2959.

147 Carp, O.; Huisman, C.; Reller, A. *Progress in Solid State Chemistry* **2004**, *32*, 33 – 177.

148 Lee, J.; Yang, Y. *Journal of Materials Science* **2006**, *41*, 557–559.

149 O'Regan, B.; Grätzel, M. *Nature* **1991**, *353*, 737–740.

150 Choi, W.; Termin, A.; Hoffmann, M. R. *The Journal of Physical Chemistry* **1994**, *98*, 13669–13679.

151 Ivanovici, S. Synthetic Methods to Control the Structure of Titania - Polymer Hybrid Materials and Nanocomposites. Ph.D. thesis, Vienna University of Technology, 2008.

152 Stichert, W.; Schüth, F.; Kuba, S.; Knözinger, H. *Journal of Catalysis* **2001**, *198*, 277 – 285.

153 Rhodes, M. D.; Bell, A. T. *Journal of Catalysis* **2005**, *233*, 198 – 209.

154 Feichtenschlager, B.; Pabisch, S.; Peterlik, H.; Kickelbick, G. *Langmuir* **2011**,

155 Neuberger, T.; Schöpf, B.; Hofmann, H.; Hofmann, M.; von Rechenberg, B. *Journal of Magnetism and Magnetic Materials* **2005**, *293*, 483 – 496.

156 Gao, Q.; Chen, F.; Zhang, J.; Hong, G.; Ni, J.; Wei, X.; Wang, D. *Journal of Magnetism and Magnetic Materials* **2009**, *321*, 1052 – 1057.

157 Iida, H.; Takayanagi, K.; Nakanishi, T.; Osaka, T. *Journal of Colloid and Interface Science* **2007**, *314*, 274 – 280.

158 Crouzet, L.; Leclercq, D.; Mutin, P. H.; Vioux, A. *Chemistry of Materials* **2003**, *15*, 1530–1534.

159 Kley, J. T.; Unger, C.; Massing, U. *Monatshefte fr Chemie / Chemical Monthly* **1998**, *129*, 173–185.

160 Arbusow, B. A. *Pure and Applied Chemistry* **1964**, *9*, 307–336.

161 Hassan, J. *German Application, DE19843383* **2000**, p. 34 pp.

162 McKenna, C. E.; Higa, M. T.; Cheung, N. H.; McKenna, M.-C. *Tetrahedron Letters* **1977**, *18*, 155 – 158.

163 Li, S.; Hong, M. *Journal of the American Chemical Society* **2011**, *133*, 1534–1544.

164 Frantz, R.; Granier, M.; Durand, J.-O.; Lanneau, G. F. *Tetrahedron Letters* **2002**, *43*, 9115 – 9117.

165 Jiang, Y.; Decker, S.; Mohs, C.; Klabunde, K. J. *Journal of Catalysis* **1998**, *180*, 24 – 35.

166 McDermott, J. E.; McDowell, M.; Hill, I. G.; Hwang, J.; Kahn, A.; Bernasek, S. L.; Schwartz, J. *The Journal of Physical Chemistry A* **2007**, *111*, 12333–12338.

167 Rouquerol, F.; Rouquerol, J.; Sing, K. *Adsorption by Powders and Porous Solids*; Academic Press, 1999.

168 Brunauer, S.; Emmett, P. H.; Teller, E. *Journal of the American Chemical Society* **1938**, *60*, 309–319.

169 Tartaj, P. *Chemmical Communication* **2011**, *47*, 256–258.

170 Das, S. K.; Bhunia, M. K.; Bhaumik, A. *Dalton Transaction* **2010**, *39*, 4382–4390.

171 Yang, J.; Peterlik, H.; Lomoschitz, M.; Schubert, U. *Journal of Non-Crystalline Solids* **2010**, *356*, 1217 – 1227.

172 Chi, B.; Zhao, L.; Jin, T. *The Journal of Physical Chemistry C* **2007**, *111*, 6189–6193.

173 Lorret, O.; Francová, D.; Waldner, G.; Stelzer, N. *Applied Catalysis B: Environmental* **2009**, *91*, 39 – 46.

174 Guillard, C.; Puzenat, E.; Lachheb, H.; Houas, A.; Herrmann, J.-M. *International Journal of Photoenergy* **2005**, *7*, 1–9.

175 Czakler, M. Verknüpfte Metallnanopartikel für neue Hybridmaterialien. M.Sc. thesis, Vienna University of Technology, 2011.

176 Czakler, M.; Litschauer, M.; Föttinger, K.; Peterlik, H.; Neouze, M.-A. *The Journal of Physical Chemistry C* **2010**, *114*, 21342–21347.

177 Nunes, S. C.; de Zea Bermudez, V.; Cybinska, J.; Sa Ferreira, R. A.; Legendziewicz, J.; Carlos, L. D.; Silva, M. M.; Smith, M. J.; Ostrovskii, D.; Rocha, J. *Journal of Materials Chemistry* **2005**, *15*, 3876–3886.

178 Yang, J.-Z.; Zhang, Z.-H.; Fang, D.-W.; Li, J.-G.; Guan, W.; Tong, J. *Fluid Phase Equilibria* **2006**, *247*, 80 – 83.

179 Gandour, R. D.; Nabulsi, N. A. R.; Fronczek, F. R. *Journal of the American Chemical Society* **1990**, *112*, 7816–7817.

180 MacDonald, J. C.; Dorrestein, P. C.; Pilley, M. M. *Crystal Growth & Design* **2001**, *1*, 29–38.

181 Rether, C.; Verheggen, E.; Schmuck, C. *Chemmical Communications* **2011**, *47*, 9078–9079.

182 Sun, Y.; Gray, S. K.; Peng, S. *Physical Chemistry Chemical Physics* **2011**, *13*, 11814–11826.

183 Annapureddy, H. V. R.; Kashyap, H. K.; De Biase, P. M.; Margulis, C. J. *The Journal of Physical Chemistry B* **2011**, *115*, 9507–9508.

184 Cui, D.; Koder, R. L.; Dutton, P. L.; Miller, A.-F. *The Journal of Physical Chemistry B* **2011**, *115*, 7788–7798.

185 Kern, W., Ed. *Handbook of Silicon Wafer Cleaning Technology*; William Andrew Publishing/Noyes, 1993.

186 Basnar, B.; Friedbacher, G.; Brunner, H.; Vallant, T.; Mayer, U.; Hoffmann, H. *Applied Surface Science* **2001**, *171*, 213 – 225.

187 Reeve, D. W.; Tan, Z. *Journal of Wood Chemistry and Technology* **1998**, *18*, 417–426.

188 Kakiage, K.; Yamamura, M.; Fujimura, E.; Kyomen, T.; Unno, M.; Hanaya, M. *Chemistry Letters* **2010**, *39*, 260–262.

189 Kim, W. B.; Choi, S. H.; Lee, J. S. *The Journal of Physical Chemistry B* **2000**, *104*, 8670–8678.

190 Gervais, C.; Babonneau, F.; Smith, M. E. *The Journal of Physical Chemistry B* **2001**, *105*, 1971–1977.

191 Fandos, R.; Gallego, B.; Otero, A.; Rodriguez, A.; Ruiz, M. J.; Terreros, P. *Dalton Transaction* **2007**, 871–877.

192 Moss, J. A.; Szczepankiewicz, S. H.; Park, E.; Hoffmann, M. R. *The Journal of Physical Chemistry B* **2005**, *109*, 19779–19785.

193 Basnar, B.; Madera, M.; Friedbacher, G.; Vallant, T.; Mayer, U.; Hoffmann, H. *Microchimica Acta* **2000**, *133*, 325–329.

194 Klemm, D.; Heublein, B.; Fink, H.-P.; Bohn, A. *Angewandte Chemie International Edition* **2005**, *44*, 3358–3393.

195 Steinbüchel, A., Doi, Y., Eds. *Biotechnology of Biopolymers From Synthesis to Patents. Volume 1.*; Wiley-VCH, Weinheim, 2005.

196 Steinbüchel, A., Doi, Y., Eds. *Biotechnology of Biopolymers From Synthesis to Patents. Volume 2.*; Wiley-VCH, Weinheim, 2005.

197 Kraft, A. *Chemistry & Industry* **2001**, *15*, 479–480.

198 Entcheva, E.; Bien, H.; Yin, L.; Chung, C.-Y.; Farrell, M.; Kostov, Y. *Biomaterials* **2004**, *25*, 5753 – 5762.

199 Fischer, F.; Rigacci, A.; Pirard, R.; Berthon-Fabry, S.; Achard, P. *Polymer* **2006**, *47*, 7636 – 7645.

200 Innerlohinger, J.; Weber, H. K.; Kraft, G. *Macromolecular Symposia* **2006**, *244*, 126–135.

201 Liebner, F.; Haimer, E.; Potthast, A.; Loidl, D.; Tschegg, S.; Neouze, M.-A.; Wendland, M.; Rosenau, T. *Holzforschung* **2009**, *63*, 3 – 11.

202 Liebner, F.; Haimer, E.; Wendland, M.; Neouze, M.-A.; Schlufter, K.; Miethe, P.; Heinze, T.; Potthast, A.; Rosenau, T. *Macromolecular Bioscience* **2010**, *10*, 349–352.

203 Liebner, F.; Potthast, A.; Rosenau, T.; Haimer, E.; Wendland, M. *Holzforschung* **2008**, *62*, 129 – 135.

204 Liebner, F.; Potthast, A.; Rosenau, T.; Haimer, E.; Wendland, M. *Research Letters in Materials Science* **2007**, *2007*.

205 Aljaberi, A.; Chatterji, A.; Shah, N. H.; Sandhu, H. K. *Drug Development and Industrial Pharmacy* **2009**, *35*, 1066–1071.

206 Gill, R. S.; Marquez, M.; Larsen, G. *Microporous and Mesoporous Materials* **2005**, *85*, 129 – 135.

207 Gonçalves, G.; Marques, P. A.; Trindade, T.; Neto, C. P.; Gandini, A. *Journal of Colloid and Interface Science* **2008**, *324*, 42 – 46.

208 Tanaka, K.; Kozuka, H. *Journal of Sol-Gel Science and Technology* **2004**, *32*, 73–77.

209 Amarasekara, A. S.; Owereh, O. S. *Carbohydrate Polymers* **2009**, *78*, 635 – 638.

210 Barud, H.; Assunção, R.; Martines, M.; Dexpert-Ghys, J.; Marques, R.; Messaddeq, Y.; Ribeiro, S. *Journal of Sol-Gel Science and Technology* **2008**, *46*, 363–367.

211 Hou, A.; Shi, Y.; Yu, Y. *Carbohydrate Polymers* **2009**, *77*, 201 – 205.

212 Kulpinski, P. *Journal of Applied Polymer Science* **2005**, *98*, 1793–1798.

213 Love, K. T.; Nicholson, B. K.; Lloyd, J. A.; Franich, R. A.; Kibblewhite, R. P.; Mansfield, S. D. *Composites Part A: Applied Science and Manufacturing* **2008**, *39*, 1815 – 1821.

214 Maeda, H.; Nakajima, M.; Hagiwara, T.; Sawaguchi, T.; Yano, S. *Journal of Materials Science* **2006**, *41*, 5646–5656.

215 Pinto, R. J.; Marques, P. A.; Barros-Timmons, A. M.; Trindade, T.; Neto, C. P. *Composites Science and Technology* **2008**, *68*, 1088 – 1093.

216 Sequeira, S.; Evtuguin, D. V.; Portugal, I. *Polymer Composites* **2009**, *30*, 1275–1282.

217 Sequeira, S.; Evtuguin, D. V.; Portugal, I.; Esculcas, A. P. *Materials Science and Engineering: C* **2007**, *27*, 172 – 179.

218 Xie, K.; Yu, Y.; Shi, Y. *Carbohydrate Polymers* **2009**, *78*, 799 – 805.

219 Yano, S.; Iwata, K.; Kurita, K. *Materials Science and Engineering: C* **1998**, *6*, 75 – 90.

220 Sun, J.; Xu, F.; Sun, X.; Xiao, B.; Sun, R. *Polymer Degradation and Stability* **2005**, *88*, 521 – 531.

221 Xiao, B.; Sun, X. F.; Sun, R. *Polymer Degradation and Stability* **2001**, *74*, 307 – 319.

LEBENSLAUF – MARCO LITSCHAUER

Angaben zu Person

Name	DI Litschauer Marco
Adresse	Leopoldstraße 48, 3400 Klosterneuburg
Telefon	+43 699 10 93 97 96
E-Mail	Download_Marco@yahoo.com
Staatsangehörigkeit	Österreich
Geburtsdatum/-ort	13. Oktober 1981 in Klosterneuburg
Familienstand	ledig

Berufserfahrung

03/2007 – 10/2011

Projektassistent
Institut für Materialchemie, **Technische Universität Wien**, Getreidemarkt 9/BC/02, 1060 Wien
Forschungstätigkeit im Bereich der Angewandten Anorganischen Chemie und Materialchemie

- Eigenverantwortliche Durchführung der Arbeiten im Rahmen der Dissertation (Literaturrecherche, Konzepterstellung, Versuchsplanung & -durchführung, Charakterisierung, Dokumentation, Abfassung wissenschaftlicher Publikationen,…)
- Präsentation der Ergebnisse auf internationalen und nationalen Fachtagungen
- Betreuung, Wartung verschiedener Labor- & Analysengeräte (UV-Vis, DLS, TGA,…)
- Betreuung von Studenten im Rahmen von Praktika

07-08 2004/2005

Aushilfe
Hagebau Schilowsky GmbH (ehemalig Hagebau Litschauer), Hirstettner Str. 63, 1220 Wien
div. Aushilfsarbeiten, u.a. in der Buchhaltung

03-04/2003

Praktikum
Wirtschaftsauskunftei Maria Wisur GmbH, Weißgerberlände 44-46/Top 8, 1030 Wien
Datenbankoptimierung

Ausbildung

05/2008 - 11/2011

Doktoratsstudium der technischen Wissenschaften aus Technischer Chemie im Bereich der Angewandten Anorganische Chemie und Materialchemie – Abschluß vorraussichtlich Mitte Dezember 2011, betreut durch Dr. M.-A. Neouze und Prof. U. Schubert

- Konzepterstellung und Literaturrecherche
- Versuchsplanung & -durchführung
- Charakterisierung der Produkte (DLS, TGA, IR, NMR, SAXS,…)
- Dokumentation der Ergebnisse
- Abfassung wissenschaftlicher Publikationen & der Dissertation (in Englisch)
- Präsentation der Ergebnisse auf internationaler & nationaler Ebene
- Absolvierung zusätzlicher Lehrveranstaltungen aus dem Bereich der anorganischen Chemie, Materialchemie und Polymerchemie

Institut für Materialchemie, Technische Universität Wien, Getreidemarkt 9/BC/02, 1060 Wien

10/2001 – 03/2008

Diplomstudium Technische Chemie –unter Erwerb des Titels „Diplom Ingenieur" abgeschlossen
Ausbildungsschwerpunkt: Technische Synthese
Diplomarbeit zum Thema „Neue Hybrimaterialien basierend auf der Chemie ionischer Flüssigkeiten" an der Fakultät für Technische Chemie auf dem Institut für Materialchemie, Getreidemarkt 9/BC/02, 1060 Wien, betreut durch Dr. M.-A. Neouze und Prof. U. Schubert, verfasst zwischen 03/2007 – 03/2008

09/1992 – 06/2000	**Bundesrealgymnasium** – mit Matura abgeschlossen BG/BRG Klosterneuburg, Buchberggasse 31, 3400 Klosterneuburg

Zivildienst

10/2000 – 09/2001	**abgeleistet** am Rehabilitationszentrum Weißer Hof, Holzgasse 350, 3400 Klosterneuburg

Persönliche Fähigkeiten und Kompetenzen

Muttersprache	Deutsch
Weitere Sprachen	Englisch (verhandlungsfähig) Französisch (Grundkenntnisse in Wort und Schrift/Maturaniveau)
Soziale Kompetenzen	**Teamfähigkeit** (erworben in verschiedenen Mannschaftssportarten – z. B. Fußball – und durch die Arbeit in verschiedenen Forschungsgruppen an der Universität) **Führungsfähigkeit** und **Verantwortungsbewusstsein** (erworben durch Lehrtätigkeiten an der Universität) **Ausdauer** (erworben durch zahlreiche sportliche Aktivitäten, wie Fußball, Radfahren (Teilnahme an div. Wettkämpfen), Badminton,…)
Organisatorische Kompetenzen	**Projektorganisation** (erworben während der selbstständigen Erarbeitung der Doktorarbeit und der Diplomarbeit)
Technische Kompetenzen	Umfangreiche Kenntnisse in zahlreichen chemierelevanten Analysenmethoden (DLS, TGA, IR, NMR, SAXS,…)
IT Kompetenzen	Sehr gute Kenntnisse in Standardanwendungen (Windows, Office, Latex,…) Sehr gute Kenntnisse in zahlreichen chemierelevanten Applikationen (ISIS, ChemOffice, SciFinder, Origin,…) Gute Hardwarekenntnisse
Künstlerische Kompetenzen	Langjähriger Unterricht am Klavier an der Musikschule Klosterneuburg
Führerschein	Klasse **B** (ausgestellt am 27.07.2000)

Zusätzliche Angaben

Hobbies/Aktivitäten	Brett-, Gesellschaftsspiele, Radtechnik, Sport (Radfahren, Fußball,…)
Mitgliedschaften	Mitglied der Gesellschaft Österreichischer Chemiker (GÖCh), ATV Grinzing